FACULTY OF SCIENCE AND TECHNOLOGY

MASTER'S THESIS

Study programme / specialisation: Marine and Offshore Technology	Spring semester, 2022 Open
Author: Christodoulos Tryfonidis	(signature author)

Course coordinator: Professor Yihan Xing
Supervisors: Professor Muk Chen Ong
Co-Supervisor: Chern Fong Lee

Thesis title:
Power Performance and Response Analysis of a Semi-Submersible Wind Turbine Combined with Wave Energy Converters in Intermediate and Deep Water.

Credits (ECTS): 30 ECTS

Keywords: STFC; floating wind turbines; wave energy converters; hybrid mooring system; renewable energies

Pages: 89

Stavanger, 15 / 06 / 2022

ABSTRACT

Renewable energies are the forefront against environmental pollution and the leading technology in sustainable energy sources. Power produced by wind energy is a well established technology. There is a lot of space for expansion though, especially at offshore environment. Floating wind turbines can take advantage of the abundant wind energy available far out at the oceans. Increasing the power production of such structures and ensuring the efficient and safe position keeping of them in every depth is crucial. Two concepts that aim to tackle down these two issues are proposed. A combination of wind and wave energy converters and an intermediate water depth mooring arrangement. The installation of wave energy converters (WECs) at the floating wind turbine base will reduce the levelized cost of energy (LCoE). The use of the same power cables and mooring arrangement to deploy the WECs can prove beneficial financially wise. Furthermore, it can act as a boost to the development of wave energy in general. The transient depth between shallow and deep is a challenging field for the traditional mooring arrangements. A cost effective solution will help the deployment of floating wind turbines in this intermediate water depth fields.

A novel concept of combining a floating wind turbine with WECs is proposed. A semi submersible floater is used to support a 5MW wind turbine. Three flap typed WECs are deployed on the pontoons of the floater. A two-point type absorber called Torus is installed at the central column. The proposed concept is named STFC. A thorough analysis of the natural periods, regular and irregular wave tests is performed to evaluate the effect of the WECs to the floater's behavior. Small to no effect is observed across all degrees of freedom except the reduction in pitch period due to increased hydrostatic stiffness. The irregular wave tests indicate that the absorbed power amplitude operator (RAO) of Torus has a wider excitation range than the flaps. The floater heave RAO is affected by the addition of Torus and the floater surge and pitch RAOs are affected by the additions of flaps. Irregular waves tests are carried out to evaluate the influence of the added WECs to the motions of the combined concept and the total power performance. The results indicate that the WECs have little to no effect to the motions of the structure except the expected reduction in pitch motions. This is preliminary indication that no changes should be made to the mooring due to the addition of WECs. The wind turbine power performance is not affected by the addition of WECs. There is small reduction in pitch standard deviation though, in loading condition EC3 that leads to slightly better wind quality. The Torus

performance is satisfactory as it accounts for 9% of the total STFC power production. The total three flaps account only for 14% of the Torus power production thus their power performance is not satisfactory. The flaps rotation is out of phase with the wave excitation force so there is room for improvement if active damping and stiffness control is added.

Following, the STFC is moved to intermediate water depth z = -50m and a new hybrid mooring design is proposed. A brief explanation of the intermediate water mooring challenges is given and the basic design criteria are established. A step to step designing process is presented. The combination of studded chain, buoys, and clump weights is proposed. The name of the concept is CCCB. A restoring force test is carried out and the linearity of the restoring force response is verified. Irregular wave tests are carried out and the data indicate that the new mooring design is a feasible design. The maximum floater offset is restrained to 14% of the water depth. The pretension of the mooring system proves to be a significant factor for the total performance of the mooring arrangement. The maximum mooring line tension is kept within safe limits throughout the whole offset range. CCCB is compared with similar concepts and proves itself stiffer mainly because of its increased pretension. Points of interest are defined across the mooring line and spectra analysis is performed to evaluate the distribution of response frequencies across the chain length. The role of buoys as dampers of motions is established. CCCB utilization factor indicates that this mooring design can be used also in larger structures and there is room for cost reduction measures.

ACKNOWLEDGMENTS

First and foremost, I want to thank my supervisor professor Muk Chen Ong. Professor Ong has an interesting personality and never settles for mediocracy. On the contrary, he obsessively goes after perfection in every aspect of his work. I want to thank him for giving me the opportunity to participate in a publication with him and accepted me working with his team. He pushed me to my limits and regardless the reason he did it, I grew stronger. His effort to dig out your fears, insecurities, and lack of motivation puts you up a tiring uphill but, in the end, you realize that it's these insecurities and bad phycology that is holding you back. Comfort zone is an unknown word to Professor Ong and if I had to live these two years again, I would still choose him as my supervisor.

The second but not less important person that I want to thank is Chern Fong Lee. Chern has proven a good friend at times I needed him. I want to thank him for putting up with my incompetence sometimes. I appreciate him because trying to work with Professor Ong and me was like trying to pass through the Clashing Rocks. His help proved vital in many parts of the thesis and the troubleshooting with him was always a pleasant procedure.

The person that I have spent the most time with during this thesis is my classmate Hammad Munir. Hammad has a kind personality and the will to communicate and help in an unselfish way. Our everyday communication and cooperation have proven really helpful for me, I want to greatly thank him for his company and valuable friendship.

Despite the ups and downs during these two years I had a great time with all my classmates

In my personal life I would like to thank Gülen for always being there for me patiently. My experience in Norway would be really different without her. She has been the tune of joy in my everyday life. I will never forget the moments we've been together.

The person that I owe a great deal is Areti. Her name means virtue and she has been a great support in my darkest days. A big part of what I achieved regardless of how big or small it is, I owe it to her. I hope one day I can pay her back for everything she has done for me.

They say that in life we end up where we began, and I will finish the acknowledgments with my family. I would like to thank them for supporting and understand me.

RESEARCH PAPERS

1. C.F Lee, C. Tryfonidis, M.C Ong (2022) Power Performance and Response Analysis of a Semi-Submersible Wind Turbine with Combined Flap Type and TORUS Wave Energy Converters. OMAE2022-79483

   Future publication
2. C. Tryfonidis, C.F Lee, M.C Ong (2022) Design and Response Analysis of a hybrid mooring system for intermediate water applications.

DECLARATION OF AUTHORSHIP

Regarding the authorship in Paper 1, I am the second author and I was responsible for numerical modeling and dynamic simulations under the supervision of Chern Fong Lee and Professor Muk Chen Ong.

TABLE OF CONTENTS

LIST OF FIGURES

LIST OF TABLES

1 INTRODUCTION

1.1 Background and motivation

Energy

Ενέργεια

εν (in) + έργω (action)

Energy is word and a term that frequently comes up in our daily conversations. Either people complain that they do not have the energy to complete a task, or in a larger scale, they hear about the energy crisis. As a general understanding, most people do realize that energy is both produced and consumed. The origin of the idea that there is energy in its modern meaning can be traced back to ancient Greek philosophers. The first reference to the word energy as it was reported by Lindsay et al. [1] in her book Energy: Historical Development of the Concept, was made by Aristotle in his work *Physics* (*Φυσικά*). He combined the words 'in' and 'action' and created the word energy which is directly translated as 'the state of acting'. Also, Heraclitus identified fire both as energy and the source of everything; 'Τὸ Πῦρ', directly translates as fire, but semantically means an ethereal essence which could be transformed into the common objects of our experience without net loss [1]. Burnet J. in his book Early Greek philosophy [2], documented Heraclitus claim that this world, the same for every being, was created by neither God nor a human, but has been forever, is, and will always be eternal live fire, which burns stronger with a rate, and burns weaker with a rate. Both interpretations foresaw the presence of energy transformation in every change of state. Even though these approaches were made from a philosophical standpoint, we cannot help it, but notice the early roots of energy definition.

Approaching energy from an evolutionary perspective, it must be emphasized that humans belong to the heterotrophic group of organisms and must obtain energy from an external source to sustain their homeostatic state. The autotroph organisms, on the other hand, such as plants, produce the energy they need on their own [3]. Both groups of organisms, no matter if they are primary producers or consumers, are characterized as metabolizers. Every living organism on planet Earth, one way or another, metabolizes some sort of energy; either its chemical energy obtained from food and transformed to motion and heat or light energy that is transformed to

chemical energy by plants. Energy acquisition has been and will always be living organisms' primary task, it is embedded in their genes and is the fundamental principle that bonds us to the materialistic world. A species' ability to thrive is closely related to its ability to obtain the proper amount of energy, primarily to withstand life and secondly to expand. In nature, the expansion of a species takes place up to the extent that another antagonist species allows it, in the form of a natural predator, or till the natural resources (energy), food for instance, in the given space cannot withstand the large species population and the ecosystem equilibrium collapses. Human societies are far from that primitive state and homo sapiens are the only living organism that systematically increased the energy productivity of nature. A striking early example of this intervention to nature is the selective breeding of wheat. Wheat has been evolving naturally by hybridization and polyploidization, but despite the long process of natural mutations, the wheat breeds existing 10.000 years ago could not produce enough food to sustain large communities. The primary reason is that natural selection does not reward only the genes accounted for the total food (energy) produced, but also for resilience to weather exposure, adaptability, and resilience to new diseases [4]. The first selective breeding happened with the domestication of wheat between 10.000 and 8.000 BC [5], when humans systematically chose the most food productive breeds of wheat to reproduce. This increased the wheat produced per hectare and contributed to the formation of the first civilization in the Mesopotamian region. At the domestication of wheat and the transition from hunter gatherer to agriculture, the first human effort to improve energy acquisition can be foreseen.

As societies grew more complex, individuals' intelligence rose and energy acquisition for survival purposes was already fulfilled. This was the turning point where human brain could consume more energy for intellectual thinking rather than survival purposes and until today this applies to most functional members of Western societies.

Despite the complexity of modern-day societies and technological advancements available, we have not really evaded our energy dependance and our natural mechanisms to obtain the energy itself.

This realization of the inevitability of our energy dependence and its close relationship with death and thriving, has been noticed by humans during early stages of civilization development. Greek mythology and Old Testament's first book Genesis contain two allegories that document this realization. Regardless of the chronological order, as it cannot be verified, both allegories

deal with the concept of creation, origin and contain a metaphor of documenting our energy dependence.

In *Genesis*, chapters two and three, there is a story of the first human beings living in the Garden of Eden where they did not have to grow their own food as everything was readily available for them. Following the incident of Adam and Eve eating the fruit of knowledge, it is written (3:17) , 'Cursed is the ground because of you; in toil you shall eat of it all the days of your life', and goes on (3:19) 'By the sweat of your face you shall eat bread until you return to the ground, for out of it you were taken; you are dust, and to dust you shall return'. These few lines provide us with the first record of the information that we are dependent on energy, and we must struggle, sweat to obtain it, but most importantly, they contain the emotional context in which this realization is conceived, which is the feeling of being punished.

Furthermore, in the myth of Prometheus, whose name is translated as 'the one who thinks beforehand', with its many variations, we have a more complex allegory for creation. The predominant myth alteration is the one given by Aeschylus in his dramatization act "Prometheus Bound" where Prometheus is the one who created humans, primarily only males. Prometheus is a Titan that survived the conflict between Titans and Gods because he enlisted with the side of Zeus [6]. Despite him picking the side of Gods, he sympathized with humans and despised the way that Zeus treated humans. Humans and Gods lived under the same rule and humans in this story also did not have to harvest their food as they were fed with the divine food ambrosia. After Prometheus played a trick on Zeus during a sacrifice, Zeus decided to take fire away from humans, bringing them back to a primitive state and leaving them in dark. Prometheus stole fire and gave it back to humans together with technology, knowledge, and the creation of civilization. Zeus got infuriated and punished humans by creating a woman named Pandora, meaning 'the one bringing gifts', gifting her with a box that contained each possible suffering and ordered her not to open it. Pandora was given as a wife to Epimetheus, the brother of Prometheus, whose name means 'the one who thinks later'. At the first night of her marriage, she opened the box and released all the possible suffering including war, hunger, death, and expelled humans from living with Gods [6].

In both stories, the readers encounter the archetype notion that there is a state of being in which humans are free of their need for food (energy) and a divine intervention in their creation. The latter is most probably sourced by the realization made by early humans of their superiority against the rest of the earth's fauna.

Earlier human civilizations approached their existence and the reason they have to struggle to survive with a religious approach to explain the why and how of their being. Nowadays we know more about the origin of humans, and interestingly enough, we can see that there is a direct relation between our ability and efficiency to obtain energy and the evolutionary changes in an earlier stage and later with societal changes.

Evolutionary wise, as Richard Wrangham, a primatologist has pointed out in his book *Catching Fire*, that cooking through fire was the main reason that homo sapiens evolved the way they did [7]. Cooking is a form of predigesting that enables humans to chew in less time, compared to other relative species such as chimpanzees who chew approximately 6 to 9 hours a day trying to tender their food. This new increased energy acquisition competency led to less chewing and smaller jaws with smaller skull and brain without a reduction in the cognitive ability [7]. The spare time saved could now be used for other activities than eating, subsequently leading to the first human-related evolutionary change due to a change in energy acquisition.

The most primitive societal changes due to changes in our energy acquisition can be traced again to our closest relatives, chimpanzees, who often attack neighboring chimpanzee communities and eliminate them proactively in order to take over their land. Even though there is no immediate benefit, the ability to control and hunt at the new extended area, results in increased muscle density of the males and even shorter periods between reproduction for the females. As a result, the attacking and prevailing community thrives [7].

Energy, in every form, being the ultimate goal throughout our existence, is the bone of contention behind every major conflict. Starting from the trivial food acquisition till the mass exploration of fossil fuels, energy acquisition is the key factor behind social and economic changes.

Nowadays, the growing movement of green energy is a proactive ‘made believe’ change, trying to be imposed. Humans do not operate on a primitive level anymore so they can understand and foresee that the way they obtain energy through nonrenewable energy sources are finite, and sooner or later, will come to an end. The exact timeframe is highly disputable, but the fact that at least the current forms of energy sources available will come to an end, is not. Another disputable aspect of the “green change movement” is the exact quantification of the impact that fossil fuels have on our planet. A sceptic should examine this topic free from ideological prejudices. The phenomena in which conservatives and liberals, or opposing sides in general, stand in completely opposite grounds on this matter, should worry people because any conflict

that persists for a long time, gets an ideological, and almost a religious character, and in the long run makes it practically impossible to distinguish the objective truth from the subjective opinions of the opponents and their rhetoric debating abilities.

Renewable energy acquisition through wind, solar and wave is the main way to decarbonize the global energy production. Nuclear and other sources of equal complexity and risk are not considered due to the negative public opinion regarding their huge nature and society impact in case of a major accident. This thesis goal, except the technical aspects of the project is to try and locate the position that renewable energies will obtain in the next 50 years. To realize how important role the renewables will play we should describe the changing environment in which they will exist.

We now live in the beginning of the 4th industrial revolution, the information era. Succeeding the 3rd revolution, consisting of the digitization and automization of the production, 4th revolution will be a fusion of the macro and microstate of being, meaning the physical and biological state respectively and the digital world [8]. The connecting link between these separate entities will be the internet. The expansion of internet and its speed increase have settled a breeding ground for this fusion to take place [9]. As every other revolution, this one is also an anthropocentric change. The previous revolutions achieved to satisfy primary, basic, and later consumer needs, but this one is going a step further as it involves humans not as recipients but as components of the revolution itself. The internet of things is not only an industry related issue, as we can see it happening also right in front of our eyes among human population. In developed societies, we have reached to a point where individuals are 24/7 connected to the grid with their smartphones. The next step after smartphones will be an augmented human connected with the network and interacting with the new blurred physical/digital interface applications, them being an autonomous car or a smart home. Even before going to the next step, the amount of information being produced per minute by the billions of humans interacting with their phone is abundant to the point that we cannot process it. At the extent we can interpretate them though they prove precious and a game changer in decision making, wealth creation and control, thus the phrase “data is the new oil” that came from the mathematician Clive Humby [10]. Information has always been important but at this point, information becomes equally important and valuable as energy.

Each industrial revolution can be considered as a change of state, a step up for the humanity. For this change to happen, humanity must follow the thermodynamic principle of

latent heat. When a substance changes phase, the arrangement of its molecule's changes, but its temperature does not change. Transiting from 100°C liquid to 100°C vapor, water absorbs 2264.705 KJ/K/ °C energy far greater than what it is required for the same amount of water to increase 1°C. The first industrial revolution became possible because of the advanced steam engines burning coal, the second industrial revolution happened with the help of fossil fuels and diesel engines and the third industrial revolution took place by the electrification of the production. The new, improved, energy acquisition competency is the medium that provides the required "latent heat" to humanity in order to jump to the next step. Energy and our ability to obtain it is the common denominator in every social change around us. Fire and cooking allowed us to evolve and transit to the next phase and now the new energy acquisition skills will help humanity further.

Renewable energy is not the protagonist but a candidate mentor of the protagonist in this 4th industrial revolution, the same way steam engines contributed to the 1st industrial revolution. The protagonist was and will always be humans and their eternal struggle to obtain energy. It's not obvious if renewable energies or something else will be the technology, the breakthrough, that will produce the latent heat and help us reach at the next stage and complete the 4th rearrangement of humanity "molecules", but the revolution will not be completed if we don't change the way we obtain energy. AI and blockchain networks will play a crucial role in the processing of the massive amount of information being produced and alongside sustainable energy production most probably will complement the 4th revolution.

As each revolution was built on the base of the previous one, the same way the 4th revolution and renewable energy will co-exist, improve the previous infrastructure. We shouldn't overlook though the second evolutionary story with the chimpanzees taking over the neighboring land and try to identify similar patterns, behaviors in today's world. By overlooking them, we are creating problematic societies that can't contribute or follow up to the effort for improving our relationship with the environment. A war torn apart society would have to go through decades before they will even think of taking care the environment. But even so, the advancement of humanity, despite the small temporary drawbacks such as wars, conflicts are inevitable.

Drawing conclusions from this exponential increase in technological achievements, we are not many industrial revolutions away from becoming an "autotroph" humanity that doesn't have to struggle for energy… but can we really function detached from our struggle for survival?

1.2 Floating wind in the energy sector, the bigger picture

Renewable energy is the forefront in the process of decarbonizing the global energy production. Starting with hydropower in 1900s and going on with wind, solar energy, and biofuels, we reached at a point in 2021 where renewable energy sources account for 6.08% of the total world primary energy production as has been reported by BP statistical review [11].

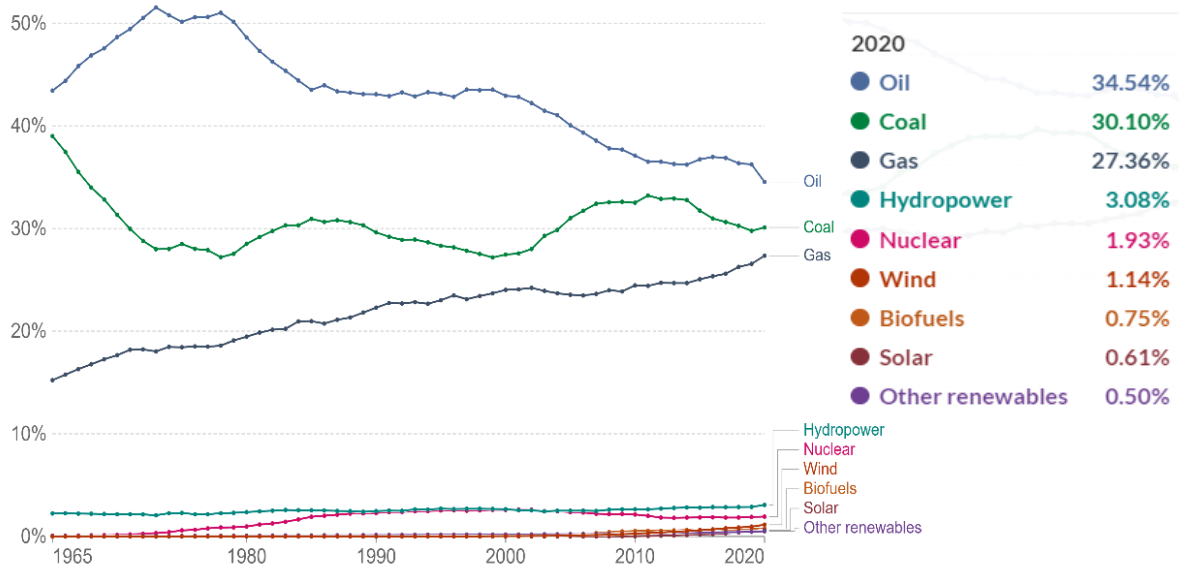

Figure 1-1 Primary energy production by source [12]

In Figure 1-1, we can see the primary energy production percentage of all the available sources. It's worth noting that the primary calculation accounts also the heat losses of the fossil fuel energy process plants. Considering that the efficiency rate of these plants varies from 33% to 41% [11], the rest of energy is lost in the atmosphere as heat. The finally consumed energy percentage per source after deducting these losses is shown in Figure 1-2.

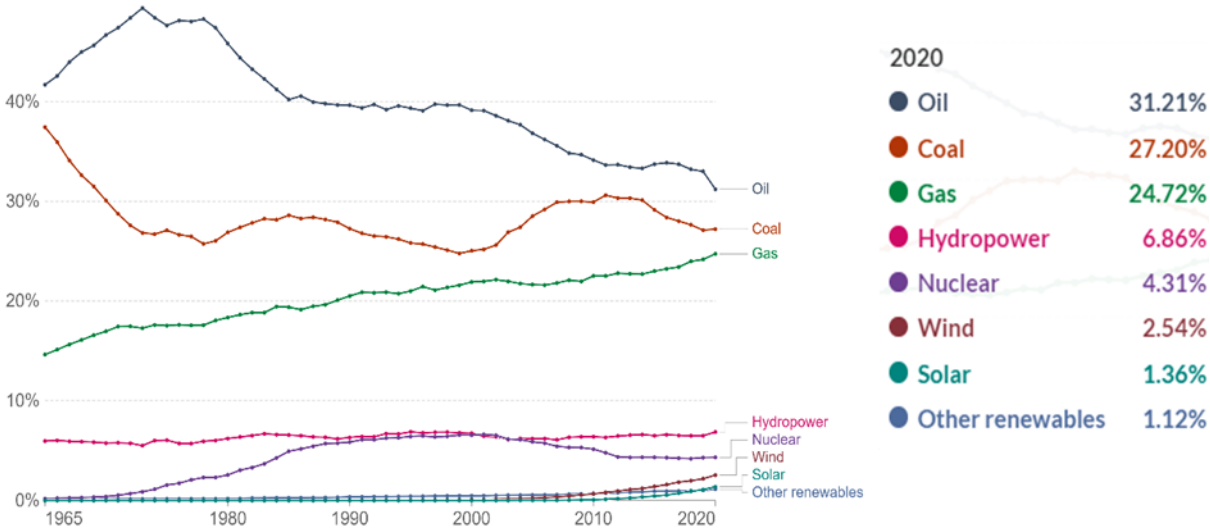

Figure 1-2 Energy consumption by source [12]

After deducting the fossil fuels' losses, the renewable energies account for 11.88% of the consumed energy. The power factor of renewables is quite large thus neglected, that's why after the deduction of losses, the fossil fuels reduce in percentage while the renewables consumption percentage is almost doubled. The first impression from the first two graphs is that renewables are nowhere close to taking over the global energy production and indeed they are not, and it can be proven utopic or even catastrophic believing so and trying to enforce it. The role that renewables should aim is to satisfy the increase in energy demand.

The largest increase in demand can be seen at Asian countries such as China and India that are mainly producers. In Figure 1-3, the increase in electricity demand from all G20 nations is presented.

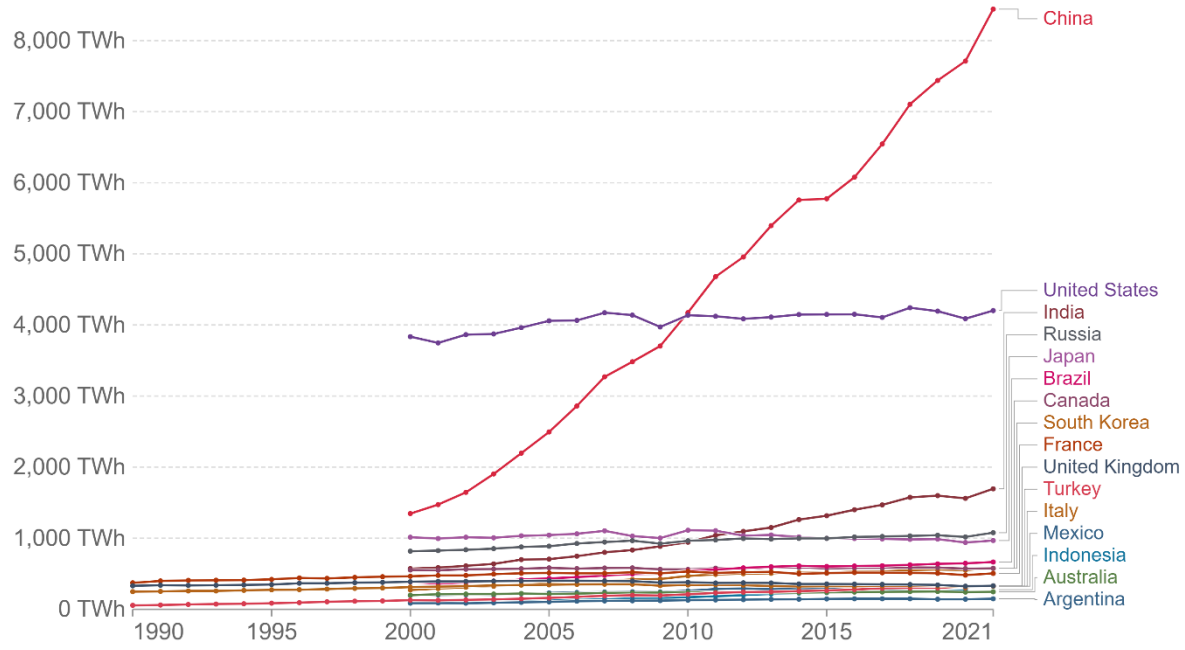

Figure 1-3 G20 nations electricity demand [12]

To decarbonize energy production, the first goal should be a simultaneous halt in energy demand increase and making sure that any excess energy needed will be satisfied from renewable energies. The focus should be on the big countries that keep expanding both population wise and production wise. Decarbonizing selectively few small countries will not solve the environmental problem as long as the heavy producing countries are using fossil fuels to power their enormous production infrastructure.

As we can see in Figure 1-4, still to this day wind power is the second largest renewable source after hydropower and makes up 21.38% of the total. This can be explained mainly by the fact that hydro dam technology developed earlier than wind turbines and was more reliable.

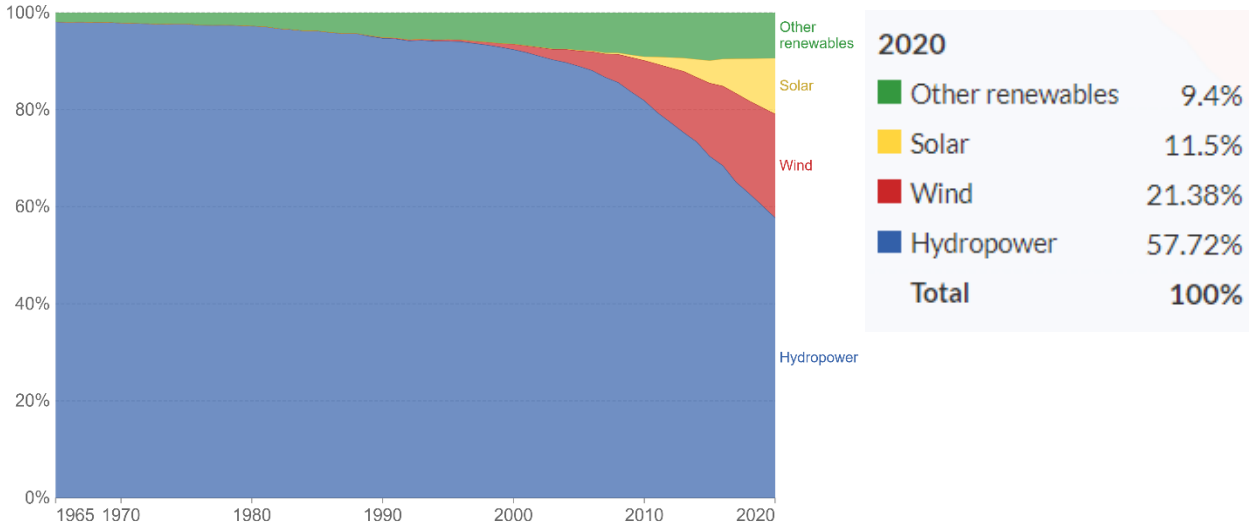

Figure 1-4 Worldwide renewable energy generation [12]

The percentage of 21.38% includes both onshore and offshore wind turbines with the offshore turbines producing up to 6.8% of the total capacity as has been reported by IRENA and shown in Figure 1-5.

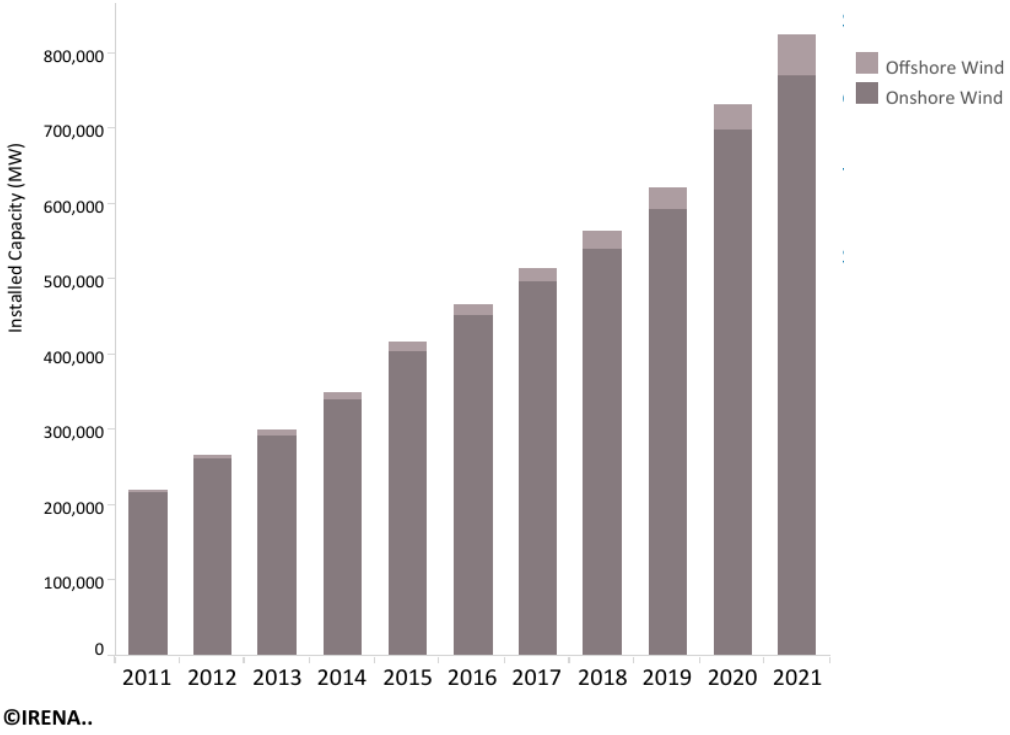

Figure 1-5 Offshore wind turbines installed capacity [13]

Included in this 6.8%, as to this day this paper is written, there are only 16 floating fully scaled floating wind turbines connected to the grid worldwide. The first wind park was the Hywind Scotland owned by Equinor and Masdar [14] consisting of 5 turbines, followed by the WindFloat Atlantic consisting of 3 turbines [15] and lastly the Kincardine consisting of 6 turbines [16]. There are also two standalone demonstration floating turbines produced by Ideol and deployed in France and Japan [17].

There are numerous merits in transiting to floating wind turbines. The most important reason is the fact that there is an abundant amount of wind energy in the oceans far from the shores. Figure 1-6 is a snapshot from the World Wind Atlas [18] and depicts the wind power density across Norway is presented. The readings refer to 100m altitude from sea level. The buffer zone starting from the shoreline has 200km length.

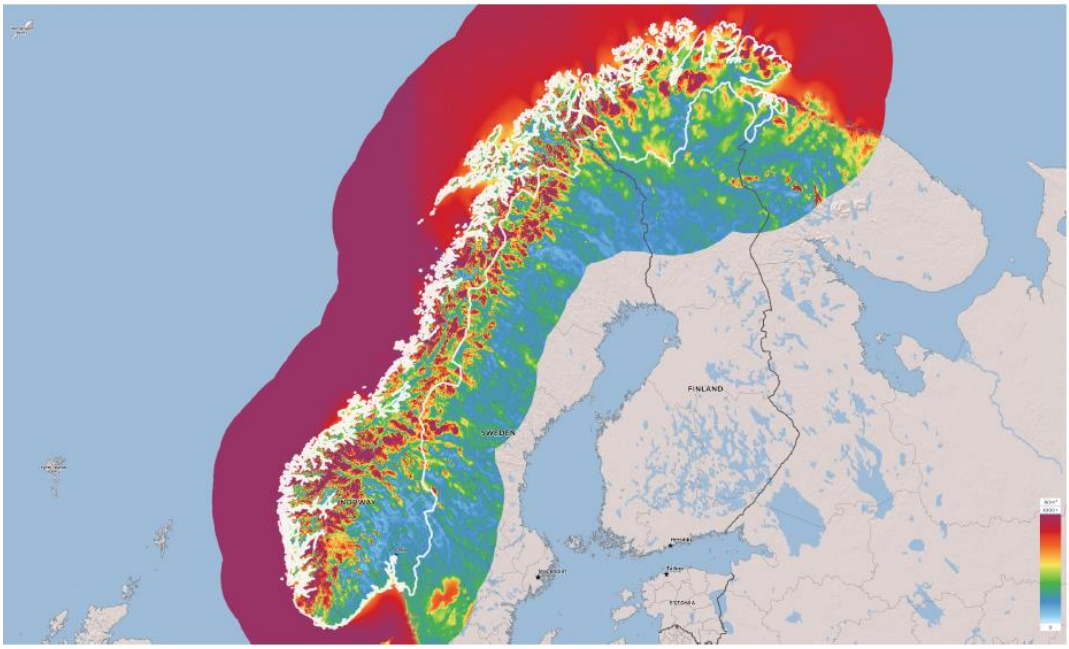

Figure 1-6 Wind power density in the Norwegian continental self [18]

Another important reason is the quality of the wind profile. Given the fact that there are no obstructions on the sea, the wind direction doesn't change that often and with the combination of low surface roughness, a higher wind consistency is observed. Besides the technical reasons, there are also many environmental concerns. Wind turbines have been blamed for interfering with major birds' migration routes. There is a direct physical threat when birds collide with the rotor blades and indirectly, in the long term their migration pattern might change exposing them to harsher conditions that usual. Fox et al. [19] have studied the birds' behavior inside the area and in the periphery of onshore and offshore wind parks. The consensus, as it has been reported

by Petersen and Fox [20], is that moving to isolated areas by utilizing floating turbines will reduce the environmental impact in the fauna. There is another important aspect also regarding the aesthetics of wind farms. Onshore and offshore bottom-based wind farms have been heavily criticized for altering the landscape and posing a visual disturbance to nearby communities. Regardless the validity of the objections against wind turbines being installed close to populated areas, it would create less tension if the wind parks were installed far from eyesight.

As every other technology that hasn't step up to massive production, floating wind turbines have a high manufacturing and maintenance cost. This leads us to the main drawback of the floating wind turbines which is the substantially high LCoE (levelized cost of energy). Energy produced from onshore wind turbines and offshore monopile turbines cost 1/3 and 2/3 of the cost of floating turbine energy respectively. Since the first project, Hywind Scotland in 2016, and up to this day, these projects are all economically unviable but it's the future potential that drives companies investing money in the development of this technology. The initial assessments in 2013 performed by Myhr et al. [21], when the Hywind Scotland park was announced, predicted an LCoE between $93 and $268 per megawatt-hour. [21], when the Hywind Scotland park was announced, predicted an LCoE between $93 and $268 per megawatt-hour. The current LCoE values, as they were reported in 2020 by the National Renewable Energy Laboratory of the USA [22], are 37 $/MWh for a reference 6.1 MW onshore turbine, 85 $/MWh for an equally large bottom fixed offshore turbine, 132 $/MWh for a 6.1 MW floating turbine, and the most interesting part is that a residential distributed project with 20 Kw wind turbine has an LCoE of 159 $/MWh. A small footnote here is the observation that while projects are scaling up, the price of the produced energy is drastically reduced. With the rate that prices are reducing, Tønset in his article in Norwegian SciTech News [23], predicts that floating wind turbines will reach the bottom fixed turbine LCoE in 2030 and Ebbesen on behalf of DNV [24], predicts that floating wind turbines will achieve a LCoE of 40 $/MWh in year 2050. The main advantage of the floating turbines is the reduced offshore installation time, as they are assembled close to the shore and tugged out in open sea.

As offshore floating wind is still in the early commercially developing stage, there is not a predominant design in the market. In Figure 1-7, the most common designs including bottom fixed are presented. Starting from left to the right, the monopiles are the most economical choice for shallow water. The main problem is that with increasing depth, the diameter of the pile should increase. So, the typical pile diameter of 7.5m is designed for 35m depth installation as has been reported by Kallehav et al. [26]. Petersen, director of business for offshore wind at engineering

consultancy Ramboll Wind predicts that monopiles can be designed for up to 60m depth with 10m diameter, increasing though significantly the production cost [27].

Indicative of the trend around monopiles is that, as it is reported on the official dodger bank website [28], 90% of the 9 GW Dogger Bank development is below 35m. Tripod and Jacket

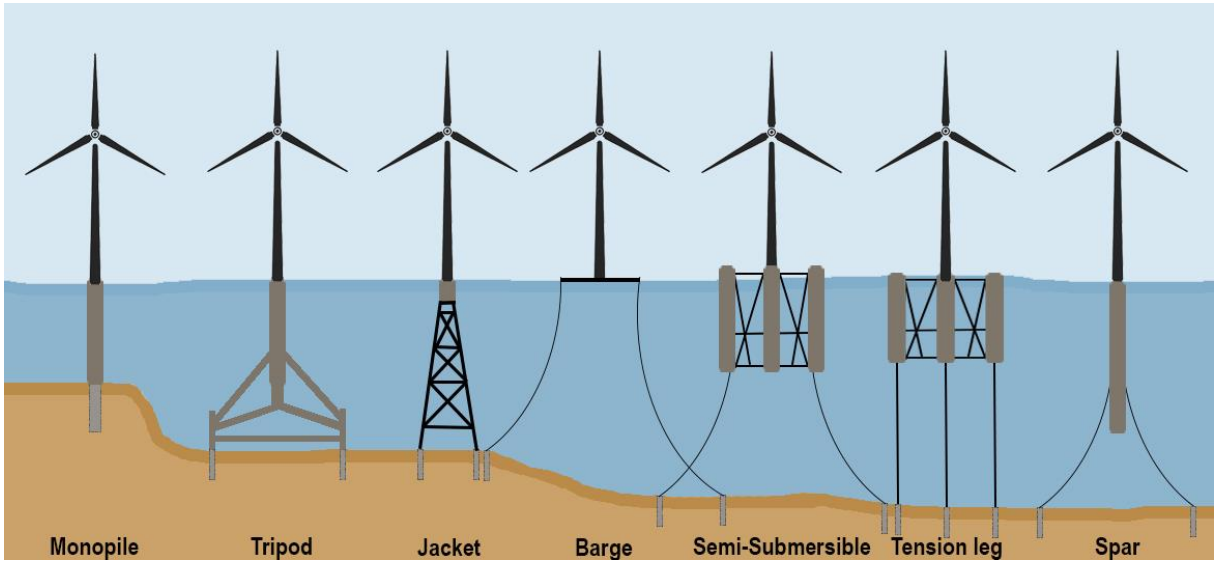

Figure 1-7 Offshore floating and bottom fixed alterations provided by Clarus Offshore [25]

structures are the next step moving deeper. The last tripod was installed in wind park "Globe Tech 1" wind park, 9 years ago in the German North Sea. Even though it was considered an abandoned project, Sif [29] in collaborations with Smulders [30] will start producing tripods up to 70m depth in 2024. The main reason for shifting to tripods is the depth increasing complexity and price of Jacket structures. This intermediate depth from 50m to 70m it's an interesting ground because the fixed structures are getting too expensive and complex, and the floating structures cannot be traditionally moored neither with catenary, because the suspended mooring length doesn't create enough pretension, nor with taut mooring, as the reduced rope length will result in high tension with relatively small offsets.

The leading condition that will decrease the floating wind LCoE, business wise, is the widespread deployment of floating turbine. This thesis though, is a prompting to the cost cutting effort from the technical aspect.

The following proposed concepts are the legs of a twofold solution to both LCoE reduction and intermediate water depth deployment of floating wind turbines. Focusing primarily in maximizing the energy production of the floating structure, a novel concept of combining a floating wind turbine with two types of wave energy converters is proposed. Following the

surplus energy calculation of the concept, a hybrid catenary mooring arrangement for 50m depth is proposed and its behavior is tested.

The combined concept name is Semi-Submersible, Torus and Flap Combination (STFC). A front view of it is presented in Figure 1-8.

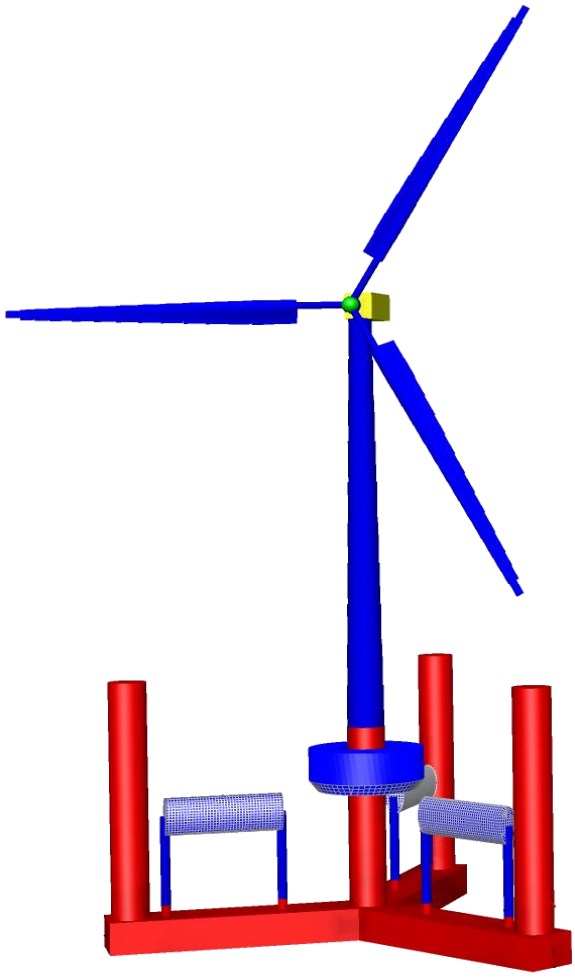

Figure 1-8 STFC

The floating foundation is called CSC, and is a semi-submersible presented by Luan et al. [31]. The middle column wave energy converter is a two-point absorber called Torus that functions taking advantage the different heave response of the floater and itself. The design is based on the original concept developed by Wavebob Ltd [32] from 1999 to 2013. The three flap-type wave energy converters are a variation of the bottom hinged surge energy converters as presented by the National Renewable Energy laboratory [33] and the floating surge wave energy converters described by Li et al. [34]. The present flap configuration and shape were presented by Luan et al. [35]. The wind turbine is a generic 5MW NREL horizontal axis reference turbine presented by NREL USA [36].

Starting from the installation of wave energy converters, it should be noted that wave energy extraction is something that hasn't scale up yet to massive production and the standalone projects existing have a higher LCoE than other renewable energies as reported by Aderinto et al. [37]. At first sight it seems oxymoron how adding a less efficient technology to a more efficient will increase the efficiency of the later. Examining though the aspects that make wave energy converters inefficient it can be noted that the marine operations involved, and mooring are a significant cost. The idea behind installing wave energy converters on the floater is that we can take advantage of the existing infrastructure, power cables, mooring arrangements, and floating support structure, to install an otherwise non profitable standalone wave energy converter. There is a two-fold benefit also in this act. The first is the obvious reduction of the LCoE and the second is the environmental benefit of absorbing the maximum possible energy for the given space a structure occupies in nature. The concept of harvesting multiple sources of energy using one structure is not something new and by carefully watching the development of new designs such as FlexiFloat presented by Rosenberg [38], Poseidon Wave and Wind system described by McTiernan et al. [39], and Denmark's Energy Islands proposed by the Danish Energy Agency [40], it is relatively safe to predict that the next step of green energy will be the transition from the concept of a single energy source capturing, such as windfarms, to the greater picture of multisource energy harvesting farms-hubs. These hubs can act as the energy provider, in the form of electricity or hydrogen produced by the multiple sources of electricity for coastal communities, whilst remaining far from urban and rural areas as has been addressed by the Danish Energy Agency [40]. These energy hubs should be arranged in dense, compact and space saving configurations to minimize costs. The STFC concept aims to contribute towards this designing philosophy.

At the second phase of this thesis, a hybrid mooring arrangement called CCCB is proposed. CCCB stands for Clump-Chain-Clump-Buoy. The arrangement is a combination of two proposals by Xu et al. [45] presented in Figure1-9.

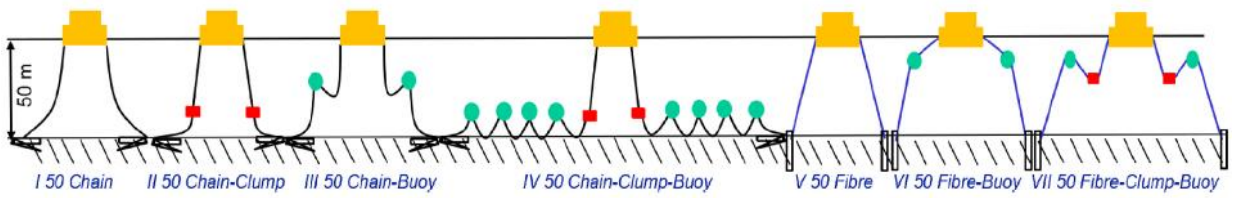

Figure 1-9 Mooring configurations proposed by Xu et al. [45]

The thesis proposed concept is a combination of the III 50 Chain-Buoy design and the IV 50 Chain-Clump-Buoy designs. Schematic drawing presented in Figure 1-10 and Sima extracted snapshot is presented in Figure 1-11.

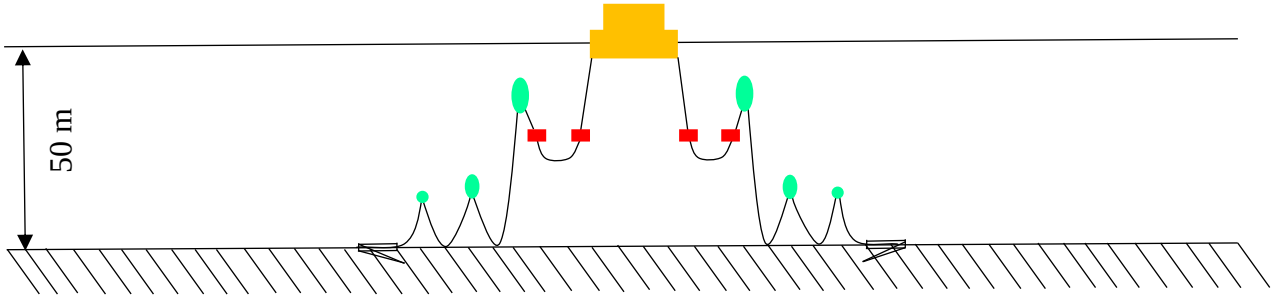

Figure 1-10 Hybrid mooring CCCB Clump-Chain-Clump-Buoy

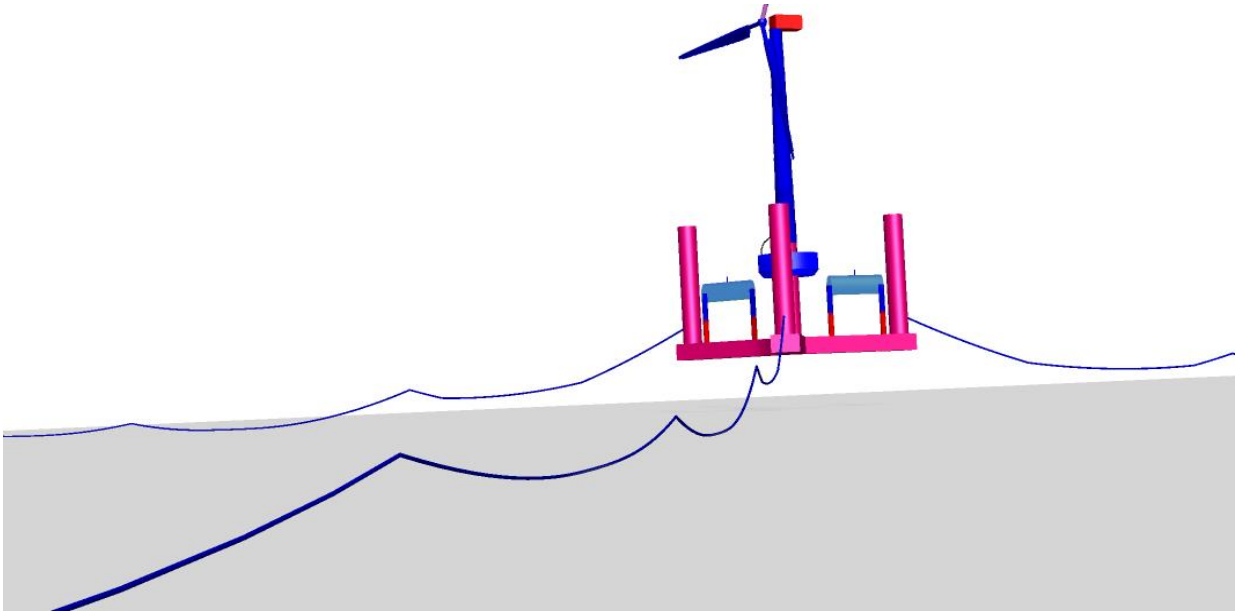

Figure 1-11 Hybrid mooring CCCB

1.3 Literature review

The combination of wind and wave energy is a concept that has been addressed by many other researchers before. A combination of flaps and a wind turbine placed on a semi-submersible called SFC has been proposed by Luan et al. [35]. Muliawan et al. [41] has presented a novel concept about a spar floating wind turbine, equipped with a torus wave energy converter. Following, Soulard et al. [42] proposed the installation of a wind turbine on a floating cylindrical barge, equipped with heave oscillating floaters. Another concept of combining an existing structure with a wave energy converter has been proposed by Aubault et al. [43]. The project consists of a wind turbine installed on the WindFloat floater and equipped with a heave wave energy converter. Finally, Bachynski et al. [44] presented a combination of heave point absorbers and a TLP based floating wind turbine.

The idea of clump weight addition was introduced in 1976 by Finn et al. [46] for the mooring of a deep-water compliance tower. Mavrakos et al. [47] in addition has proven that the proper number, size, and location selection of buoys can reduce the mooring line dynamics in deep water applications. The same buoy principle was tested in 50m depth from Fitzgerald and Bergdahl [48] for the mooring purposes of a two-point wave energy converter. The buoy utilization resulted in reduced cable weight, influence on the floater and mooring loads. Getting closer to the proposed floater concept, Yuan et al. [49] proposed a new deep water hybrid mooring design consisting of a buoy placed close to water surface and a set of three clump weights placed close the sea bottom. The difference between a simple chain catenary and a hybrid catenary with clump weight or buoy was tested by Vicente et al. [50]. The application was a floating-point absorber, and the outcome was that the main effect of buoys and clump weight configurations is mainly on the average and maximum mooring tension and less on the horizontal motion and absorbed power

1.4 Objectives and outline of the thesis

The main scope of the thesis is to investigate the feasibility of the two proposed concepts. The first concept is the combination of a floating wind turbine with wave energy converters called STFC and the second one is an intermediate water hybrid mooring system called CCCB. The sub-scopes of thesis are listed below:

1.4.1 STFC concept

- To establish a numerical model of the STFC, SFC [35] and CSC [31] in deep water 200m.
- To carry out decay tests and compare the results among the different models.
- To carry out regular wave tests on the numerical models of both SFC and STFC to evaluate the response RAOs of the supporting platform and the WECs.
- To establish 6 sets of environmental cases, which are the combination of turbulent wind and irregular waves in an operational condition.
- To perform one-hour duration of dynamic simulation with five random wind seeds for each environmental case.
- To investigate the dynamic responses of STFC and compare them with CSC, conclude if the WECs influenced the platform in such extend that redesigning of mooring is required.
- To calculate the mean power production of STFC.
- To calculate the annual power production of STFC and CSC and compare the results.

1.4.2 CLUMP-CHAIN-CLUMP-BUOY (CCCB) concept

- To establish a numerical model of the STFC in intermediate water depth 50m, pointing out the differences with Xu et al. [45].
- To define the new mooring concept characteristics, line length, clump weight, buoy sizing.
- To establish 5 sets of environmental cases, which are the combination of turbulent wind and irregular waves and current in operational and parked condition.

- To perform one-hour duration of dynamic simulation with six random seeds for each environmental case.
- To investigate dynamic responses and mooring line tension statistics during operational and parked conditions.
- Draw conclusions on the feasibility of the proposed concept and evaluate it against Kun Xu's IV 50m Chain-Clump-Buoy.

Chapter 1: The motivation of thesis and a few thoughts about the future of renewable energy are given. A positioning of renewable energy amidst the energy sector is attempted. The proposed concepts of thesis are presented followed by the literature review for each concept.

Chapter 2: The main theory of this study and the governing equations are presented.

Chapter 3: Details related to the numerical modeling of STFC are given. The environmental conditions for the global analysis and mean power are introduced. In addition, the extended environmental condition grid for the annual power production is presented.

Chapter 4: Details related to the numerical modeling of the new hybrid mooring concept CCCB.

Chapter 5: Results and discussion of dynamic analysis results of STFC compared with CSC. The mean and annual power performance are presented and compared with CSC.

Chapter 6: Results and discussion CCCB.

Chapter 7: A summary of the thesis is included in this chapter. The main conclusions

and the feasibility of each proposed concepts are addressed here.

Chapter 8: The last part includes the recommendations for the future work of the thesis.

2 THEORY

In this stion the theory and the governing equations are presented. In the beginning the theories of wind and wave are presented. Following, the hydrodynamic loads of the structure are explained. At last, basic floating stability theory is presented and basic catenary equations are explained.

2.1 Modeling of wind and wave

This stion discusses the wind field generation theory and wave profile. This Thesis uses a turbulent wind model and an irregular wave model to account for the stochastic fluctuations of wind and wave. Wind and wave spectra are applied to determine the frequency distribution of energy. The wind and wave spectra are then used as inputs for additional aerodynamic and hydrodynamic load calculations.

2.1.1 Wind

The wind profile starting for the sea surface is described by the power of law formula. This formula is a rough estimation that considers only the surface roughness. The mean wind speed at specific height can be obtained by the following equation presented by Jonkman et al. [51].

$$U(z) = U(z_{ref})(\frac{z}{z_{ref}})^{\gamma} \quad (1)$$

Zref is the hub height and in this case is 90m. U(zref) is the mean wind speed at Zref and U(z) depends on the γ factor. γ is defined as 0.14, is based on the surface roughness and follow the IEC 61400-1 Class C guidelines [51]. The wind field used in this thesis is a turbulent wind field meaning that there are gust winds and changes in pressure and wind velocity throughout the time series. The quantification of these violent changes is called turbulence intensity, is proportionate to standard deviation of the mean wind speed and disproportionate to the mean wind speed.

$$I = \frac{\sigma}{\overline{U}} \quad (2)$$

The turbulence characteristics vary with the wind speed and wind height. The lower the mean wind speed, the higher the turbulence will be because of the increased standard deviation. IEC 61400-3 [52] gives the formula for calculating the standard deviation.

$$\sigma_u = \frac{u_{hub}}{\ln\left(\frac{z_{hub}}{z_o}\right)} + 1.28 \times 1.44 \times I_z \tag{3}$$

Using the above formula, the software TurbSim [51] will generate random timeseries of wind fields. The turbulence model followed is the Kaimal filter that is described by a velocity spectrum. The formula of the spectrum is presented below.

$$S_k(f) = \frac{4\sigma_k^2 . L_k/u_{hub}}{(1 + 6f . \frac{L_k}{u_{hub}})^{5/3}} \tag{4}$$

k = u, v, w
$f = cyclic\ frequency$
$\bar{u}_{hub} = mean\ wind\ speed\ at\ hub\ height$
$\sigma_\kappa = standard\ deviation$
$L_k = integral\ scale\ parameter\ proportional\ to\ turbulence\ scale\ parameter\ \Lambda_U$

The minimum value between Zhub and 60meters can determine the turbulence scale parameter.

$$\sigma_v = 0.8\sigma_u \tag{5}$$
$$\sigma_w = 0.5\sigma_u$$

$$L_k = \begin{cases} 8.10\Lambda_U, & k = u \\ 2.70\Lambda_U, & k = v \\ 0.66\Lambda_U, & k = w \end{cases} \tag{6}$$

$$\Lambda_U = 0.7 \times min(60m, z_{hub}) \tag{7}$$

The Kaimal turbulence model has neutral stability thus the Richardson number is zero. This means that the velocity spectra created is invariant across the whole grid. The grid height and width can be specified in TurbSim according to the rotor diameter of each turbine and the hub height.

$$Ri = \frac{\frac{g}{T_V}\frac{\partial \theta_v}{\partial z}}{\left(\frac{\partial U}{\partial z}\right)^2 + \left(\frac{\partial V}{\partial z}\right)^2} \tag{8}$$

A small variation though of the standard deviation in longitude direction is present due to spatial coherence as has been reported by Jonkman et al. [51]. The coherence formula is presented below.

$$Coh_{i,j} = exp\left(-a\sqrt{\left(\frac{f * r}{\bar{u}_{hub}}\right)^2 + \left(0.12\frac{r}{L_c}\right)^2}\right) \tag{9}$$

f = frequency
r = distance between the points i and j
α = coherence decrement = 12
L_c = coherence scale parameter = $5.67 * \min(60\text{m}, z_{\text{hub}})$

Except the coherence u, the rest v and w components are not specified by IEC standards, they are considered as zero and their standard deviation will cover the whole wind grid.

2.1.2 Waves

Both concepts of the thesis are designed for the North Sea. In order to generate new random wave realizations, the Jonswap spectrum is used. This spectrum is a result of data collected between 1968 to 1969 from an offshore site in the North Sea. The definition of the spectrum is given by Hasselman et al. [53] and is given below. γ and β are set to 3.3 and 1.5 respectively.

$$S_\xi(\omega) = \frac{\alpha g^2}{\omega^5} exp\left(-\beta\left(\frac{\omega_p}{\omega}\right)^4\right)\gamma^{\exp\left(\frac{(\omega/\omega_p - 1)^2}{2a^2}\right)} \tag{10}$$

$$\alpha = \left(\frac{H_S {\omega^2}_p}{4g}\right)^2 \frac{1}{0.065\gamma^{0.803} + 0.135} \tag{11}$$

$$\sigma = \begin{Bmatrix} 0.07 & \omega < \omega_p \\ 0.09 & \omega > \omega_p \end{Bmatrix} \tag{12}$$

$$\omega_p = \frac{2\pi}{T_p} \tag{13}$$

$$\sigma = \begin{cases} 0.07 & \omega < \omega_p \\ 0.09 & \omega > \omega_p \end{cases} \tag{14}$$

The main parameters affecting the energy spectrum is the wave height Hs, the peak period Tp and the γ peak size parameter.

2.2 Hydrodynamic loads

2.2.1 Potential flow theory

Wave-induced movements and loads may be represented to a significant degree by linear theory, which can be used to semi-submersibles, ships, and other large volume structures [54]. According to linear theory, the wave-induced movements and stresses on a structure are proportional, on a linear scale, to the amplitude of the wave that is striking the structure. The theory of linear waves also suggests that the wave steepness, which is the wave amplitude divided on the wavelength, is relatively low, which indicates that the waves are still a long way from breaking. In addition, the wave kinematics are only accurate up to the level that is considered to be the mean water level. The assumption made in this research is that the potential flow theory, which depicts the velocity field in a fluid as the gradient of a scalar function and refers to it as the velocity potential, accurately represents the fluid under investigation. In order for potential flow theory to be applicable to a fluid, the following three conditions must be true: the fluid must be inviscid, irrotational, and incompressible [55]. The results of a structure in irregular seas are derived by linearly superimposing the results of regular wave components. This is possible because irregular seas have waves that are not perfectly regular. This indicates that it is adequate, hydrodynamically wise, to study a structure in incident sinusoidal waves with a minor wave steepness since the waves are not too steep [56]. In the case of regular waves, the hydrodynamic issue is often broken down into two, the diffraction problem and the radiation problem as is reported by Faltisen [54].

- The diffraction problem refers to the forces and moments that operate upon the body when the structure is prevented from vibrating and regular waves are heading onto it. The hydrodynamic loads that are responsible for the forces and moments are referred to as wave

excitation loads, and they may be subdivided into diffraction forces, moments and Froude-Kriloff forces

- The radiation problem, also known as the forces and moments that are exerted on the body when the structure is pushed to oscillate in water. There are no waves that are coming onto the structure, and the hydrodynamic loads are the added mass, damping and restoring terms.

A schematic representation of the two problems is presented in Figure 2.-1

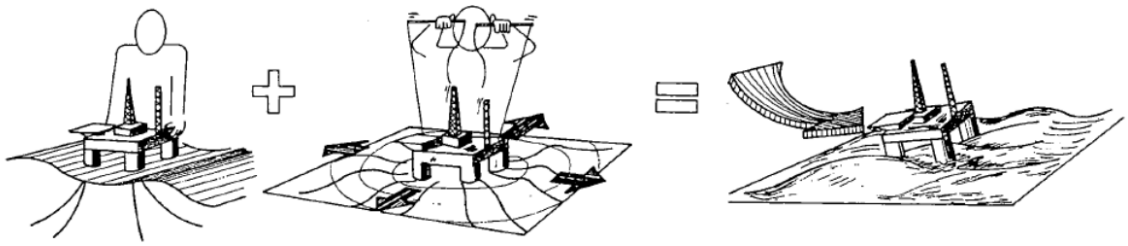

Excitation loads | Added mass, Damping, Hydrostatics | Motion response

Figure 2-1 Diffraction and radiation problems [54]

2.2.2 Morison equation

The wave forces that act on a structural component that has a circular cross stion are calculated using Morison's equation. The two basic components are the mass force and the viscous drag force. The mass force is determined by potential theory, and its magnitude is directly proportional to the acceleration of the undisturbed fluid. If the body is moving, it is possible to further expand the mass force to include two terms. These are the Froude–Krylov force and the hydrodynamic mass force. According to Morrison's equation, the horizontal force dF that acts on a unit length of circular cross stion may be computed as follows:

$$dF = dF_M + dF_D = \rho \frac{\pi D^2}{4} C_M a_x dz + \frac{1}{2} \rho C_D D u|u| dz \quad (15)$$

ρ = water density
D = cylinder diameter
C_M = mass coefficient
C_D = drag coefficient
u = velocity of the water particles
a_x = acceleration of the water particles

2.3 Mooring system

The mooring system used in this thesis is the catenary arrangement. The advantage of catenary mooring is the fact that the mooring line is not under tension. The restoring forces on the floater are induced by the free hanging weight of the line. The catenary shape is changing according to the weight of the line and the position of the floater. The surplus force needed to bring back the floater is coming out of the mooring line being lifted of the seabed. In every possible floater position, the geometry can be found by the following formula.

$$y = \frac{H}{W}\left(cosh\frac{W}{H}x - 1\right) \tag{16}$$

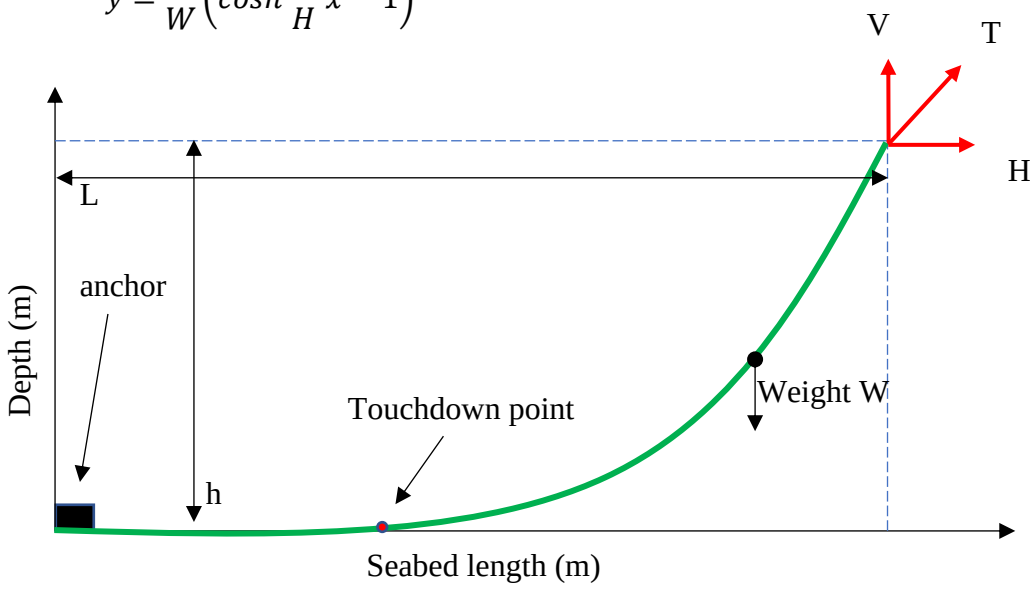

Figure 2-2 Catenary shape and forces

The formulas bellow are from Marine and Operations book by Gudmestad [57]. With these series of formulas, the relevant forces and the important points of the catenary arrangement can be calculated. V is the vertical tension, S is the suspended length from top till the touchdown point, L is the horizontal distance from the anchor till the floating structure. H and V are the horizontal and vertical component of the line tension, h is the water depth and W is the submerged mooring weight.

Length of catenary $$S = \frac{H}{W}\left(sinh\frac{W}{H}L\right) \tag{17}$$

Water depth $$h = \frac{H}{W}\left(cosh\frac{W}{H}L - 1\right) \quad (18)$$

Horizontal force $$H = \frac{W}{2h}(S^2 - h^2) \quad (19)$$

Distance to touch down point $$L = \frac{H}{W}cosh^{-1}\left(\frac{W}{H}h + 1\right) \quad (20)$$

Vertical force $$V = W \times S \quad (21)$$

Tension $$T = \sqrt{H^2 + (WS)^2} \quad (22)$$

3 NUMERICAL MODELING

The numerical modeling comprises of three parts. The first part includes details about the physical structure of the involved parts for both projects STFC and CCC. The second and third consists of the numerical modeling of the proposed concepts utilizing the SESAM package

3.1 Physical architecture

This chapter will consist of the presentation of the physical architecture of components for both concepts and after that the numerical modeling of both will be presented.

3.1.1 STFC Physical architecture

The CSC concept is a proposal by Luan et al. [31]. The floating structure consists of three horizontal, fully ballasted and submerged pontoons, oriented in a Y shape, 120 degrees from each other starting from axis x. The origin of the global axis (xg-yg-zg) is placed in the middle of the center column's diameter, at sea water level. There are 3 vertical cylindrical columns placed at the far end of each pontoon, providing the restoring forces, and a central column acting as the base for the wind turbine. The side columns can be ballasted accordingly to achieve the required draft. The central column has 10 meters freeboard while the side columns have 20 meters. The total draft is 30 meters. The semi-submersible construction is not an optimized design but a reasonable structural design for the CSC concept. The dimensions and arrangement of the semi sub are presented in Table 3-1 and Figures 3-1 and 3-2.

Table 3-1 CSC dimensions

Side col. diameter *scd*	6.5 m
Central col. diameter ccd	6.5 m
Displacement	10297.5 m^3
Operational draft	30 m

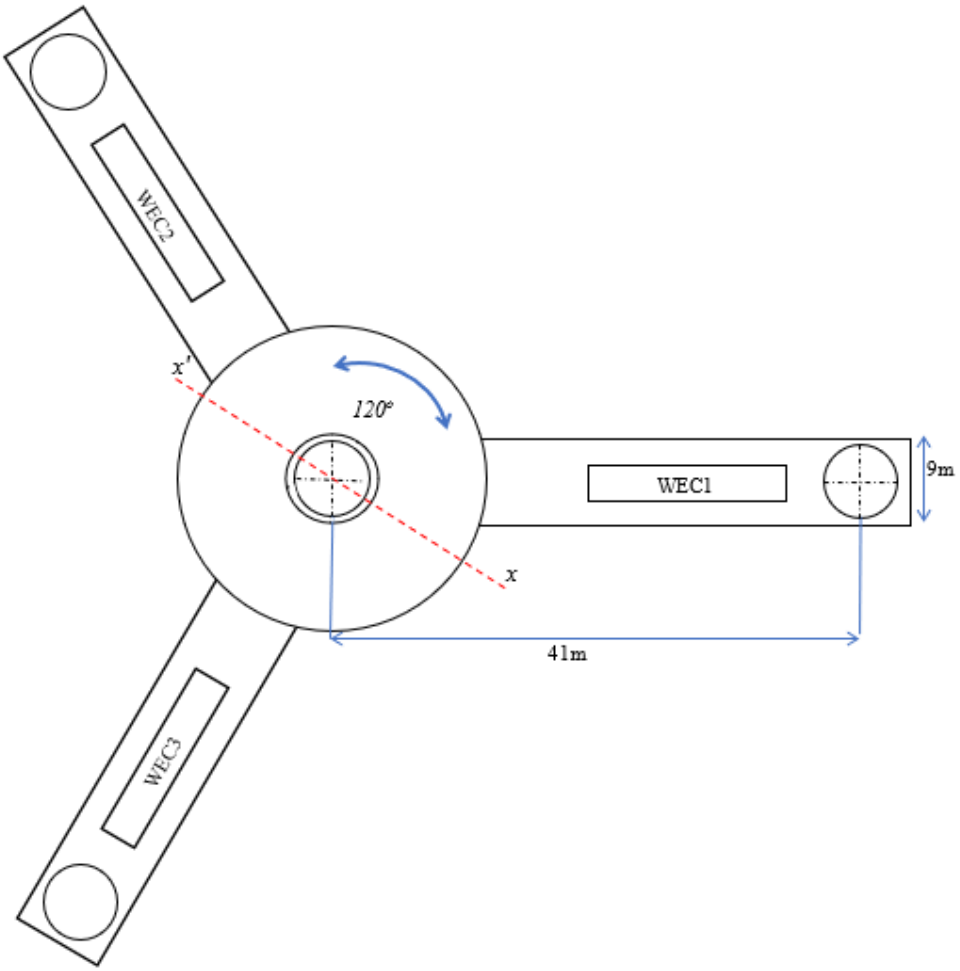

Figure 3-1 STFC zg top view

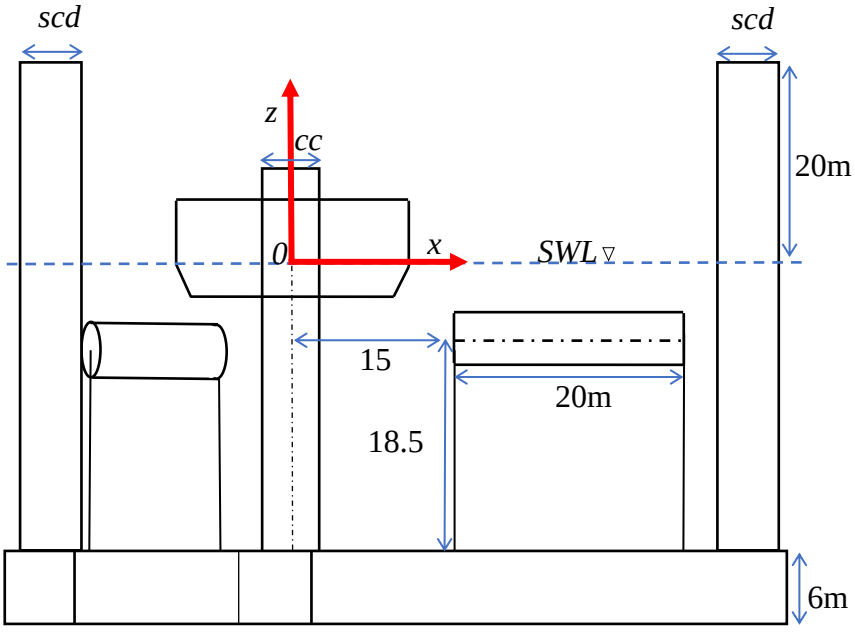

Figure 3-2 STFC yg axis view

The point absorber is placed around the central column. The diameter of the central column is equal with the diameter at sea water level of a floating spar described by Cheng et al. [58]. The idea of combining a floating spar with a point absorber has been presented by Muliawan et al. [41]. Since the cross section of the semi-sub's central column is identical with the spar, we are going to adopt roughly the same torus dimensions presented by Muliawan et al. [41] and Wan et al. [59]. The original design of the point absorber was developed by Wavebob Ltd 1999 to 2013 and presented in public by Weber et al. [32] whilst the patent has been granted to Dick [60]. It's worth mentioning that so far, the design dimensions have been estimated from available published information and may deviate from the original Wavebob concept as it has been reported by Muliawan et al. [61]. For this reason, there is a large deviation between published papers regarding the Wavebob concept. Li et al. [62] are using the Wavebob concept with mass 1,442,000 kg whereas Li et al. [63] use 966,900 kg as the mass value. On the other hand, Muliawan et al. [64] are using 418,000 kg as the weight value. The main difference between these concepts is located at the submerged part's profile which in some publications appears tapered and in others just cylindrical or tapered with a different profile. Without it being an optimized design, the following cross section x-x' depicted in Figure 3-3 will be used. It is inspired by the Wavebob Ltd media releases and its dimensions are presented in Table 3-2.

Table 3-2 Wavebob floater dimensions

Torus outer diameter	Tod	20m
Torus inner diameter	Tid	8m
Torus draft	Tdr	2m
Torus profile tip	Tpr	3m
Torus profile center	Tpc	14m
Torus freeboard	Tfb	6m
Displacement		395.84 m3
Centre of mass		-0.9m zg
Stroke length		6m

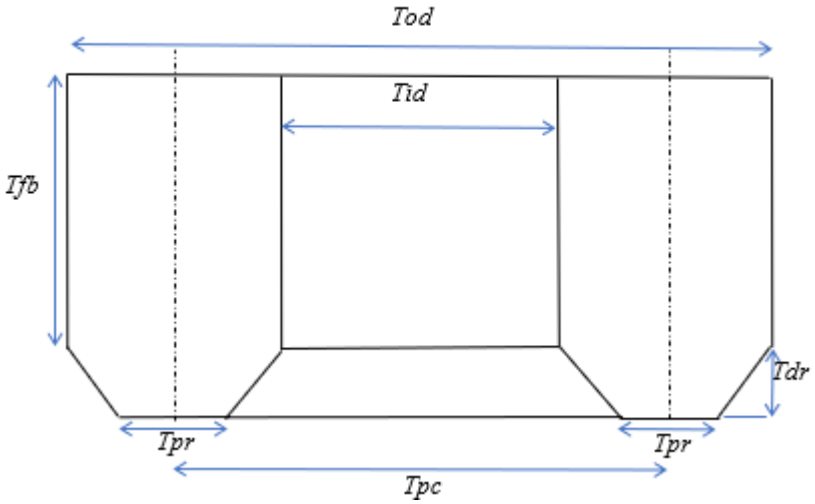

Figure 3-3 Wavebob floater cross stion x-x'

The operation principle of Wavebob is based on the different heave response of two uniaxial components reciprocating with respect to each other, a torus/donut shape volume that stays afloat, and a submerged floater. They are interconnected with a power take of mechanism (PTO) consisting of one or more hydraulic rams. The relative motion between the two objects fluctuates the ram chamber's volume thus accumulating hydraulic pressure. The pressurized fluid is being driven to a turbine, placed inside the central column, that produces electricity. The schematic drawing is presenting in Figure 3-4. In our case, the semi-sub will subsidize the submerged floater. The reciprocation function and contact forces between the column and the torus are facilitated by a bearing rail/wheel arrangement at three elevations. At the outer surface of the column there are 8 vertical rails placed at the periphery with sufficient length for the 6m stroke distance. At the inner diameter of torus there are wheels for each rail position. Except the single x y plane rail/wheel set, there are two more series of wheels in different z elevation that utilize the same vertical rails. The number of wheels ensure that there will be no change in the behavior of the torus in case one wheel fails. To ensure there will be no impact forces between the bodies, each wheel's axis is sliding in a groove and pushed against the rail with a preloaded spring. This arrangement restricts the relative surge sway roll pitch yaw motion of the torus. These data have been obtained from Muliawan et al. [41].

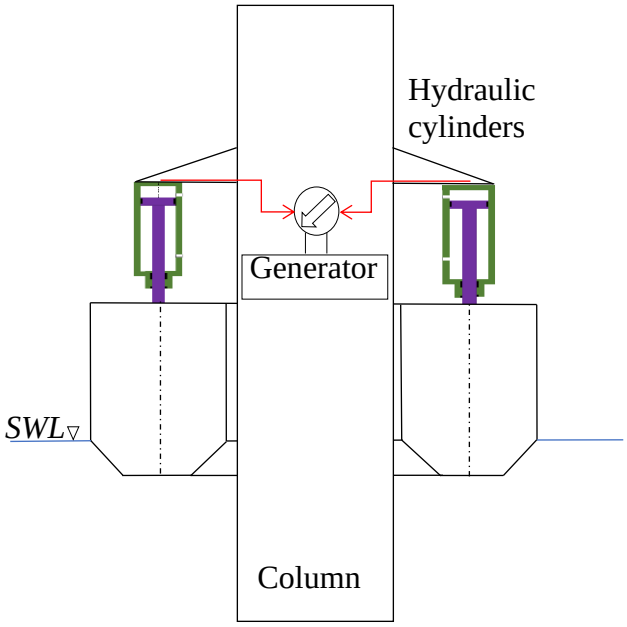

Figure 3-4 Wavebob PTO schematic diagram

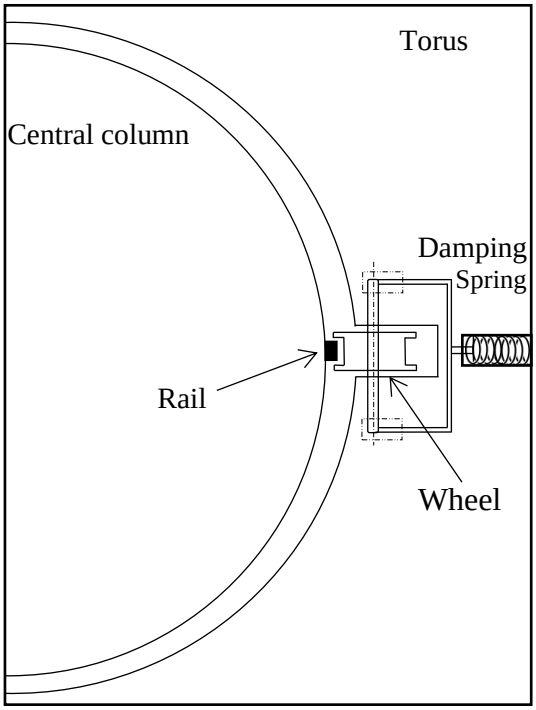

Figure 3-5 Contact rail

There are in total 3 flaps and each flap is placed above a corresponding pontoon. The flap's design is a variation of the bottom hinged surge energy converters as presented by the National Renewable Energy laboratory [65] and the floating surge wave energy converters described by Li et al. [34]. The arrangement used in this paper has been presented by Luan et al. [35]. Each flap mechanism consists of a flap that is positioned 2 meters below the mean water level and should have 15 meters distance from the center of the central column to prevent collision between the WECs. The flap has an ellipsoid cross section with 7m length major axis oriented parallel

with z_g and 3m minor axis oriented parallel to y_L axis of the corresponding pontoon. The cross section is chosen by Luan et al. [35] as the most efficient shape, following the results published by Kurniawan et al. [66], "The submerged elliptical cylinders have the best overall performance among the geometric configurations considered". Each flap weighs 100 tons and displaces 394.5 tons of water. Every flap is connected to the pontoon with two rigid arms through a PTO system. The arms follow the characteristics presented by Luan et al. [35]. Since the semi-sub is moored and the flaps are hinged through flexible joint on to it, the relative movement of the flaps, under the influence of waves, with respect to semi-sub's response, will energize the PTO mechanisms that have the same design philosophy as the torus's PTO. Flap's cross section and PTO mechanism are presented in Figure 3-6**.** The PTO arrangement presented in Figure 3-6 b) and c) is just a schematic proposal from the author and not a detailed design.

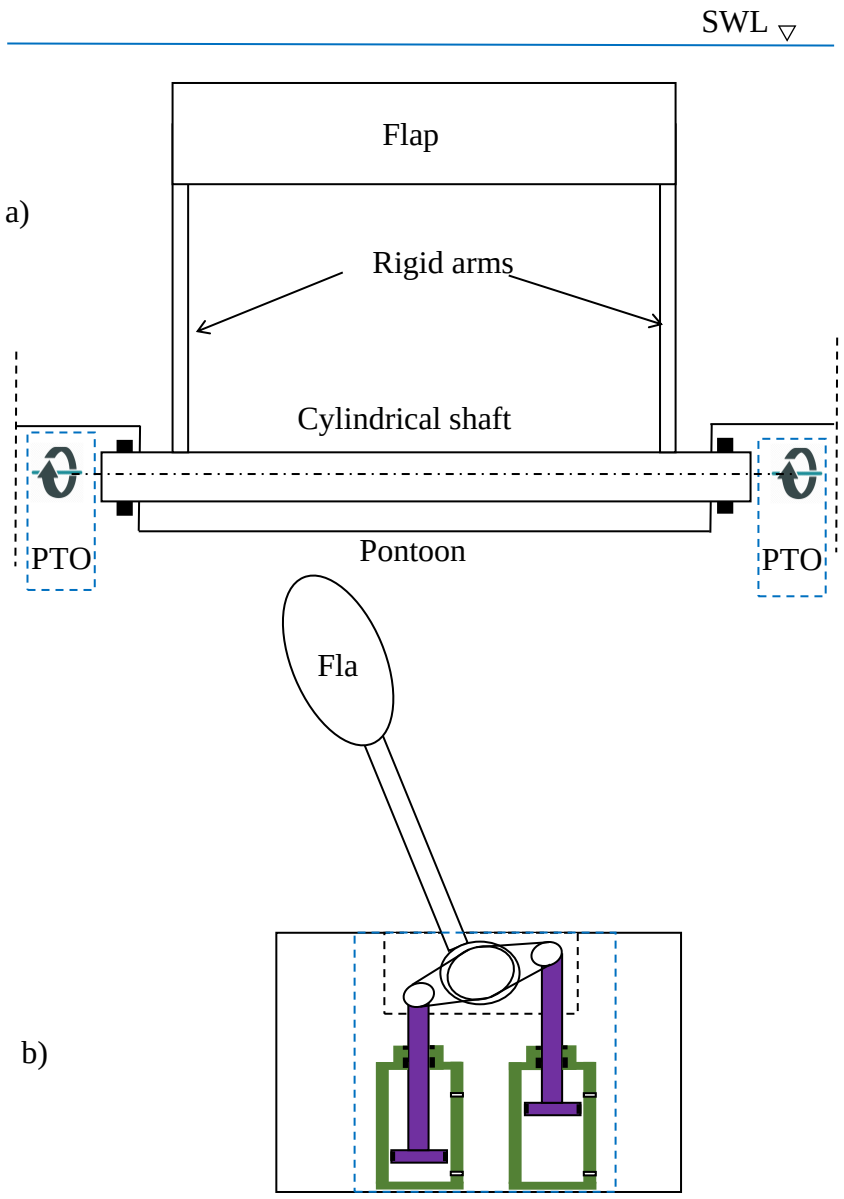

c)

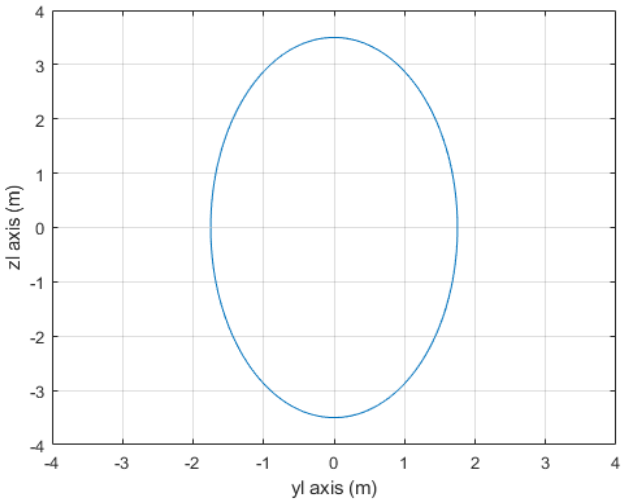

Figure 3-6 a) Flap cross stion b) Flap mechanism y_L axis view c) Flap mechanism x_L axis view

The mooring system utilizes three catenary chain mooring lines equipped with a clump weight. The orientation of the mooring lines is presented in Figure 3-7.

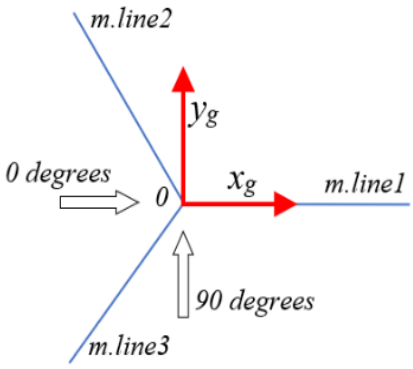

Figure 3-7 Mooring line orientation

3.1.2 CCCB Physical architecture

Before presenting the actual design of the mooring line a brief reference is made to the challenges that shallow water mooring poses. In the case of a floating structure, the rigid body motions and the mooring line tension are coupled. This is necessary for the operation of the mooring system. The static equilibrium, and the dynamic motions away from it, of the floater will force the mooring line to operate and provide the restoring forces to restore the floater to its equilibrium position. The effects that the mooring system provides to the floater are the inertia and damping effects and the restoring effects. In quasi static condition, the total restoring force is related to the geometric stiffness and elastic stiffness of the mooring line. The geometric stiffness comes from the weight and the pretension of the mooring line. The elastic stiffness comes from the mooring line elongation and it's mainly applicable at taut mooring lines utilizing elastic fiber ropes. Under dynamic motion of the floater, the mooring line motion will create a drag force ($b_D * v_x * |v_x|$) and an inertial force ($mL * a_x$) which contribute to the damping and inertial effect of the mooring line, respectively. Low frequency motions are dealt by the damping effect of the mooring line. The mooring arrangement should be stiff enough in order to reduce the motions of the floater but also compliant enough so that the tension doesn't increase above the operational limits under the influence of first order forces. The mooring of a floater in deep water is a relatively easy task, as the long-suspended mooring line provides enough pretension with relatively small top angles. The above line of thoughts is presented by Xu et al. [45].

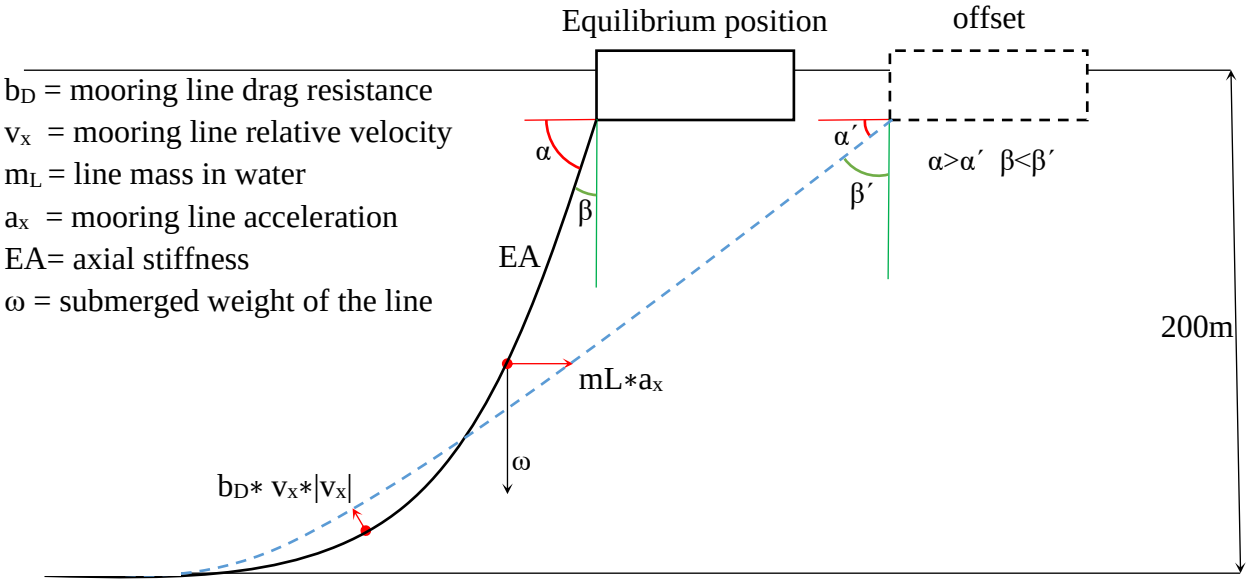

Figure 3-8 Mooring line action into effect [45].

In Figure 3-8 the mooring line action into effect is presented. The angle β is the equilibrium mooring line top angle from the vertical that is an indication of the catenary shape. The smaller this angle is, the better the catenary geometry. Moving to an offset position, the mooring line is lifted, the suspended line weight increases and this results into the restoring effect of the mooring system thus the return of the floater to the initial position. At 200m depth or any deep-water application, the movement of the mooring line will be restricted by drag forces due to the hydrodynamic interaction between the water and the mooring line and by inertia forces due to the weight under acceleration as has been reported by Xu et al. [45]. In Figure 3-9 a 50m shallow water simple catenary application is presented for the same floater and the issues arising from that are presented. The first and most obvious issue is the restricted mooring line suspended length. The first outcome of this is that the inertia forces and drag forces of such a mooring line are negligible, thus the low frequency floater motions will not be damped by the drag and inertia forces. The second outcome is that the reduced suspended length will result in reduced pretension at the fairlead if the same top angle from the vertical is used (a). So, starting with the mitigation measures for these issues, the first act is to increase the per meter weight of the mooring line, include clump weights or both. Due to the small size of the catenary shape though, the horizontal forces will be significantly reduced compared with the 200m application, so the mooring line pretension should be increased also by increasing the mooring anchors' distance from the floater (b). By doing that, we create an artificial offset of the floater but this time by distancing the anchors' position and not the floater. The only difference is that when the floater moves it's a dynamic motion and the effects of the mooring line will decrease over time when the floater returns to the equilibrium position. In contrast, when the mooring anchors' distance is increased is an act of stiffening the equilibrium position by increasing the pretension. The same effects though apply to both instances, the suspended mooring line length increases, thus the forces to the floater increase. The only disadvantage is that now the equilibrium position top angle β is increased in comparison with the 200m application, thus the initial catenary shape is of inferior geometry. This, progressively with higher floater offsets, will cause the top angle becoming to big and the mooring line being lifted completely from the ground applying pulling forces to the anchors. Even though more mooring line is laid down on the floor, the pulling effect will persist. By pulling the mooring line, the catenary effect is gone. By the moment that the line is straightened and under tensile forces, the catenary doesn't depend anymore on the weight of the mooring line but on the axial stiffness of the line. In Figure 3-9 a graphical explanation of all these matters is presented.

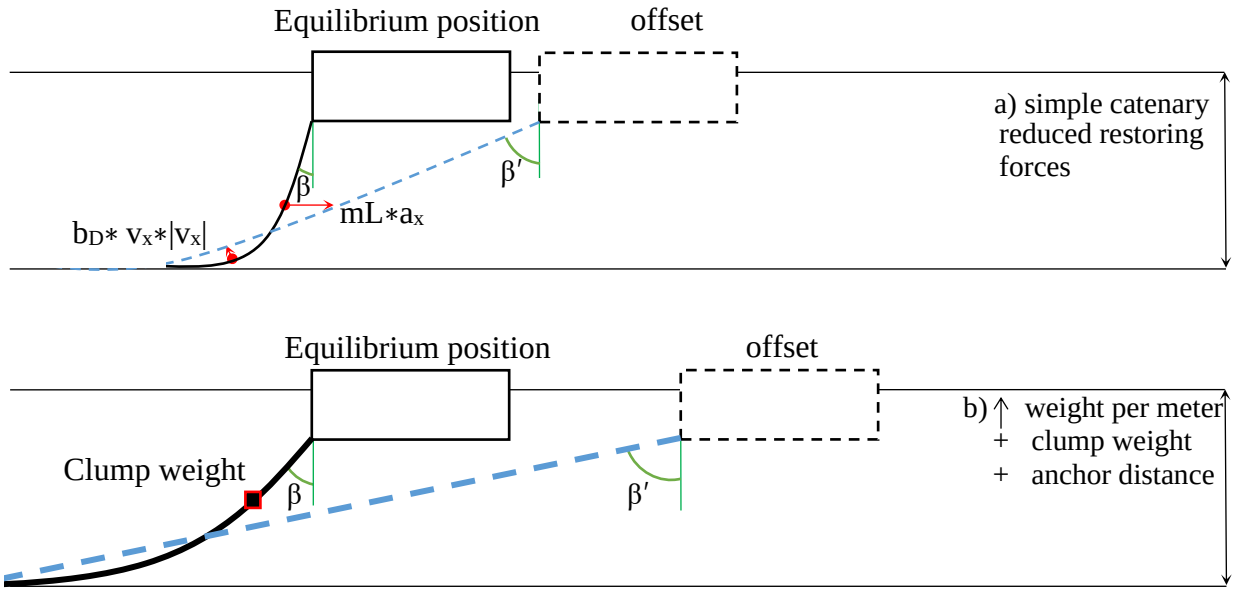

Figure 3-9 50m mooring issues' mitigation measures

Another important problem that might arise is the slacking of the leeward mooring line during severe weather conditions due to it's reduced catenary shape. In Figure 3-10 a Sima snapshot of this incident is presented.

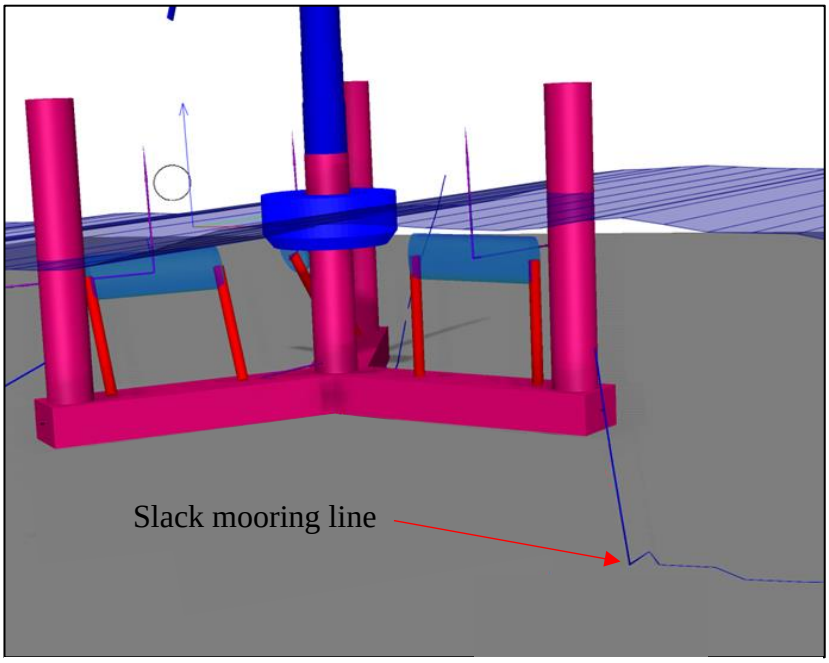

Figure 3-10 Shallow water simple catenary arrangement leeward mooring line slack.

The occurrence of slack mooring lines is a dangerous incident as during the return of the to the equilibrium position, snap loads will occur at the mooring line and fairlead. The main advantage of the catenary system is the linearity of its restoring forces' response to the floater offset. The two phenomena described above, the pulling and the slacking effects occurring at the shallow water application, constitute the simple catenary arrangement a non-viable solution.

As it has been addressed in section 1.2 a hybrid mooring design that is inspired by Xu et al. [45] concepts will be proposed. This thesis will focus only at the ULS (ultimate limit strength) and will not perform a complete mooring design check according to DNVGL-OS-E301 Position Mooring guidelines [67] that would require a fatigue limit state (FLS) and ultimate limit state (ULS) check. The current design will try to address all the issues involved with the shallow mooring water and satisfy the following criteria that have been proposed by Xu et al. [45].

- The new design parameters should use as a reference point a 200m catenary mooring arrangement. In this case, the pretension and horizontal stiffness are tuned to match the 200m mooring parameters. The line length is shorter that the 200m
- Avoiding slack condition of the leeward mooring line hence snap loads that might lead to mooring line failure.
- Each segment of the mooring line should be able to withstand the maximum load effect in every environmental condition. The maximum mooring line tension shouldn't exceed the maximum breaking strength considering the safety factor.
- The motions of the floater should be reduced to an acceptable range taking into consideration the safety of the power cables
- The mooring line shouldn't be completely lifted from the sea bottom during maximum weather conditions.

The main components of the system are presented in Figure 3-11.

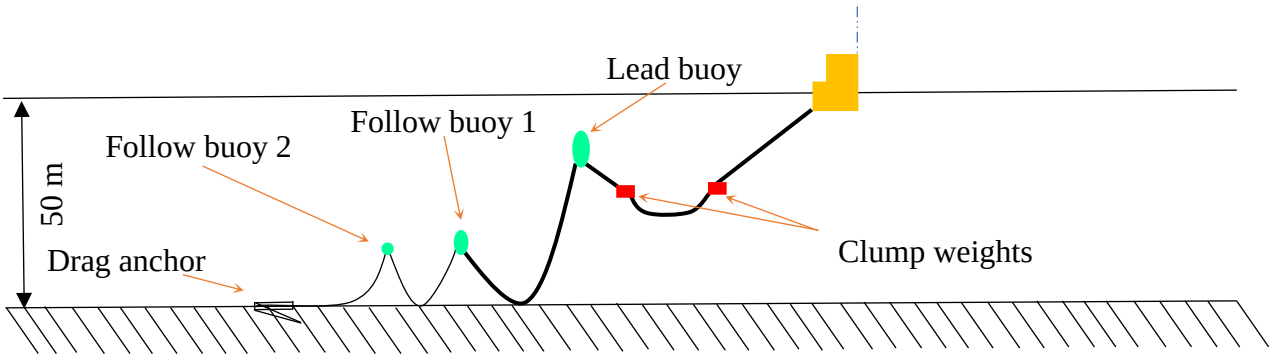

Figure 3-11 CCCB mooring components arrangement

CCCB explanation

The CCCB design is the product of the methodology presented by Xun et al. [45]. The principles that were followed by Xun et al [45] to design a feasible mooring system for the OC4 floater, were also followed in this thesis to design a mooring system for the STFC floater.

The two main objectives of this design are first to linearize the restoring forces effect and to avoid the slack of the leeward mooring line. Starting from the first objective, a large buoy is placed along the line starting from the fairlead. In the distance between them, two clump weights are placed. The clump weights increase the total weight but also straighten the mooring line close to the buoy and the floater. This results in a small equilibrium top angle from the vertical and a superior catenary shape. The line between the two clump weights has the catenary shape and induces the main restoring forces at the floater. The first big buoy in combination with the rest buoys act as a set of hinges that allows for more mooring line to be laid up among a confined space. The weight of the lines, the buoys and the length of the line ensure that the line will not lift from the bottom even during maximum weather events. The design ensures also that the leeward mooring line will not get slack first of all because the first catenary is not in touch with the seabed and second because even during the maximum offset the first catenary will not touch the sea bottom. The mooring line is not uniform throughout its length. The part that is closer to the floater and forms the first two catenaries, the hanging one and the sea bottom touching one, weigh 506kg per meter. The last catenary consists of a mooring line weighing 300kg per meter. For both cross stions, studded chain was chosen, as for the same diameter has higher weight per meter that the studdles. The philosophy of the system is to concentrate the weight in the first two catenaries thus having high stiffness response during the initial offset values and lighter mooring line at the last catenary that is going to be lifted only during extreme weather without adding though excessive tension to the mooring line.

The components used in this design are all readily available in market: The mooring lines and drag anchors are out of the shelve product from Vryhof [68]. The buoys are made by Panterplast [69], and the clump weights by Sagasubsea [70].

3.2 STFC modeling methodology

The STFC is modelled in SIMA using a fully coupled SIMO-RIFLEX model. Information about modeling have been obtained from RIFLEX user guide [71] and SIMO user guide [72]. The components are divided into rigid SIMO bodies and flexible RIFLEX slender elements. There are in total 7 rigid bodies with 6 degrees of freedom (*d.o.f)* each one in the global axis. The challenging part of the concept is the combination of rigid bodies and slender elements via couplings and flexible joints to simulate the wave energy converters. Existing features of SIMA will be used to replicate the behavior of the wave energy converters. The STFC components are presented starting from top to bottom.

The wind turbine is modelled solely in SIMA and consists of two rigid bodies with concentrated mass, the nacelle, and the hub. Both are modeled as SIMO elements including only structural mass properties. They are connected at the top of the tower and the end of the shaft respectively. All the slender structures such as the tower, the shaft, and the blades are designed as beam RIFLEX elements with distributed weight. The blades are connected through eccentric beams at the shaft end. At this end, a flexible joint is applied to allow the shaft-blades arrangement to rotate over the shaft's longitudinal axis and transfer the loads through the nacelle at the tower. The torque generation and power production are calculated via the SIMA embedded controller. We use the controller's engine data option to keep a steady power production via regulating torque. For the power generation control we use a PI controller with proportional gain kp= 0.60873 and integral gain ki=0.086962. The loads on the slender elements of the structure are calculated by RIFLEX.

The rest five rigid bodies, namely three flaps, torus and the semisubmersible are modelled as plate/shell structures using GeniE [73]. To obtain their hydrodynamic properties, we must discretize them first, by using FEM method. For our case we simulate a hydrostatic load case in GENIE for all the submerged areas and through its analysis we get the resulted mesh. The maximum mesh size for the large flat areas is 1 m and for smaller size and curved areas, we optimized the design using smaller mesh size down to 0.5 m to ensure a proper meshing quality. In Figure 3-12, the panel mesh is presented.

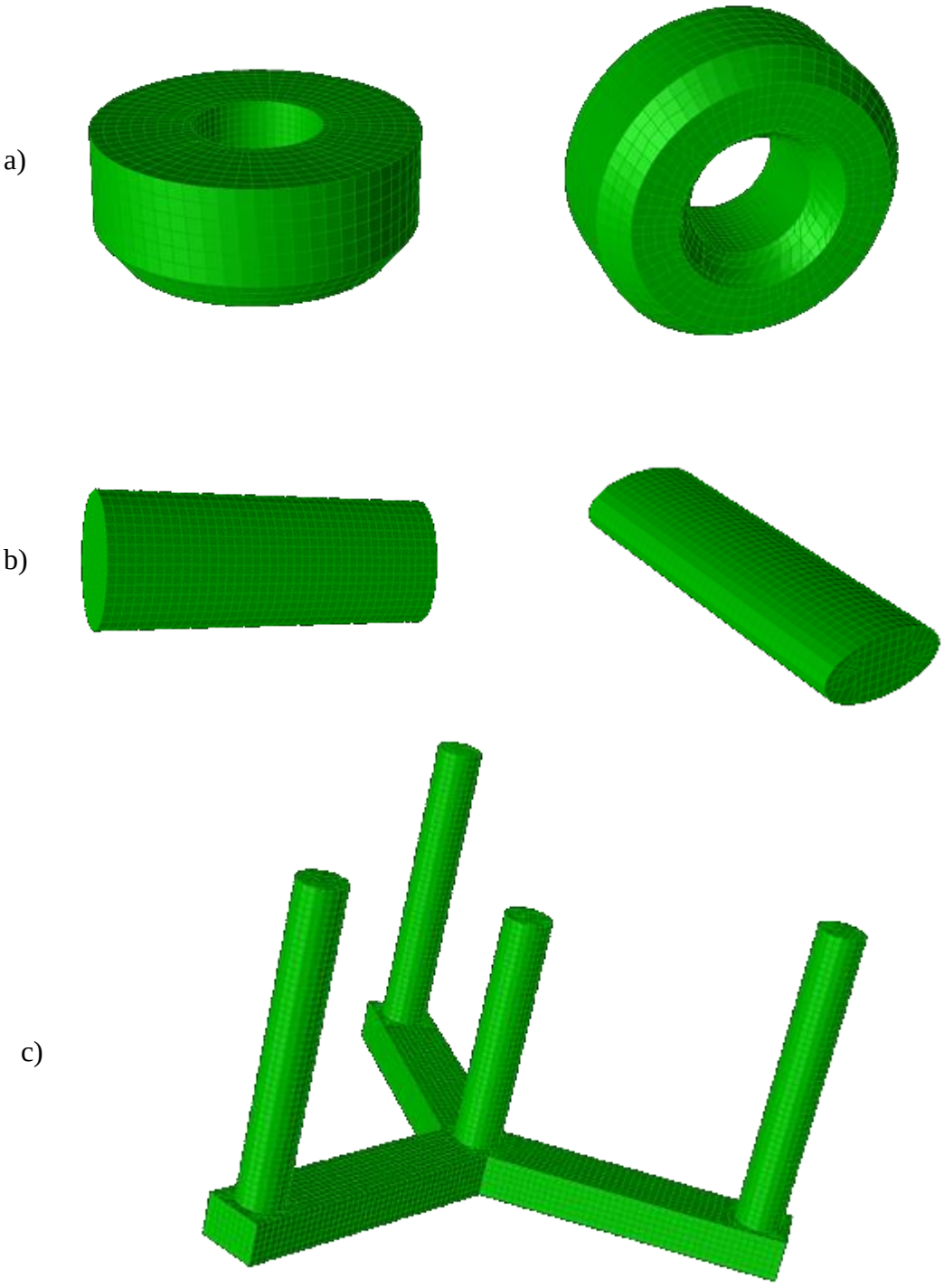

Figure 3-12 Panel mesh of all three components of STFC. a) Torus b) Flap c) CSC

A WADAM [74] analysis has been performed for all 5 submerged and floating structures in HydroD [75]. The coupling between them has been addressed as a multi body analysis. It's worth mentioning that assumptions have been made to simplify modeling. WADAM analysis is a frequency domain analysis of a body that can be either floating or submerged at a certain point according to its global axis. Nevertheless, in our case the flap is submerged at z = -2 m in its equilibrium position but during operation it can reach at z = -18 m. The added mass matrix will be significantly different when it's calculated close to z = -2 and the free surface boundary conditions compared to the one at the maximum position at z = -20 m at extreme weather conditions. To have an exact representation of the added mass in each point we should have the ability to produce a z dependent array of matrices in segments throughout a prescribed movement path. These matrices though cannot be imported into the time domain simulation as variables A and B. So, it is proposed to include the added mass matrix at the top position. This decision was made to help the model validation step based upon the observation Luan et al. [1] did that the flap's oscillation with respect to its rotational axis is relatively small. No stiffness or damping matrix is considered for the coupling of flaps and the CSC. The only interaction between the flaps and the rest of the structures is the diffraction. As regards the torus, an assumption was made for the coupling of torus and the floater. First and foremost, the torus is connected to the central column via a bearing arrangement to restrict the relative motion of torus in roll pitch yaw surge and sway. In addition, preloaded springs ensure that there is no slack movement between the torus and the floater by compressing the bearings. The effect of these springs would normally be described as stiffness and damping coupling matrices in these exact *d.o.f* they restrict. Even so, we disregard the effect of the springs and consider the two bodies as single body at these 5 *d.o.f* because the effect will be small and the calculations complexity disproportionate to the necessity for such detailed representation. The only degree of freedom where a damping matrix is applied between the torus and the floater is the heave motion where the damping value of the PTO system is used as the damping value. In Figure 3-13, a snapshot from the multibody analysis in HydroD is presented. Wadam performs a frequency domain analysis on fixed or floating structures with no speed. In the current analysis, each body is tested with frequencies ranging from 0.134 rad/s up to 5 rad/s and 0.1 interval. This translates to a range from 1.2s to 46s. These 50 frequencies will serve in the future for the second order frequency difference calculations. A range from 0 to 360 degrees is tested to ensure the full capture of the added mass and damping in a 360 radius. The seabed depth is set to z = -200m. The outcome is a text file containing the important information about the Simo body that is going to be imported to Sima.

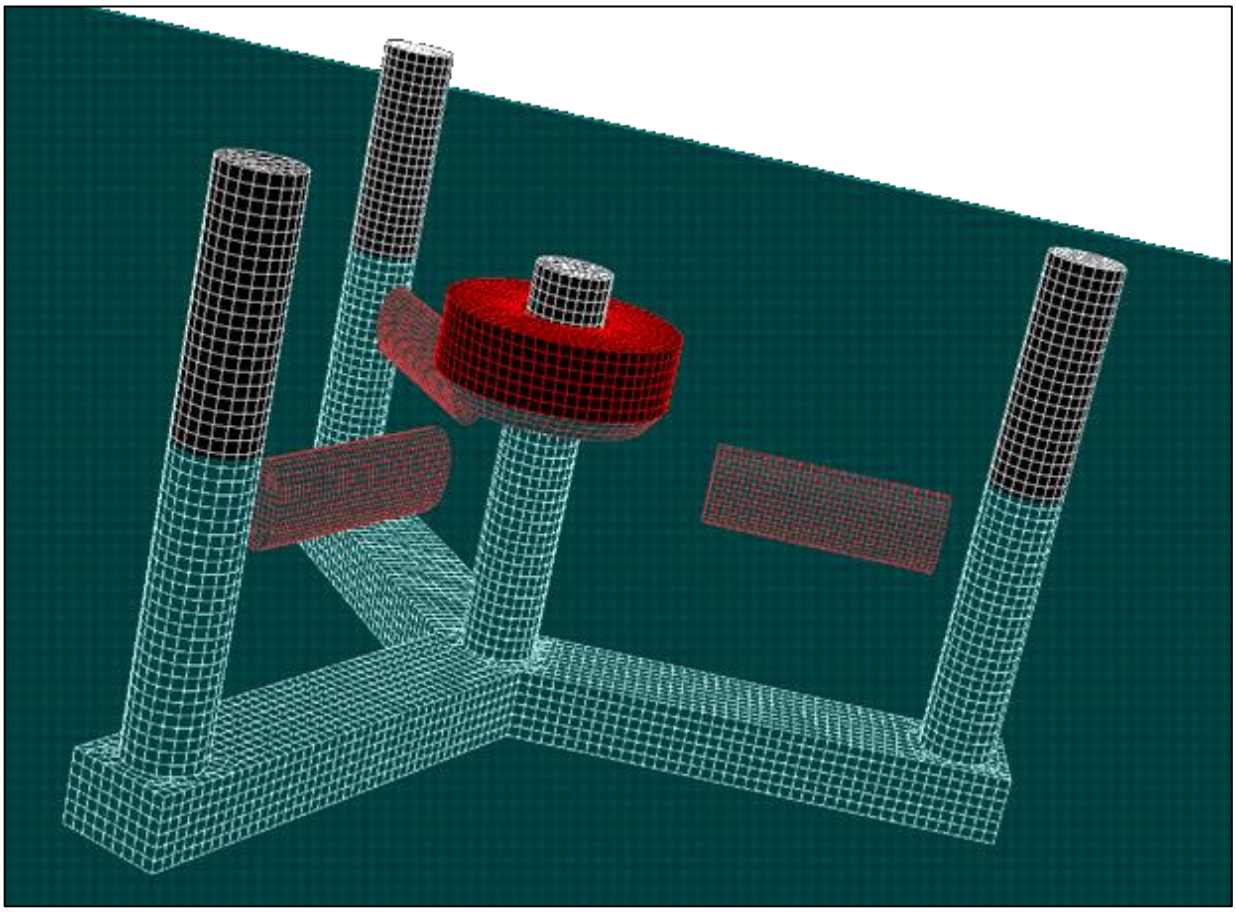

Figure 3-13 HydroD multibody analysis snapshot

The next step is the import of these objects as Simo bodies in a Riflex task created in Sima. The multibody analysis is imported to Sima as a Simo body containing the following information.

Structural mass: The mass of each object is imported to Sima and calculated from the displaced water.

Tabell 3-1 Floater mass properties

	Mass	Ixx	Iyy	Izz	CoG
Floater with ballast	9.738 e06	1.05 e07	1.05 e07	8.24 e07	-24.36m
Floater with ballast and wind turbine installed	1.0502 e07	1.0447 e10	1.0447 e10	8.1985 e09	-18.45m

Tabell 3-2 Torus and flap mass properties

	Mass	Ixx	Iyy	Izz	CoG
Torus	4.2378 e05	1.0765 e07	1.0765 e07	2.0587 e07	-0.9m
Flap	1.0 e05	3.68 e06	7.53 e06	4.17 e06	-5.5m

The imported mass of CSC is calculated by HydroD using the displaced water thus including the weight of the turbine and mooring lines. The simulation of the turbine and mooring lines using Riflex slender elements in Sima, will double their actual weight. To counter act, it and ensure the z axis heave equilibrium at z=0 an upward constant force of magnitude equal to the weight of the turbine plus the vertical downward force of the mooring lines is applied as shown in Figure 3-14.

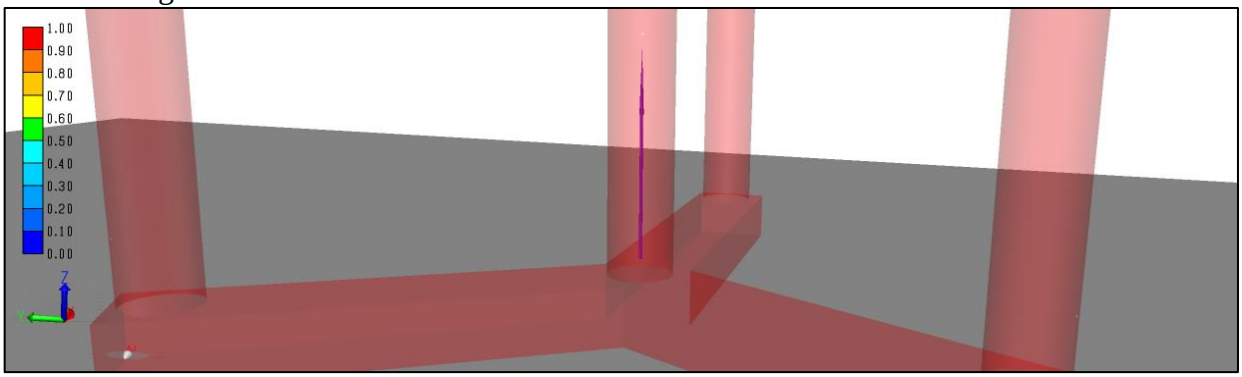

Figure 3-14 CSC upward force

The force is applied at the center of gravity -18.45m with upward direction at the global axis insuring that during rolling and pitching it still faces upwards.

Hydrostatic stiffness:

The restoring force in the heave negative direction is the buoyancy. The linear stiffness of the Simo body is a 6 by 6 matrix with only three non-zero values. These values are the stiffness in heave direction C_{33}, and the stiffness in roll and pitch, C_{44} and C_{55} respectively. Special attention should be paid to C_{44} and C_{55} regarding to whether the Wadam analysis was performed using the standalone CSC CoG -24.36 or the total CSC with installed turbine CoG -18.45. In case the Wadam analysis is performed with the latter, the GM will be calculated taking into consideration the added weight of the turbine thus smaller GM value. The addition of slender elements in Sima will further reduce the GM resulting in larger pitch and roll angles. To counter act that either the HydroD calculations should be performed with the CSC standalone CoG, or the below formula should be used to correct C44 and C55 value at Sima.

$$C_{55,44} = \rho g I_{wp} + \rho g \nabla z_B - M g z_G \quad (23)$$

No corrections are needed at the Torus stiffness values imported from HydroD. In its case also, only C_{33}, C_{44}, and C_{55} terms are present at the stiffness matrix. Since the flaps are submerged, the hydrostatic stiffness matrix imported from HydroD has no physical meaning. It should be disregarded and replaced by a constant stiffness regardless of position. The flaps weigh 100 tons and displace 394 tons of water. This results to a constant upward buoyancy force of 2884 kN. To obtain zero force equilibrium at the z axis, each flap arm, exerts half of the buoyancy force thus resulting in the flap being in equilibrium. To simulate buoyancy, we apply a specified force with magnitude of 2844 kN and a positive vector to the global z axis. To ensure that the buoyancy will be facing constantly upwards the force should be applied to the global and not on the local body axis. The force must be applied at the center of buoyancy of each flap as shown in Figure3-15

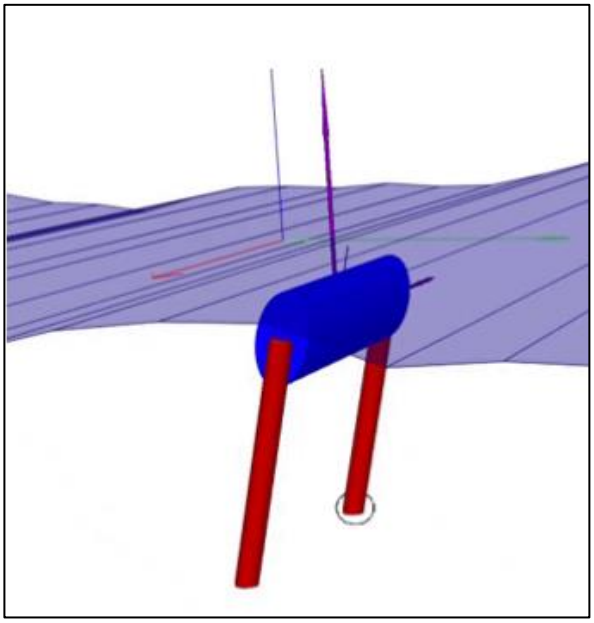

Figure 3-15 Flap upward force

A hydrodynamic effect that is not included in the Wadam analysis is the quadratic drag forces. To calculate them, slender elements representing the pontoons and columns are tied to the CSC Simo body using the Morison equation. A slender element accounting also for the drag forces of the submerged part of the Torus is tied to the Torus Simo body. The slender elements are presented in Figure 3-16 and their properties in Table 3-3.

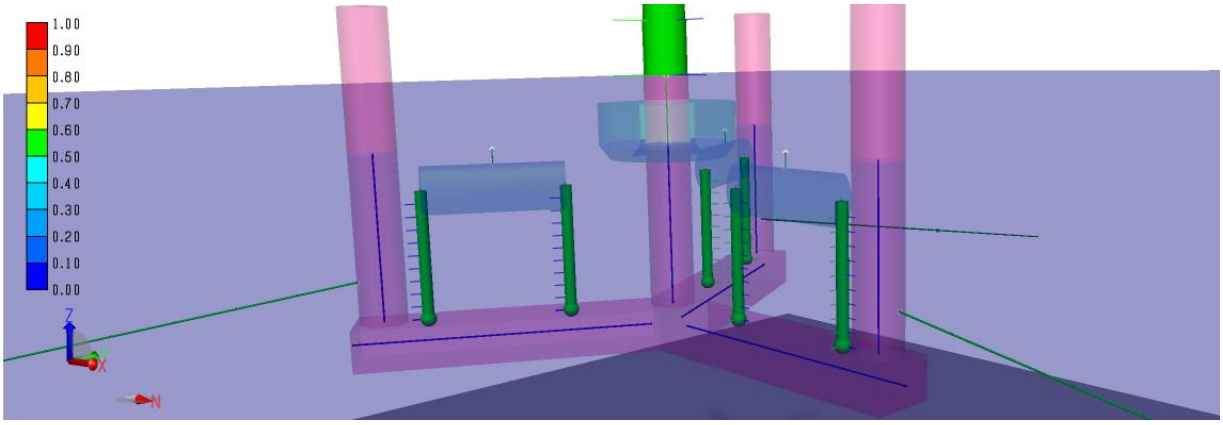

Figure 3-16 Sima snapshot of the slender elements tied up to the CSC Simo body

Table 3-3 Quadratic drag force coefficient calculation parameters

Slender el.	X1 (m)	Y1 (m)	Z1 (m)	X2 (m)	Y2 (m)	Z2 (m)	C_D (-)	C2y/C2z (Ns^2/m^3)
Pontoon 1	3.25	0	-27	45.5	0	-27	1.9	5228/9686
Pontoon 2	-1.625	2.815	-27	-22.75	39.4	-27	1.9	5228/9686
Pontoon 3	-1.625	-2.815	-27	-22.75	-39.4	-27	1.9	5228/9686
Column 1	41	0	0	41	0	-24	0.6	1666/1666
Column 2	-20.5	35.5	0	-20.5	35.5	-24	0.6	1666/1666
Column 3	-20.5	-35.5	0	-20.5	-35.5	-24	0.6	1666/1666
Central Col	0	0	0	0	0	-24	0.6	1666/1666
Torus	0	0	0	0	0	-2	0.6	10250/10250

The added flaps will increase the buoyancy of the total construction. In order to counter act their uplifting effect and maintain the equilibrium position at z = 0, the peripheral columns

should be ballasted. To replicate this effect in Sima, we could either install a downward force with equal magnitude as the buoyancy force but given the fact that it would be applied only at the center point of the pontoon, the mass moment of inertia effect would be neglected. To ensure that the full effect of the added ballast to the side columns is captured, three more slender elements are attached to the columns with the following properties presented in Table 3-4.

Table 3-4 Ballast addition

Slender el.	X1 (m)	Y1 (m)	Z1 (m)	X2 (m)	Y2 (m)	Z2 (m)	Distr. Mass (kg/m)
Column 1 Ball	41.0	0	-7.86	41.0	0	-16.3	34004
Column 2 Ball	-20.5	35.5	-7.86	-20.5	35.5	-16.3	34004
Column 3 Ball	-20.5	-35.5	-7.86	-20.5	-35.5	-16.3	34004

First order motion / wave force transfer function:

The calculated motion RAO, for every direction and d.o.f defined in HydroD, is inserted to Sima as 36 sets of period-amplitude tables. A total of 216 predefined tables constitute the transfer function of each Simo body. The same number of sets are also inserted for the first order force function of each Simo body.

Retardation function:

The free surface memory effects that are part of the wave radiation forces are calculated in HydroD using a time convolution of the retardation function. When transforming the equation of motion from frequency into time domain, this “memory function” or impulse response function is introduced into the equation of motion and accounts for the frequency dependent added mass and linear damping during the non-linear effects of penetrating the free surface.

Added mass infinite frequency:

A 6 by 6 matrix of added mass in infinite frequency is inserted from Hydro. No changes are made.

Connection of Torus and Central column.

The challenge at this point is the simulation of the bearing system and the end stop system. The torus has an effective stroke length of 6 meters from z = -3 to z = +3. This characteristic derives from the length of the hydraulic pistons. Overextension or compression of the pistons at the minimum stroke length should be avoided; thus, an end stop spring arrangement that restricts the stroke within the pistons' permissible limits should be used. There are in total three components regarding the sliding mechanism of torus that should be modeled, namely the bearing system, the end springs, and the hydraulic pistons. The design of sliding mechanisms follows Wen et al. [76].

End springs are going to be simulated as point fenders. Simo modelling enables the restriction of two bodies relative motion by utilizing point or roll fenders and bumpers. In this case, two point fenders in different elevations are used to achieve the desired heave restriction. Each fender point arrangement consists of a fender point and a fender plane attached to the torus and the floater's central column respectively. Both restrictors share the same elevation for the fender point z = 9 m and differ in the fender plane elevation with z = 6 and z = 12 for the downward restriction spring and the upward restriction spring respectively. A schematic representation of the end stoppers system is shown in Figure 3-17, the spring linear stiffness and damping values are shown in Table 3-5 and presented by Muliawan et al. [41, 61].

Apart from heave restriction, a constrain in all other degrees of freedom should be applied. The sliding bearing ensures that the torus is heaving concentrically according to the floater's central column. To achieve that, a total of three docking cone couplings are applied in different elevations presented in Table 3-6. The docking pins are positioned on the floater and the docking cones are positioned on the torus. All three of docking cones share the same cone elevation which represents the bearing constrain on the torus, and in addition to this, the central column is represented by three pins in different elevations. Zero friction in the heave direction is assumed. A detailed view is shown in Figure 3-18, the propertied of the cones are shown in Tables 3-7 and were presented by Muliawan et al. [41, 61].

Table 3-5 End stopper properties

Points	Distance	Stiffness	Damping
1	0	0	0
2	-0.0001	1 e06	1 e04

a)

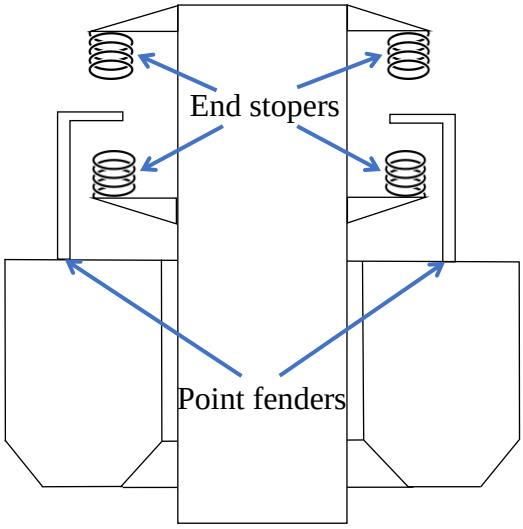

b)

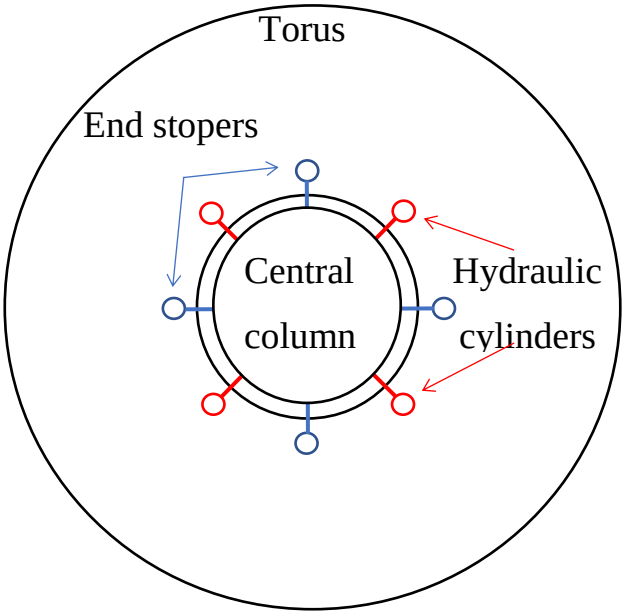

Figure 3-17 a) End stoppers schematic side view b) End stoppers schematic top view

The current arrangement does not restrict the yaw rotation of the Torus. To ensure that the torus will not start spinning, a C_{66} stiffness 20% larger than the C_{44} is inserted in the hydrostatic stiffness matrix of Torus. This stiffness has no physical meaning as the physical architecture of torus requires very small tolerances in the yaw rotation because this motion is perpendicular to the hydraulic cylinders of the PTO thus the actual bearing system will restrict also the yaw rotation.

Table 3-6 Docking cone coordinates

	Pin elevation	Cone elevation
Docking Cone 1	5.8	12
Docking Cone 2	2.8	12
Docking Cone 3	-5.8	12

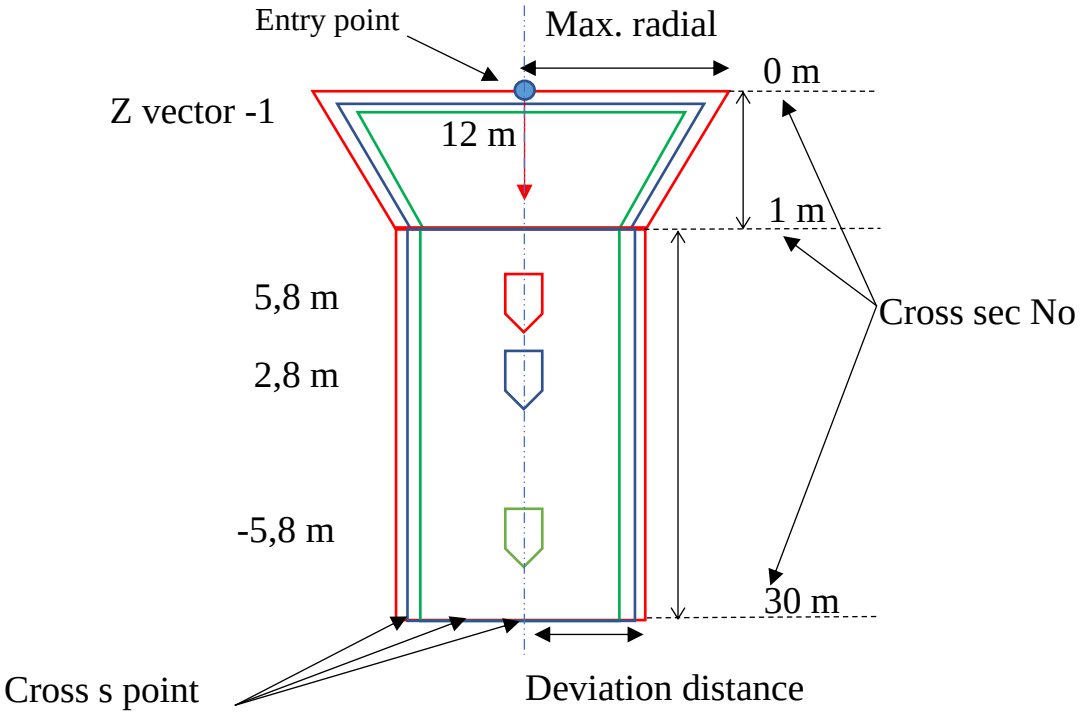

Figure 3-18 Cross stion schematic view of the docking cones arrangement

Table 3-7 Docking cone properties

Cross section No.	Cross sec. dist. From end		Max. rad. dist
1 (entry point)	0m		0.01
2	1m		-
3	30m		-
Cross stion distance-force properties			
Cross s. point	Distance	Vert. Force	Damping
1	0	0	0
2	0.001	1 e07	0
3	5	1 e07	0

Furthermore, the PTO system is simulated using a set of fixed elongation couplings. To replicate the effect of the hydraulic cylinders at the relative motion of torus with respect to the floater, the values of stiffness and damping of the PTO system are used. So far, these values have affected the added mass and damping matrices of both bodies in the frequency domain simulation and now they will affect the torus-floater elevation realizations in the time domain simulation. One fix elongation coupling is applied between two fixed points on torus and floater respectively with constant damping value 8.0e06 Ns/m. To simulate the stiffness of the PTO, another fixed elongation with linear stiffness of 50000N at 5m elongation is applied. The values are presented in Table 3-8 and borrowed by Muliawan et al. [41, 61]

Table 3-8 Fixed elongation coupling properties

Point number	Distance	Stiffness	Damping
1	0	0	8 e06
2	5	5 e04	8 e06

Connection of flaps and pontoons

The coupling of the flaps with the floater takes place through slender RIFLEX elements, the arms. Their properties follow Luan et al. [35]. To achieve the proper rotation of the flap, the following properties illustrated in Figure 3-19 should be applied. The connection of the flap body is achieved with an artificial line between the node "d", that can have any arbitrary point in the rigid body geometry, and the beginning of the flap's local axis that coincides with the axis origin imported from WADAM, node "e". Total length of the arms is 18,5 m. They are clamped at the flap with two nodes at the center of the elliptical cross section at two ends. Nodes "c" and "f" should be slave to node "e" so that the flap doesn't rotate over its z axis during operation. The connection with the pontoons takes place at nodes "a" and "h" that are slave to the beginning of axis of the floater. To obtain rotation of the flap, a flexible joint should be applied to the lower end of each arm. As mentioned also by Luan et al. [35], the flexible joint cannot be applied at a slave node, thus the arms are divided in two equal cross section pieces, namely "a-b", "b-c" for the first arm and "h-g", "g-f" for the second arm, with length 0,1 m and 18,4 m respectively. The flexible joint is applied at end one of the second line segment. Properties of flexible joint are presented in Table 3-9. To achieve the right orientation of rotation for flaps two and three, local element axis should be applied for all the segments of the arm lines.

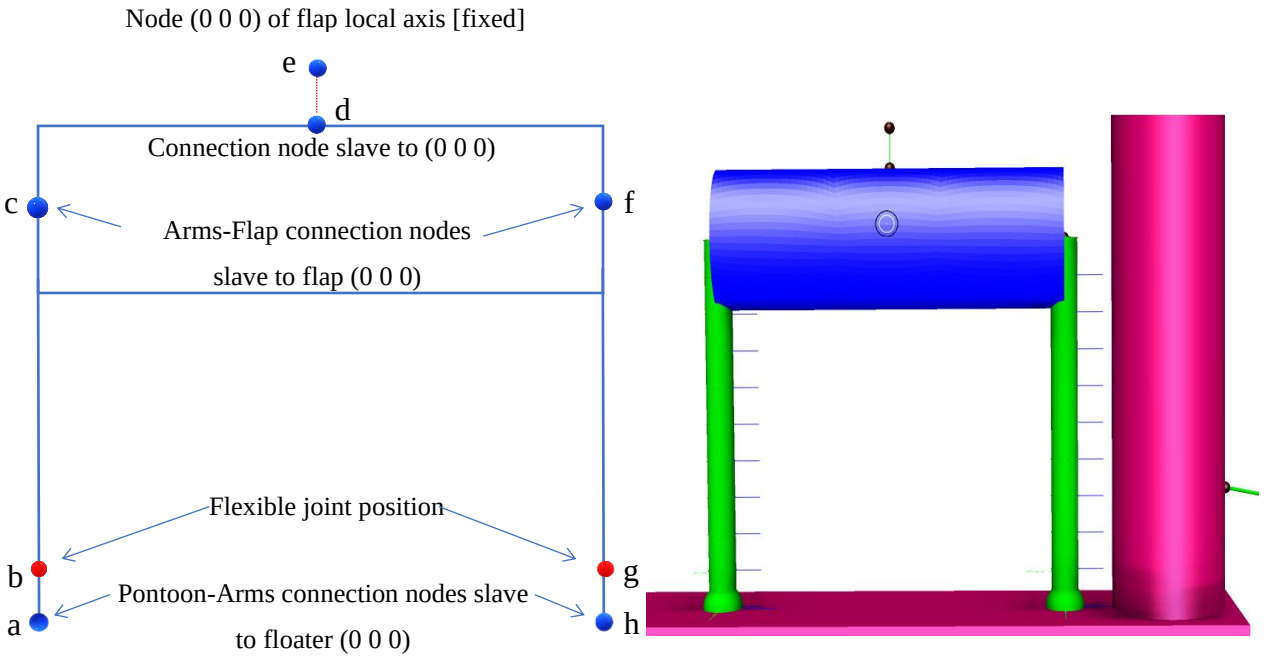

Figure 3-19 Flap super nodes / Riflex elements arrangement.

Table 3-9 Flap joint properties

Local axis	Stiffens rotations	Damping rotation [Nms/deg]	Linear stiffness magnitude [Nm/deg]
x (Line longitudinal)	Linear	0	1 e05
y	Linear	0	1 e05
z	Free	1.2 e05	-

Mooring line arrangement.

A catenary mooring arrangement proposed by Luan et al. [35] is modelled. The mooring arrangement is a combination of chain and clump weight fixed at drag anchors. For the purposes of modelling, a simplified equivalent model with cylindrical cross section and a clamp weight is used. Modeling values are presented in Table 3-10

Table 3-10 Mooring line characteristics

Mass per unit length (in the air)	115 kg/m
Diameter of the mooring line cross-stion	0.137 m
Clump weight in water	15,000 kg
Clump distance from fairlead across mooring line	240 m
Material density	7850 kg/m^3
Mooring line unstretched length	1073m
Fairlead pretension	1.638 KN

Environmental conditions

The following methodology follows the methodology of Cheng et al. [77]. The turbulent wind fields are generated using software TurbSim [78]. The Kaimal turbulence model is defined in IEC 61400-1 Class C [79]. The wind shear profile is considered by applying the power law shown in equation

$$u_{10}(u_{ref}) = u_{ref} \times \left(\frac{z_{10}}{z_{ref}}\right)^{\gamma} \tag{24}$$

Uref	Reference wind speed
z_{ref}	Hub heigh=90m
z	Height
γ	Power law exponent=0.14

For the description of the irregular wave state, the JONSWAP spectrum with significant wave height Hs and peak period Tp is used. Using data from the Statfjord site in the Northern North Sea, several loading scenarios have been generated. Based on observations from 1973 to 1999, a joint distribution for wind and wave proposed by Johannessen et al. [80] has been adopted for describing the sea state in this area.

$$f_{U_{10}H_sT_p}(u_{10}, h_s, t_p) = f_{U_{10}}(u_{10}) * f_{H_S|U10}(h_s|u_{10}) * f_{T_p|H_sU_{10}}(t_p|h_s, u_{10}) \tag{25}$$

The joint distribution is the result of a marginal distribution for wind, a conditional distribution of Hs for given U10, and a conditional distribution of Tp for given U10 and Hs. U10 is the 1-hour average wind speed at a height of 10m. Using the law stated in Stion 4.4, the equivalent

U10 can be determined using the wind speed Uw at a reference height of 90m. Given the U10, a 2-parameter Weibull distribution is used to characterize the conditional distribution of significant wave height Hs. The following formula gives the expected wave height. The shape and scale parameters α and β respectively are given.

$$E(H_S) = \beta\Gamma\left(\frac{1}{\alpha} + 1\right) \tag{26}$$

$$\alpha = 2 + 0.135 \times u_{10} \tag{27}$$

$$\beta = 1.8 + 0.1 \times {u_{10}}^{1.322} \tag{28}$$

Knowing the U_{10} and Hs, the following formula will give the spectral peak period T_p.

$$E(T_P) = (4.883 + 2.68 \times {h_s}^{0.529}) \times \left[1 - 0.19 \times \frac{u_{10} - \left(1.764 + 3.426 \times {h_s}^{0.78}\right)}{1.764 + 3.426 \times {h_s}^{0.78}}\right] \tag{29}$$

For the mean power production and global analysis, 6 sets of independent 4000s simulations with random seeds are performed for each load case. The mean values are derived from the time series data. The first 400s are eliminated to reduce the transient effects. The load cases are presented in Table 3-11

Table 3-11 Mean power production load cases

Load case	U_w (m/s)	Turb.Int	H_s (m)	T_p (s)
EC1	5	0.224	2.10	9.74
EC2	10	0.157	2.88	9.98
EC3	14	0.138	3.62	10.29
EC4	18	0.127	4.44	10.66
EC5	22	0.121	5.32	11.06
EC6	25	0.117	6.02	11.38

For the annual power production and global analysis, 11 sets of independent 4000s simulations with random seeds are performed for each load case. The mean values are derived from the time series data. The first 400s are eliminated to reduce the transient effects. The load cases are presented in Table 3-12.

Table 3-12 Annual power production load cases

Load case	U_w (m/s)	Turb.Int	H_s (m)	T_p (s)
EC 1	5	0.224	2.10	9.74
EC 1.5	7.5	0.180	2.45	9.82
EC 2	10	0.157	2.88	9.98
EC 2.5	12	0.146	3.2	10.1
EC 3	14	0.138	3.62	10.29
EC 3.5	16	0.132	3.96	10.44
EC 4	18	0.127	4.44	10.66
EC 4.5	20	0.124	4.8	10.82
EC 5	22	0.121	5.32	11.06
EC 5.5	23.5	0.119	5.58	11.18
EC6	25	0.117	6.02	11.38

3.3 CCCB Clump-Chain-Clump-Buoy modeling methodology

Line properties

The modeling methodology of the new mooring system is mainly the same with a simple catenary shape mooring. The following properties at Tables 3-13, 3-14, and 3-15 are used for the line modeling in Sima.

Table 3-13 Anchors coordinates

Anchor	Xg	Yg	Zg
1	974.5	0	-50
2	-487.25	843.94	-50
3	-487.25	-843.94	-50

Table 3-14 Nodal components

Nodal component	Weight (kg)	Volume (m^3)	Position along the line (m)
Clump1	28.000	3.56	51.2
Clump2	28.000	3.56	131
Lead Buoy	14000	95	140
Follow Buoy 1	4000	46	320
Follow Buoy 2	4000	42	480

Table 3-15 Cross section properties

Total line length	935m
Cross section 1 weight in water	300kg/m
Cross section 2 weight in water	500kg/m

Hydrodynamic properties

While moving closer to shallow water, the effect of the seabed to the hydrodynamic properties of the structure is accounted for by performing a new WADAM analysis with seabed position at z = -50m.

Environmental conditions

Almost the same methodology as chapter 3.1.2 is used to generate the load cases for testing the new mooring line design. The only difference is that and the maximum values were derived from

the time series data instead of the minimums, to reflect the stochastic variations. At the last load case, a 1m/s current is introduced. A surface current speed of 10m/s is considered a 10-year return period incident and is recommended by the DNVGL [67] for mooring analysis. The current profile is considered linear from maximum speed at still water till zero speed at z = -50m. The following formula describes the profile. The cases are presented in Table 3-16.

$$U_c(z) = 1.0 * \left(\frac{50 + z}{50}\right) \ for \ -50 \leq z \leq 0 \tag{30}$$

Table 3-16 Load cases for mooring analysis

Load case	U_w (m/s)	Turb.Int	H_s (m)	T_p (s)	U_c (m/s)
EC 1	8	0.174	2.53	9.85	-
EC 2	16	0.132	3.97	10.44	-
EC3	24	0.118	5.69	11.23	-
EC4	40	0.110	9.77	12.95	-
EC5	40	0.110	9.77	12.95	1.0

4 RESULTS AND DISCUSSION FOR THE STFC CONCEPT

The results presented in this chapter are extracted from C.F Lee, C. Tryfonidis, M.C Ong [81]

4.1 Decay test

Decay simulations are carried out for all three different concepts: the original (1) CSC model proposed by Luan et al. [31], the SFC (2) model being a CSC equipped with three flap type WECs proposed by Luan et al. [35] and the STFC (3) model which is a CSC equipped with three flap type WECs and a torus WEC proposed by Lee et al. [81]. The WECs' natural periods are also calculated.

4.1.1 Decay test Environmental and operational conditions

During decay test, the wind turbine is put in parked mode and the WECs are put in operational condition to capture the effect of the PTO damping properties to the overall structure behavior. Even though the main reason behind the decay tests is to describe the effects of the added WECs to the structure.

4.1.2 Decay results

Table 4-1 Natural period results

DOF	CSC (s)	SFC (s)	Damping (%)	STFC (s)	Damping (%)
Platform surge	84.9	85.15	5.7	86.62	6.5
Platform heave	25.1	26.91	2.5	27.67	19.0
Platform pitch	31.4	34.68	2.6	32.63	2.4
Platform yaw	58.12	63.14	-	63.7	10
Flap2 rotation	-	14.50	7.3	14.16	6.5
Torus heave	-	-	-	19.4	23.3

In table 4-1 the natural period results are recorded. Comparing the STFC with CSC, a slight only increase in natural period is observed at surge, heave, pitch, yaw DOF. Surge increased 2%, heave 10%, pitch 4%, and yaw 9.6%. The increase in natural period was caused by the increased inertia due to the installed WECs and ballast addition. Comparing the SFC and STFC, a slight decrease of 5.9% is noted at pitch natural period. The torus installed in the middle column acts as a single body in the pitch DOF, at least in the numerical model. The increased hydrostatic stiffness induces higher restoring forces thus the decreased period. In reality, there is a damping and stiffness matrix value in coupling η_{44} and η_{55} as the torus bearing surface contacts are spring preloaded to avoid impact loads between torus and floater. As a result, the experimental data is expected to indicate a smaller decrease in periods. Continuing with the torus and floater heave motions, the steady increase in natural period along the CSC, SFC and STFC model indicates that the effect of the PTO system is negligible. Prompted by the pitch motion results and assume that the torus is locked at z=0, a significant increase in hydrostatic stiffness and reduced natural periods are expected. The yaw natural period increases of 8% among CSC and STFC can be attributed to the increased mass moment of inertia.

4.2 Regular wave tests

A series of regular wave tests are carried out on the numerical models of SFC, STFC and WECs separately, to evaluate their response amplitude operator (RAO). The wind turbine and WECs are in operation mode during the tests. Twelve different period waves with 1m amplitude are used. The test frequencies are presented in Table 4-2.

Table 4-2 Regular wave periods

	Period		Period
T1	5.013s	T7	11.830s
T2	6.965s	T8	12.806s
T3	7.934s	T9	13.782s
T4	8.910s	T10	14.757s
T5	9.885s	T11	15.726s
T6	10.861s	T12	17.678s

In order to ensure the validity of the numerical modeling, the SFC model results are compared with the experimental data published by Michailides et al. [82]. In Figures 4-1, 4-2, 4-3,4-4 and 4-5 the RAOs of the SFC agree well with the experimental responses. Before the discussion takes place, few important values that will play crucial role are presented in Table 4-3

Table 4-3 Torus and Flap natural periods

Torus heave natural period	Flap rotation period
19.4 s	14.5 s

Flaps influence on the structure:

In Figure 4-1, the influence of flaps 2 and 3 rotation to the platform surge motion is observed. A slope building up from 8 s reaches its peak at 14.5 s and after that the slope becomes a lot milder. The peak is more obvious in the numerical data of SFC and STFC. This can be attributed to the difference in the PTO damping between the experimental and the numerical model.

In Figure 4-5, the influence of flaps 2 and 3 to the pitch motion of the platform can be observed. The numerical data from SFC and STFC experience a peak at 14.5 s. The slope though is much shorter in this occasion and exactly after the peak the slope becomes negative. This can be attributed to the fact that flaps 2 and 3 are rotated 30deg and -30deg on the xy plane from the pitch platform axis, thus it quickly dies out. In this case also the experimental data don't follow the numerical model due to the difference in PTO damping.

Torus influence on the structure**:**

In Figures 4-3 the influence of torus on the floater its observed. The STFC RAO experiences a peak close to the natural period of torus in contrast with SFC, whose both numerical and experimental data don't.

Power absorption:

Flap number 2 is selected as reference for all flaps. In Figure 4-6, a peak at the absorbed power is observed close to the natural period. The magnitude and position of the peak differ between the numerical and experimental data because of the different PTO damping.

To interpret the power production of torus, a combined interpretation of Figure 4-6 and 4-4 should be made. Absorbed power of torus doesn't depend primarily on the torus RAO but on the torus-floater relative heave motion RAO. The absorbed power significantly outperforms the flaps

as it is obvious but there is not a peak in power close to the torus natural period. The same pattern of a plateau with two slopes on each side, at the same frequencies, is observed in both Figures 4-4 and 4-6. To the point that the torus' RAO reaches its maximum point, the influence of the floater RAO sort of cancels out the first and the relative torus-platform RAO decreases. This broad range of frequencies that the torus is excited is also the reason that the power absorbed is much higher than the flaps which in turn experience only a peak close to their natural period instead of a wider plateau across a range of periods. This also indicates the superiority of two-point absorbers over the surge action flaps. It's worth noting that the flaps were originally designed to be fixed on the bottom of shallow water thus taking advantage of the surge oscillating action of waves reaching the bottom in the form of short vertical axis elliptical orbits. Further comments and proposals will follow in the future work section.

Torus and flaps interaction:

No correlation between RAO of torus and flaps is observed.

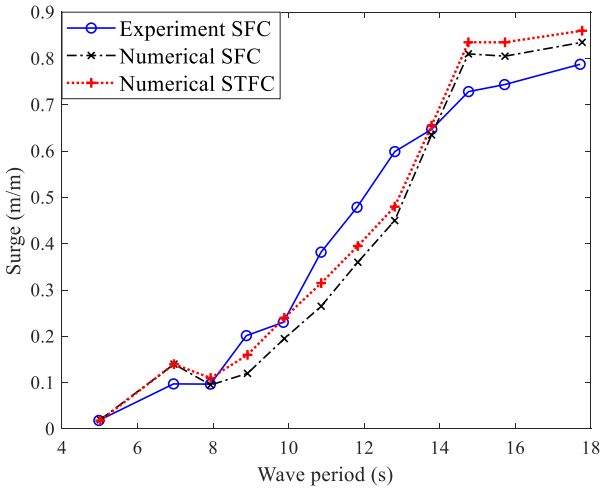

Figure 4-1 Floater surge RAO

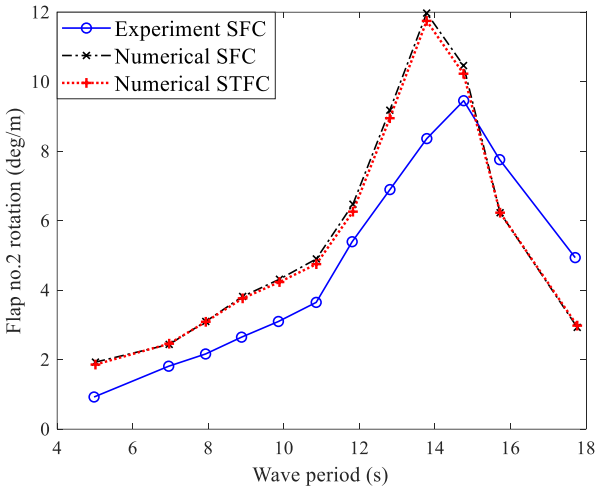

Figure 4-2 No2. Flap rotation RAO

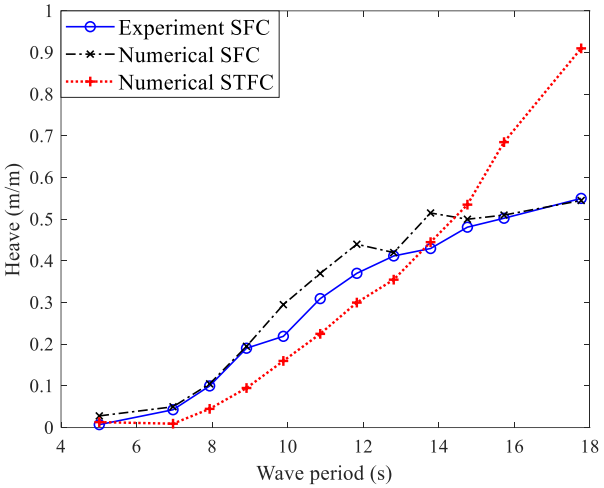

Figure 4-3 Floater heave RAO

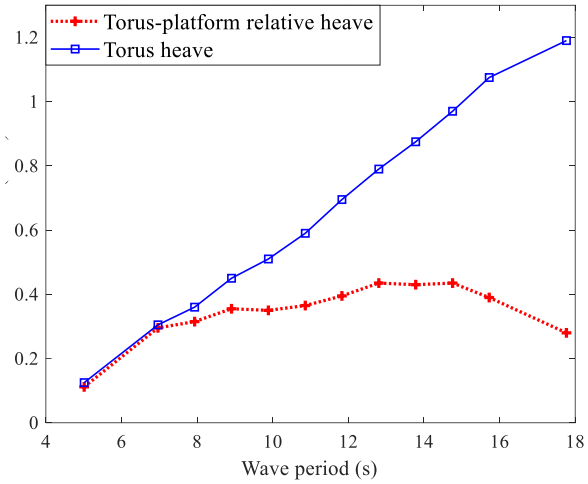

Figure 4-4 Torus heave RAO

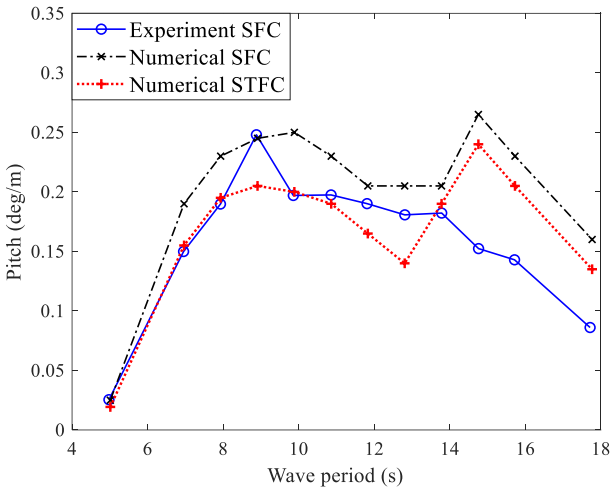

Figure 4-5 Floater pitch RAO

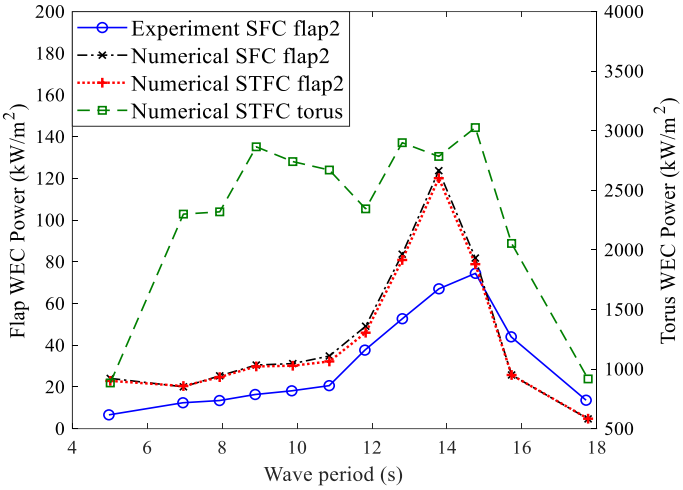

Figure 4-6 Absorbed power RAO

4.3 Irregular waves and turbulent wind tests

Surge motion:

The dynamic behavior of the structure is simulated under the environmental conditions presented in numerical modeling. Starting from Figure 4-7, the almost identical mean surge responses for both CSC and STFC are observed. Surge motion is affected by the mean wind thrust and the mean mooring restoring forces. Prompted by the largest deviation among the ECs, a power spectral density for the heave motion in EC3 is plotted. A significant drop in pitch resonant response is noted for the STFC in comparison with the CSC in Figure 4-8. The torus addition resulted in a stiffer structure in the pitch DOF, decreasing the effect of pitch surge coupling F_{r14} and C_{14} thus the surge realizations do not deviate far from the mean value. Coupling between F_{r14} and C_{14} are present due to the difference in submerged and emerged volume during pitching motion.

Heave motion:

In Figure 1 The mean heave values for CSC and STFC are close to zero, However, the standard deviation in heave motion is smaller for the STFC due to the lower heave response closer to the platform heave natural frequency as shown in Figure 4-12. The addition WECs, pushed the floater heave resonance frequency further away from the EC3 wave frequency.

Pitch motion:

In Figure 4-9, the STFC experiences lower mean pitch motions for all ECs. Std follows the same pattern except EC5 and EC6 where the std is almost the same. EC3 shows the largest difference in std due to a reduction in response at the pitch natural period frequency as is presented in Figure 4-10. The same difference magnitude can be noted in Figure 4-8 also where the pitch resonant response for the STFC is significantly reduced in comparison with CSC.

Overall motions comparison:

The overall impression from the global analysis is that the addition of WECs doesn't significantly affect the behavior of the structure during operational conditions. From the platform motions comparison between CSC and STFC, there are no strong indications that the mooring arrangement should be reconsidered.

WECs influence on the wind production:

The comparison of wind power production of CSC and STFC in Figure 4-17 indicates that the addition of WECs doesn't significantly affect the power performance of the turbine. Even though the mean values are the same across the ECs, the standard deviation for the STFC is smaller for EC3. The same pattern can be noted also in Figure 4-13 and 4-15 where the standard deviation for both Aerodynamic thrust and Aerodynamic torque in EC3 is reduced in comparison with CSC. The reduced wind thrust fluctuation leads to smaller pitch motion thus higher wind consistency. Even though it's a quite small effect, we could say that the reduced standard deviation in EC3 leads to a slightly better wind quality.

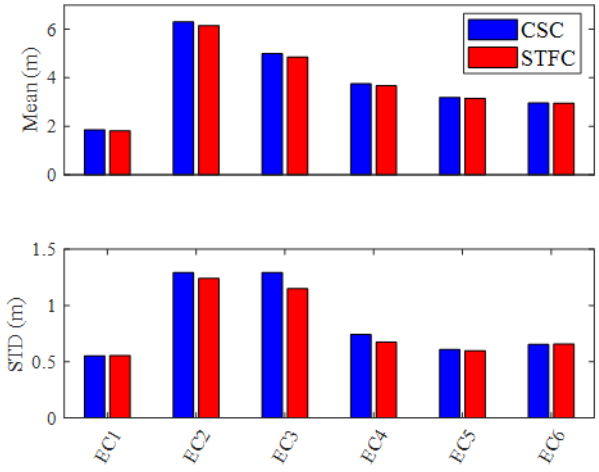

Figure 4-7 Floater surge motion

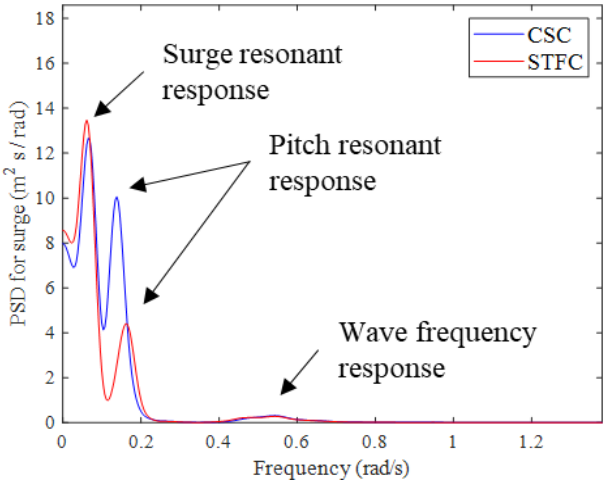

Figure 4-8 Floater surge power spectra

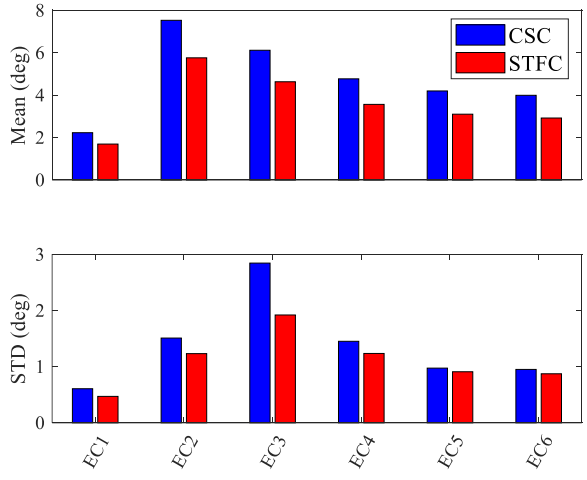

Figure 4-9 Floater pitch motion

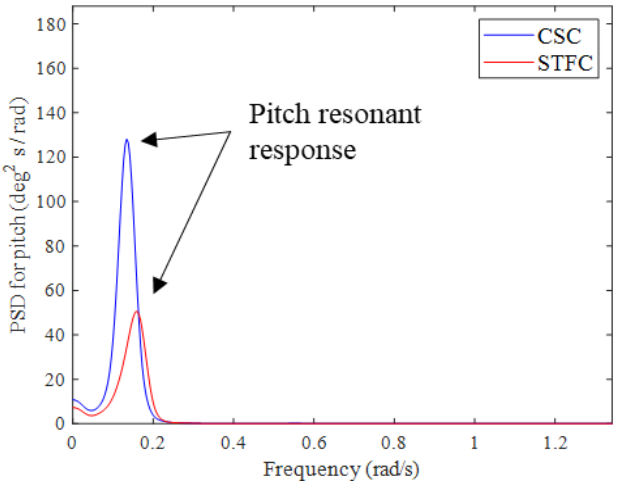

Figure 4-10 Floater pitch power spectra in EC3

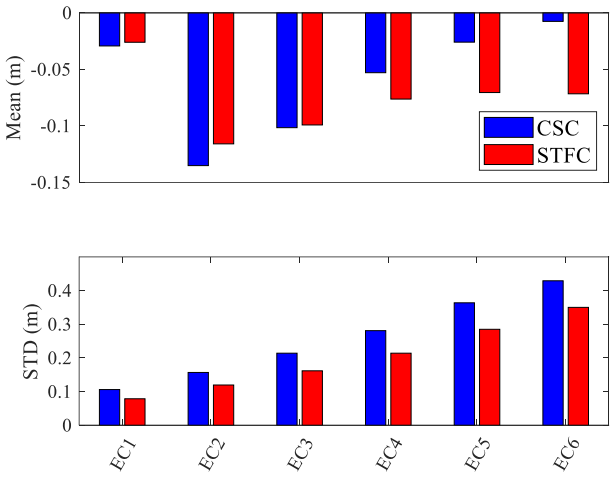

Figure 4-11 Floater heave motion

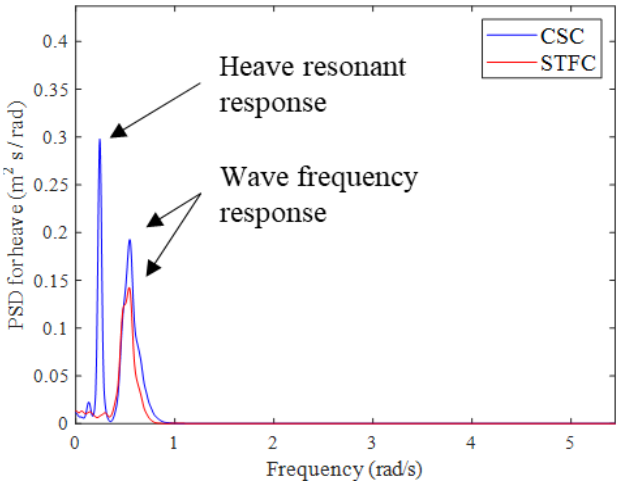

Figure 4-12 Floater heave power spectra

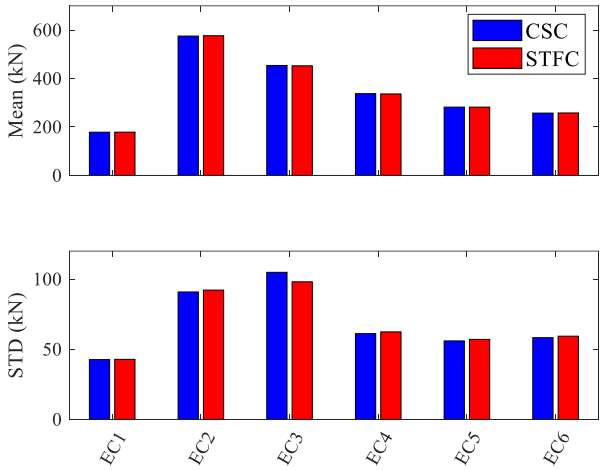

Figure 4-13 Aerodynamic thrust

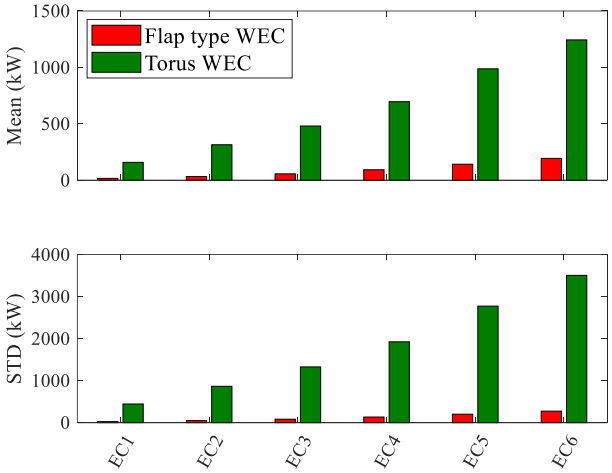

Figure 4-14 WEC absorbed power

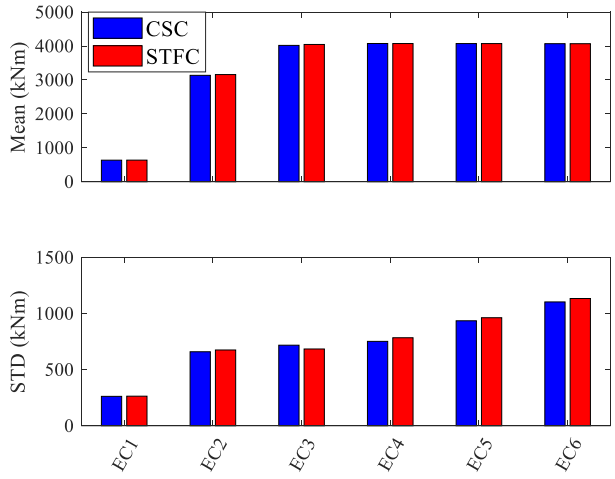

Figure 4-16 Aerodynamic torque

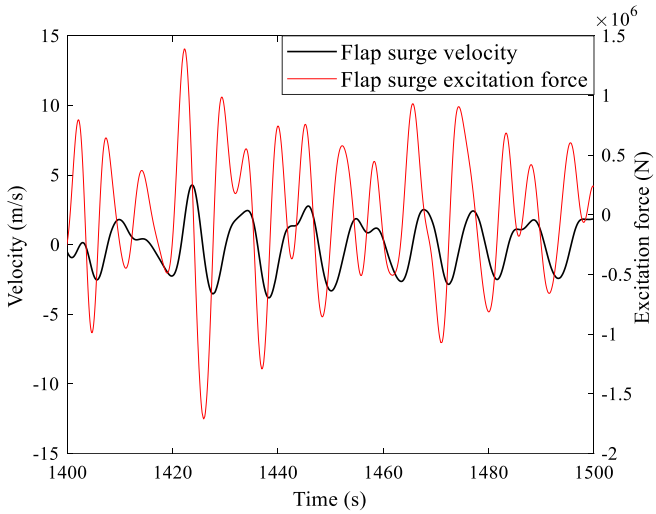

Figure 4-15 Surge excitation force and Flap 2 corresponding velocity in EC6 (max power production)

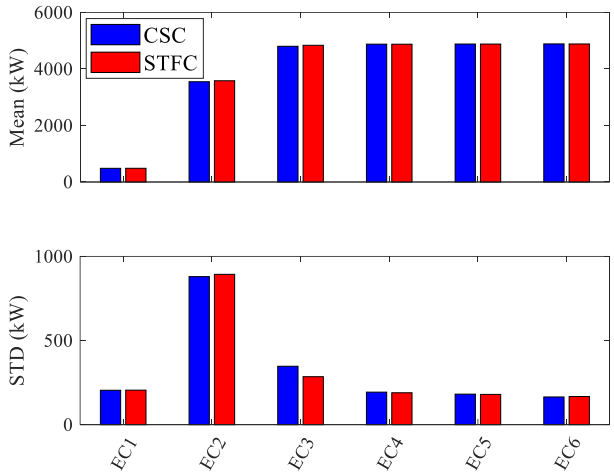

Figure 4-17 Wind Turbine power production

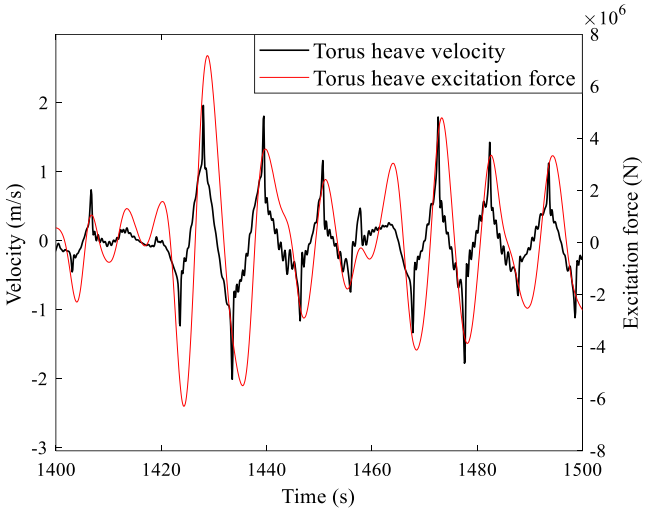

Figure 4-18 Heave excitation force and torus corresponding velocity in EC6 (max power production)

STFC WECs mean power production

In Figure 4-14, The WEC mean absorbed power and standard deviation is presented. A linear increase in power absorption and standard deviation throughout the ECs is noted. On the contrary, the wind turbine power production standard deviation is significantly reduced in EC3 comparing to EC2 and remains the same across EC4 to EC6. This can be attributed to the controller acting above 11.4 m/s wind speed keeping a constant power output. The WECs on the other hand have only passive control meaning constant stiffness and damping coefficients thus the increasing power production and standard deviation with the weather state. Taking a closer look at Figures 4-16 and 4-18, the in-phase oscillation of torus with heave excitation force and the out of phase oscillation of surge excitation force with flap2 is observed. That's the reason that Torus outperforms all the flaps combined. The out of phase oscillation is also an indication that active damping control could increase the power absorption of flap type WECs.

4.4 STFC Estimation of annual power production

To compute the annual power production of STFC, it is important to consider the characteristic of stochastic variations in the wind speed. The annual power production could be roughly estimated through the distribution of mean wind speed and power production. Modeling the distribution of wind speed involves the use of a probability density function. At the location chosen in the North Sea, a two-parameter Weibull distribution proposed by Johansen [80] is utilized to characterize the marginal distribution of 1-hour mean wind speed at 10m height, u10, as demonstrated in the equation below where $\alpha = 1.708$ and $\beta = 8.426$ are the shape and scale parameters, respectively. Similar methodology is followed from Cheng et al. [83].

$$F(u_{10}) = 1 - e^{-\left(\frac{u_{10}}{\beta}\right)^{\alpha}} \quad (31)$$

To increase the resolution of the annual power calculation, a finer bin discretization was chosen. 5 more environmental cases within the cut in and cut off range are generated through the power of law equation

$$u_{10}(u_{ref}) = u_{ref} \times \left(\frac{z_{10}}{z_{ref}}\right)^{\gamma} \quad (32)$$

Where z_{ref} = 90m, u_{ref} is the wind speed in 90m height and γ = 0.14. The environmental cases generated are mentioned in numerical modeling. The annual power production can be obtained by the summation of the product of the yearly mean power and the probability of mean wind speed within a year.

The probability distribution function is described by the equation XX and the plotted distribution with the ECs marked are shown in Figure 4-19 and 4-20.

$$f(u_{10}) = \frac{\alpha}{\beta} \times \left(\frac{u_{10}}{\beta}\right)^{\alpha-1} \times e^{-\left(\frac{u_{10}}{\beta}\right)^{\alpha}} \quad (33)$$

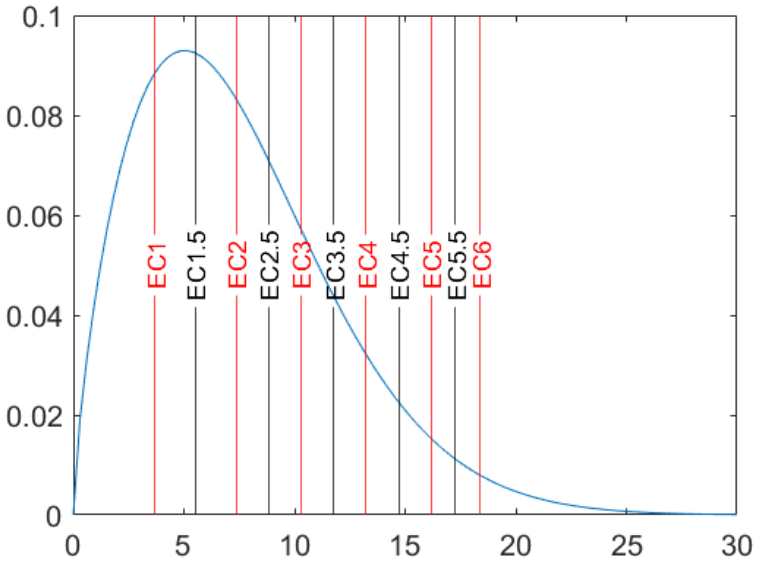

Figure 4-19 Probability density function with the ECs marked

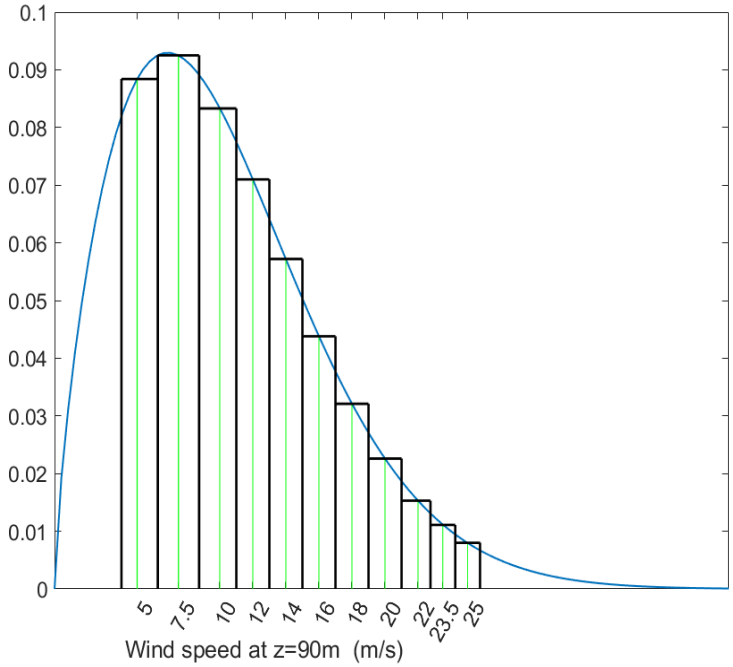

Figure 4-20 Probability of occurrence for each sea state

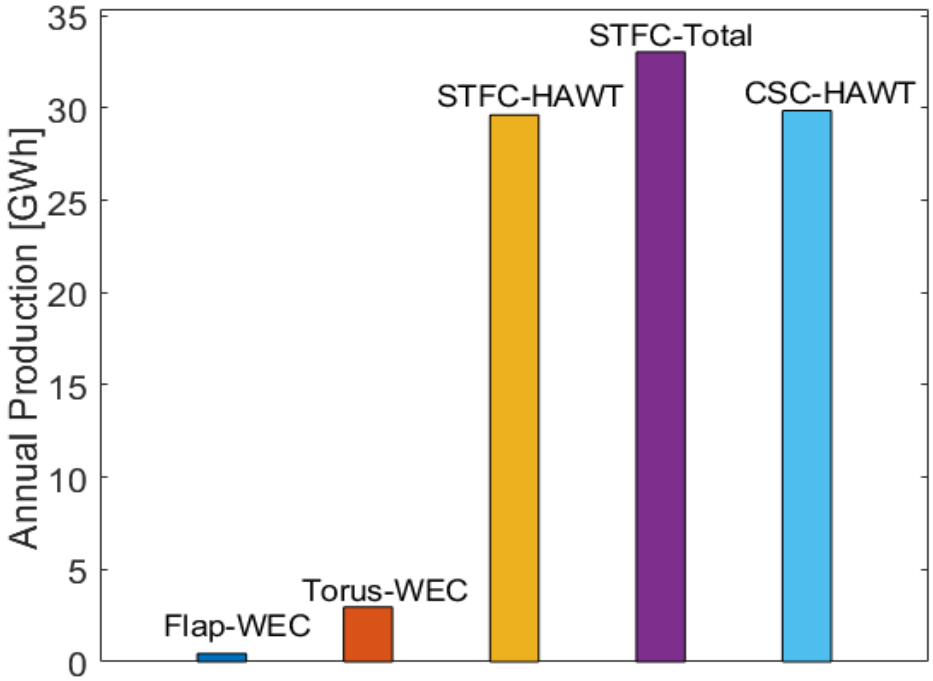

Figure 4-21 Prediction of annual power production for the WECs, STFC, STFC HAWT, CSC.

In Figure 4-21, the annual predicted power production is presented. There is a good agreement between the STFC and CSC wind turbines validating the previous findings that the addition of WECs doesn't significantly affect. The flap type WECs produce only 0.444 GWh, just 14% of what a single torus is producing. Torus produces 2.9 GWh consisting 9% of the total power produced by the STFC concept annually. The STFC outperforms the CSC with a 10% increase in energy production.

Judging by the current configuration, the addition of flaps without active damping and stiffness control seems to be in vain. The addition of torus on the other hand is a promising concept. The wind turbine in both cases of SFC and STFC didn't presented any significant change.

5 RESULTS AND DISCUSSION FOR THE HYBRID MOORING CONCEPT CCCB

5.1 Decay test

The equilibrium position mooring top angle from the vertical of STFC 200m moored with a simple chain-clump catenary and the STFC 50m moored with the hybrid mooring CCCB are quite the same. The 200SC has 62deg and the 50CCCB has 65deg top angle measured from the vertical. Given the fact also that the pretension has been adjusted to the later in order to be the same as the 200SC, the effect of the new mooring lines will be negligible in the natural period of the STFC

The 50CCCB though is tested in parked conditions also. The same way the wind turbine is parked, the WECs also should be parked. As the wind and waves are correlated, the cut off conditions are the same for both the turbine and the WECs. In this study, the WECs are in operational condition. As a reference, the torus has two survival condition options. It can be put in parked condition by either ballasting it, submerging it to the lower stroke position z=-3m, and locking it or locking it at the mean water level z=0 [84]. The flaps are simply set free to rotate with no connection to the PTO mechanisms [85]. Thus, the effect of locked torus and free flaps will not be captured at the platform motions during survival conditions LC8 and LC9 and no "parked" natural period is calculated

5.2 System restoring forces

The design that the CCCB will be compared against is the IV Chain-Clump-Buoy (CCB) from Xun et al. [45]. Except the obvious differences in designing, the IV concept has some basic operational differences from the CCCB that are pointed out and referred later in the results discussion.

- Xu's model (CCB) supports a 5 MW NREL turbine placed on an OC4 semi-submersible floater with 20m draft.
- CCCB supports a 5MW NREL turbine placed on a CSC semi-submersible floater with 30m draft.

- The closest thing they share is the displacement which is 13470000kg and 10555000kg for the IV and for the CCCB respectively.
- The zero offset top angle of IV is 57deg whereas CCCB is 65deg.
- The pretension of CCCB is adjusted to meet the STFC 200m value whereas the IV model is only 50% of it. See table 5-1

Table 5-1 Pretension values

STFC 200m	CCB Chain-Clump-Buoy	CCCB Clump-Chain-Clump-Buoy
1628KN	859 KN	1572 KN

- The CCB orientation utilizes one mooring line parallel to waves and wind propagation. CCCB utilizes two mooring lines with 60deg angle on each side of the sea state propagation orientation.
- Xu is also calculating the difference frequency second order effect of waves while this thesis takes into consideration only the first order effect.
- Both CCB model and CCCB use 935m long mooring lines.

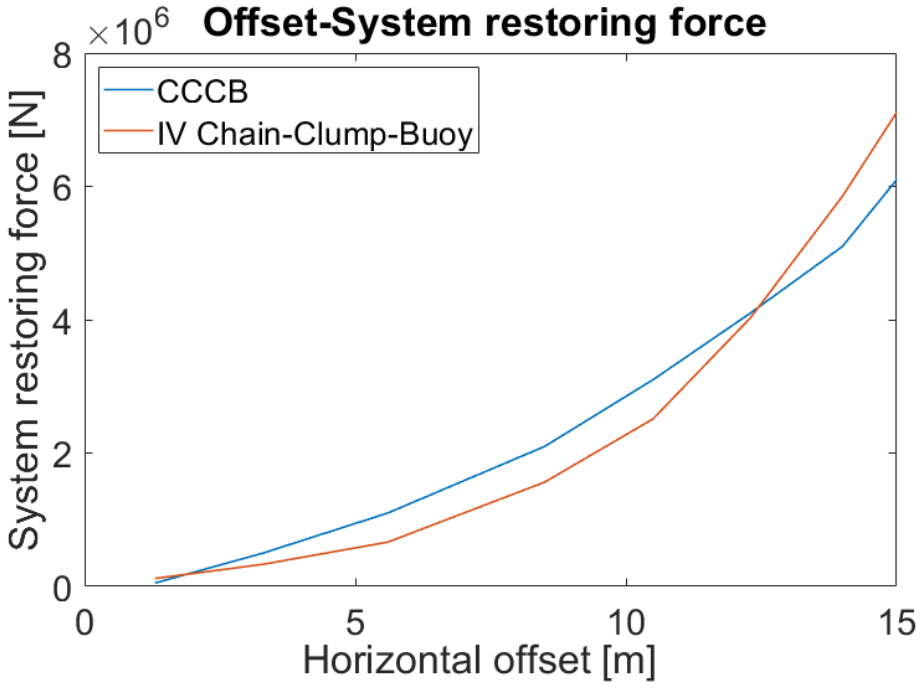

Figure 5-1 System restoring force.

In the above Figure 5-1 the horizontal restoring force of the mooring system is presented. At 15m offset, a smaller restoring force for the CCCB is observed. It was expected and is due to the orientation of the mooring lines. This Y shape, 120deg apart, mooring line configuration has

a different restoring force between offset in x and -x direction and that explains the higher restoring force of the CCB model.

The increased pretension is achieved mainly by increasing the weight of the material but also by increasing the position of the anchors. Xu's model is using the same mooring line length as the CCCB and half the pretension. This means that the sagging of CCB's mooring line is bigger than the CCCB. The anchors' position is also closer to the platform and the catenary shape has smaller initial top angle. This results in a superior catenary shape compared to the CCCB design.

Their main difference is that the IV model follows the recommended admissible floater offset to water depth ratio of 0.3 at 50m depth proposed by Campanile et al. [86] thus the low pretension. During extreme weather condition EC5, CCB model experiences 12m surge offset accounting for 0.24 ratio of the water depth. On the other hand, the CCCB having higher pretension reaches up to 14% of the water depth with maximum surge offset of 7m.

5.3 Irregular waves and turbulent wind tests.

After establishing the differences between the two systems the results from the irregular wave tests are presented in the following figures. The values for the IV model are extracted from Xu et al. [45]. 6 simulations of 4000s with different wave seeds for each of the 5 environmental cases are performed for the CCCB. EC1, EC2, and EC3 are operational conditions for both the wind turbine and the WECs. In EC4 the wind turbine is parked with the WECs in operation and in EC5 we have the same conditions with EC4 with the addition of 1 m/s current.

In Figure 5-2, the surge motion of both floaters is captured. Significantly higher values for the maximum surge offset are noticed for the CCB model. There are two procedural reasons for that and one practical. Starting from the procedural and statistically wise, the difference could be accounted to the fact that the values from Xu et al. [45] are extracted from ten 3 hours simulations for each weather state. Another reason that the motions are higher is the fact that in this thesis only the first order wave effect is accounted for, thus the slow drift difference frequency effects are not calculated. This can be quantified though by taking a closer look at the mean values of EC4 and LC5. In EC4, the wind turbines are set to parked conditions reducing the wind thrust effect to minimum. While the mean force from the wind is eliminated, the CCCB model

experiences higher mean value than the CCB. Both structures have a negligible mean surge magnitude though so we can consider the two values equal, meaning that the effect of the second order forces is not high enough. The practical reason that the CCCB experiences lower surge motions is that it's a stiffer model not allowing the floater to move that far. Even though in Figure 5-1 the maximum restoring forces seem to be close, these values are added on the pretension, which is higher for the CCCB, so in total it exerts higher forces to the floater.

In Figure 5-3, the heave motion is presented. There is a trend that can be noticed through weather conditions 1 to 5 where in the first three, the CCCB model has higher mean and max values, but this is reversed in last two ECs. This can be attributed to some imbalances in the CCB model as its equilibrium position is not at z=0 but close to z=0.2. At the last two ECs the surge offset is large enough and the downward forces have increased thus the CCCB mean, max and standard deviation values are less than the CCB.

In Figure 5-4, the pitch motion is presented. Another pattern can be noted in this figure as during EC1 CCB experiences higher max and mean values whereas in EC2 and EC3 CCCB takes the lead. The first weather state pitch rotation difference between the floaters can be attributed to the higher pretension of the CCCB. The CCB having lower pretension is more prone to pitching during the lower sea states. Moving though to EC2 and EC3 the wind thrust increases to maximum and the tower moment increases. The lower pitch response of CCB can be attributed firstly to the increased inertia due to the bigger displacement of the OC4 compared with the CSC, secondly to the larger offset of the columns of OC4 compared with the STFC creating a bigger restoring moment and lastly to the different orientation of the two floaters. The STFC while rotating towards the positive pitch direction, utilizes only one submerged column of 6.5m diameter while the OC4 utilizes two submerged columns of 10m diameter. This results in higher pitch stiffness C55, thus the decreased pitch motion. Looking at the parked conditions EC4 and EC5, the mean pitch value for both floaters plummets to almost zero and this is the result of the absence of wind thrust. The maximum values remain substantially higher for CCB, and this can be attributed to the increased simulation time that allowed the capturing of these maximum values. It can not be attributed to any structural reason.

In Figure 5-5, the statistics of mooring line tension are presented. As it was expected, the mean values of CCCB are higher than CCB across all ECs. The much-expected reduction in tension for both CCB and CCCB in EC4 is attributed to the reduction of wind thrust. The maximum value though for the CCB is much higher than the CCCB and the duration of

simulations is once again the reason. Because of the number of maximum vales being recorded, the standard deviation of CCB is equally higher than the CCCB.

The outcome of the irregular waves tests is that even though both designs utilize more or less the same structural characteristics, the stiffness of CCCB makes it a more appropriate design for equally lightweight structures as STFC equipped with wave energy converters. The CCCB design could be characterized as an overdesigning concept taking into account that its maximum responses reach to half the offset to depth ratio that is proposed by Campanile et al. [86]. The STFC model though would require a much firmer position keeping ability because of the wave energy converters. The steadier the floater, the higher the motions that are induced to the wave energy converters. The exact benefit from the increases power production in relation to the increased cost of the mooring line is something that should be investigated further.

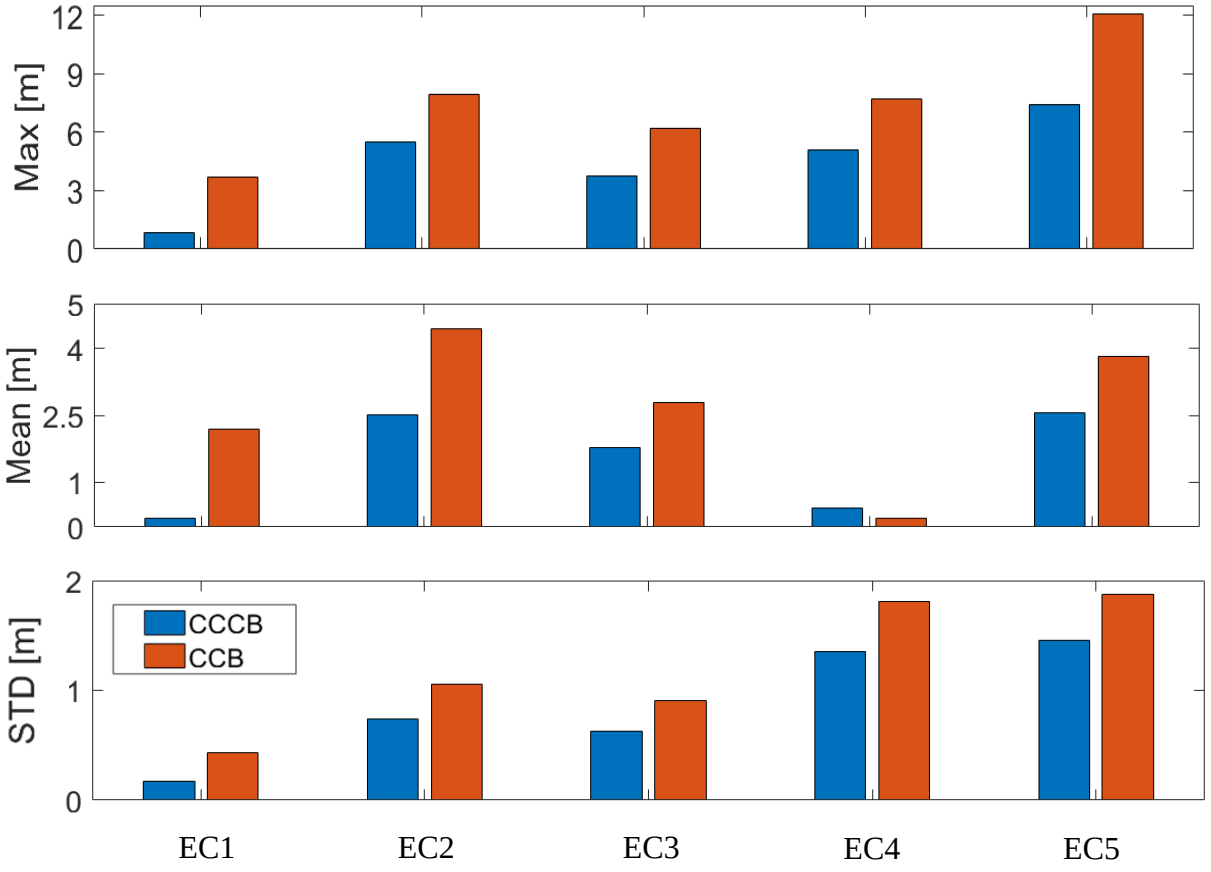

Figure 5-2 Surge

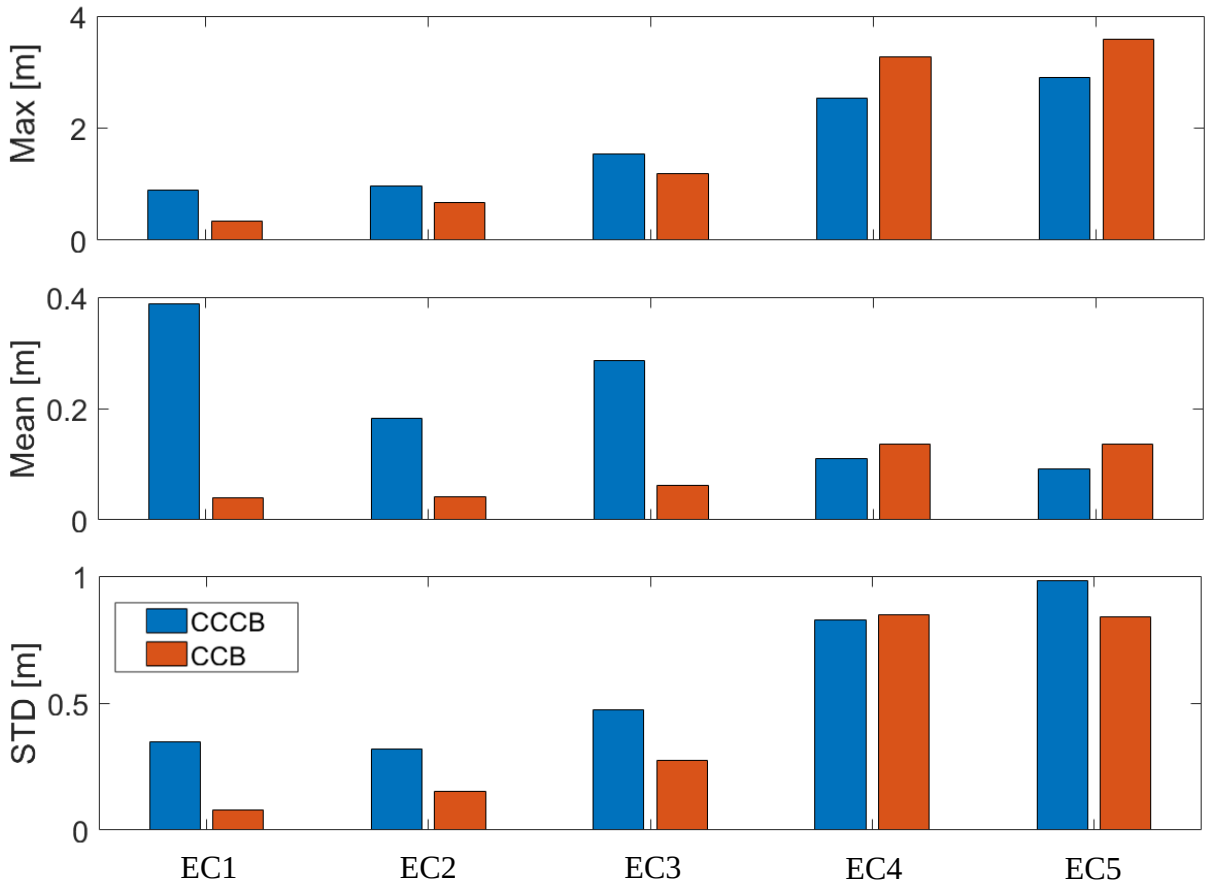

Figure 5-3 Heave

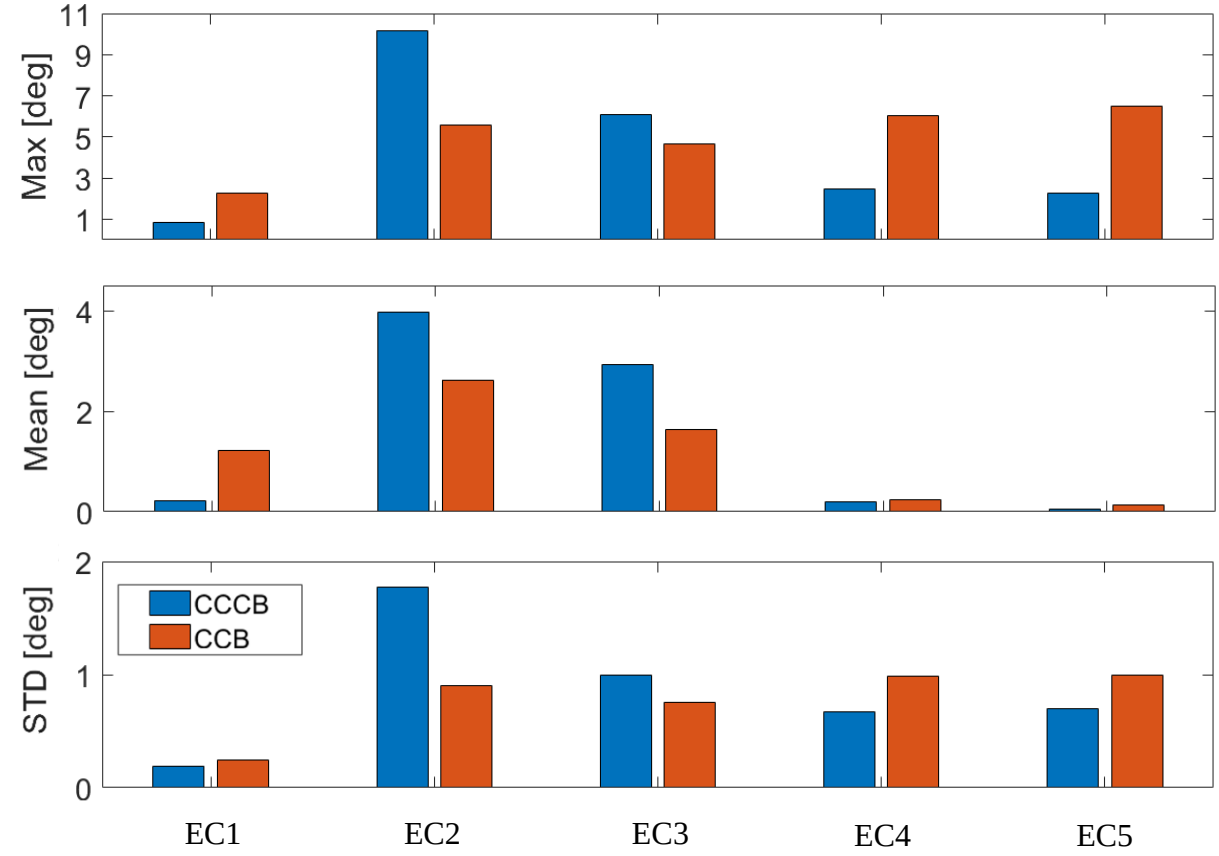

Figure 5-4 Pitch

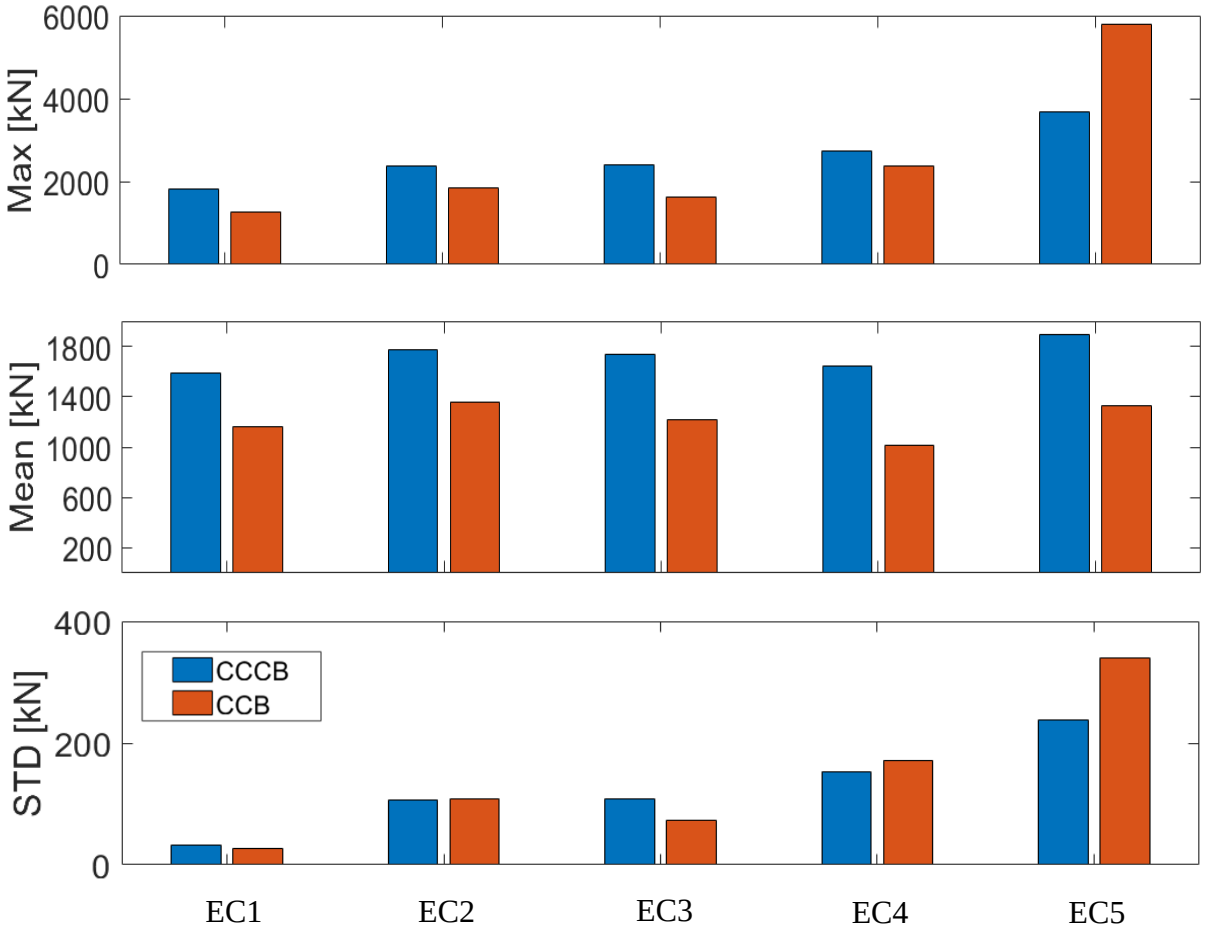

Figure 5-5 Statistics of mooring line tension

5.4 Spectra for mooring line tension from EC1 to EC5

In the present part of thesis, the spectra of the mooring line tension will be presented in three points across the mooring line. The position of these points is presented in the Table 5-2.

Table 5-2 Points across the mooring line

Point identifier	Point description
P_1	Seg. 1 el. 1 (Fairlead position)
P_2	Seg. 4 el. 40 (Follow buoy1)
P_3	Seg. 5 el. 30 (Follow buoy2)

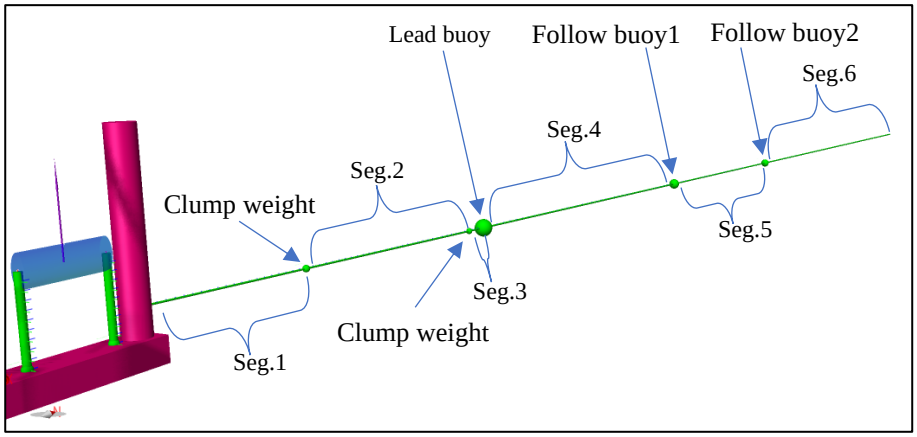

Figure 5-6 Mooring line segmentation

As it can be seen also from Figures 5-6 and 5-7, the P_1 is located at the fairlead in segment one, the P_2 is located close to the Follow buoy1 and P_3 is located close to Follow buoy2. The purpose of reading the power spectra is to quantify the power magnitude and frequency distribution across the mooring line and the effect of the buoys.

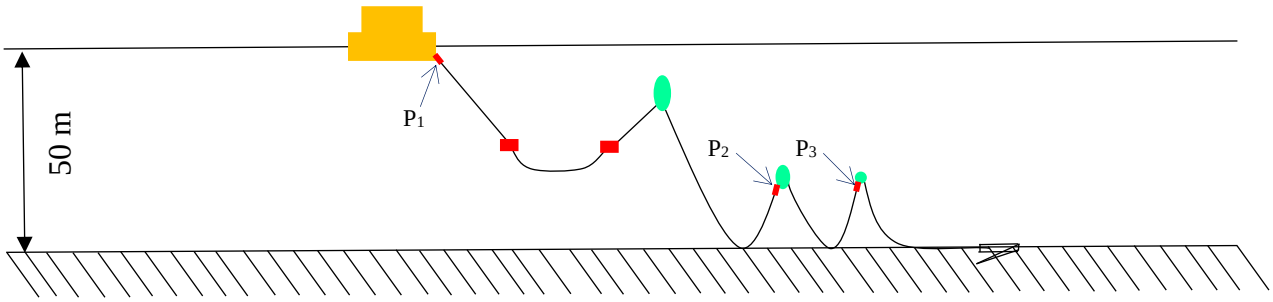

Figure 5-7 Schematic representation of the CCCB and the points P_1, P_2 and P_3

The bellow Figures 5-8 (EC1) to 5-12 (EC5) are a representation of the energy distribution starting from the Fairlead (P_1) and reaching up to the Follow buoy2 (P_2) which is the last floating part of the mooring line.

A high frequency response point is observed in EC1,2, and 3. The frequency of this point is progressively increasing throughout the first three weather states. It starts from 6.3 rad/s in Figure 5-8 P_1 and reaches to 25rad/s in Figure 5.4-5 P_1. Its frequency doubles at every sea state and it is eliminated in P_2 and P_3 at all sea states. The source of this power frequency is different than the wave frequency. After the transition from P_1 to P_2 the high frequency power response can not be detected. At sea states 4 and 5 though, the wave resonance response is amplified in a way that seems like it's absorbing the high frequency power. The same thing does not happen for EC1,2, and 3. The only thing changing between EC1,2,3 and EC4,5 is the parked condition and as a consequence the wind thrust. During EC4 and EC5 that the wind and waves are the same, the high frequency response has the same magnitude and frequency. The reason why this high frequency is added to the wave resonance at the parked conditions after the Follow buoy is that the wind thrust is reduced, and the standard deviation eliminated. At the operational conditions though the standard deviation remains high. By looking closer at all the Figures, it is noticed that the Lead buoy acts as a damper of the frequency signals, creating a more unilateral loading to the rest of the mooring line hanging from the Follow buoy1 and Follow buoy2. The high frequency response occurring only at the first part of the mooring line is the effect of the Lead buoy that is oscillating in the heave direction

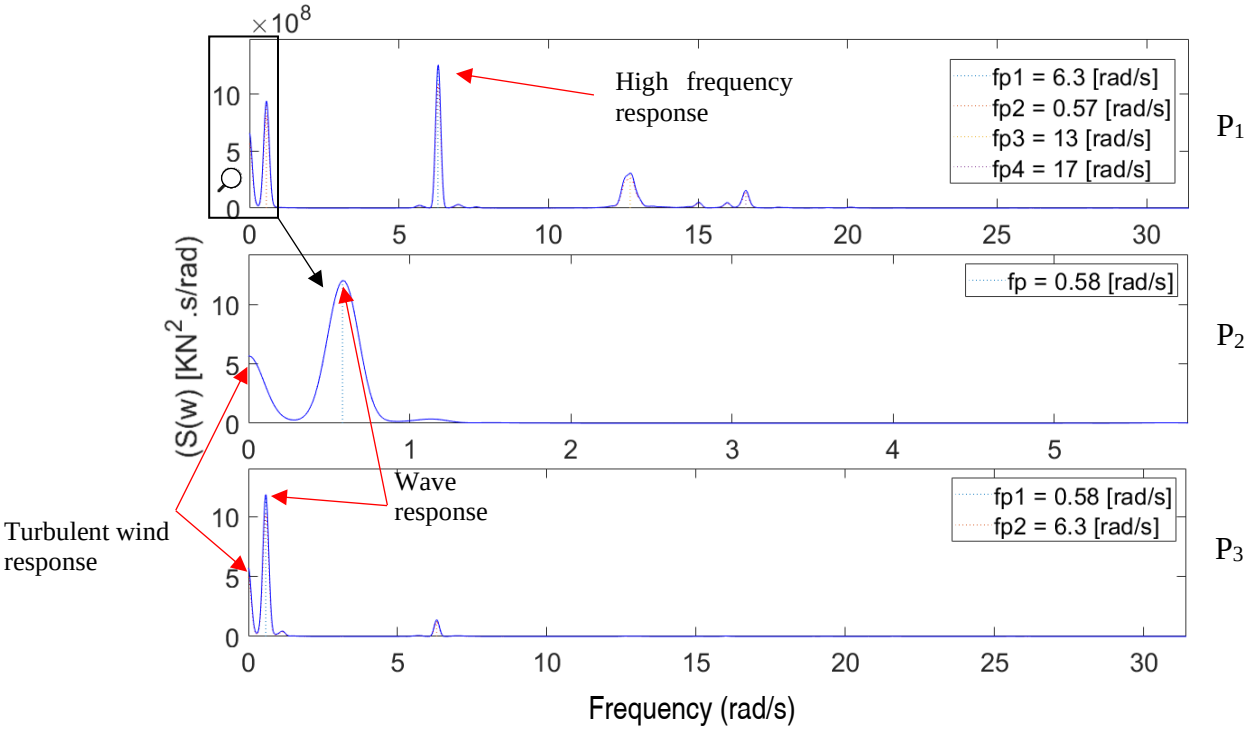

Figure 5-8 Spectra for mooring line tension in LC1

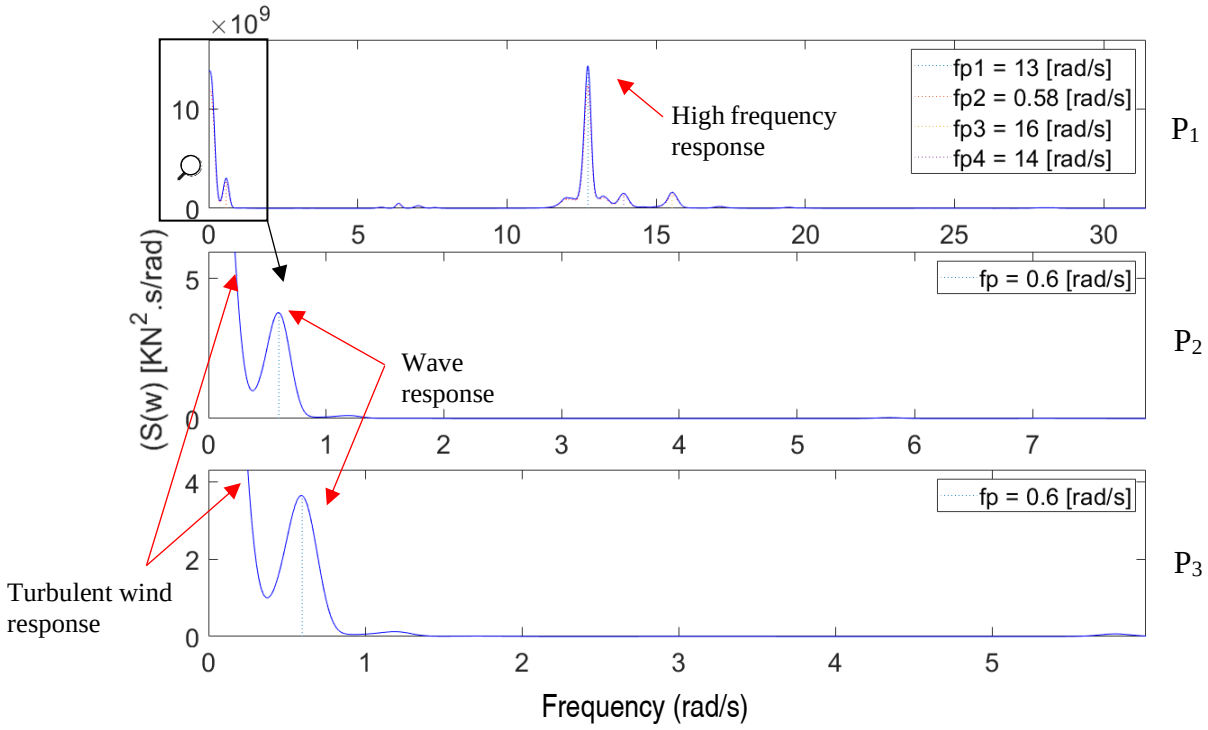

Figure 5-9 Spectra for mooring line tension in LC2

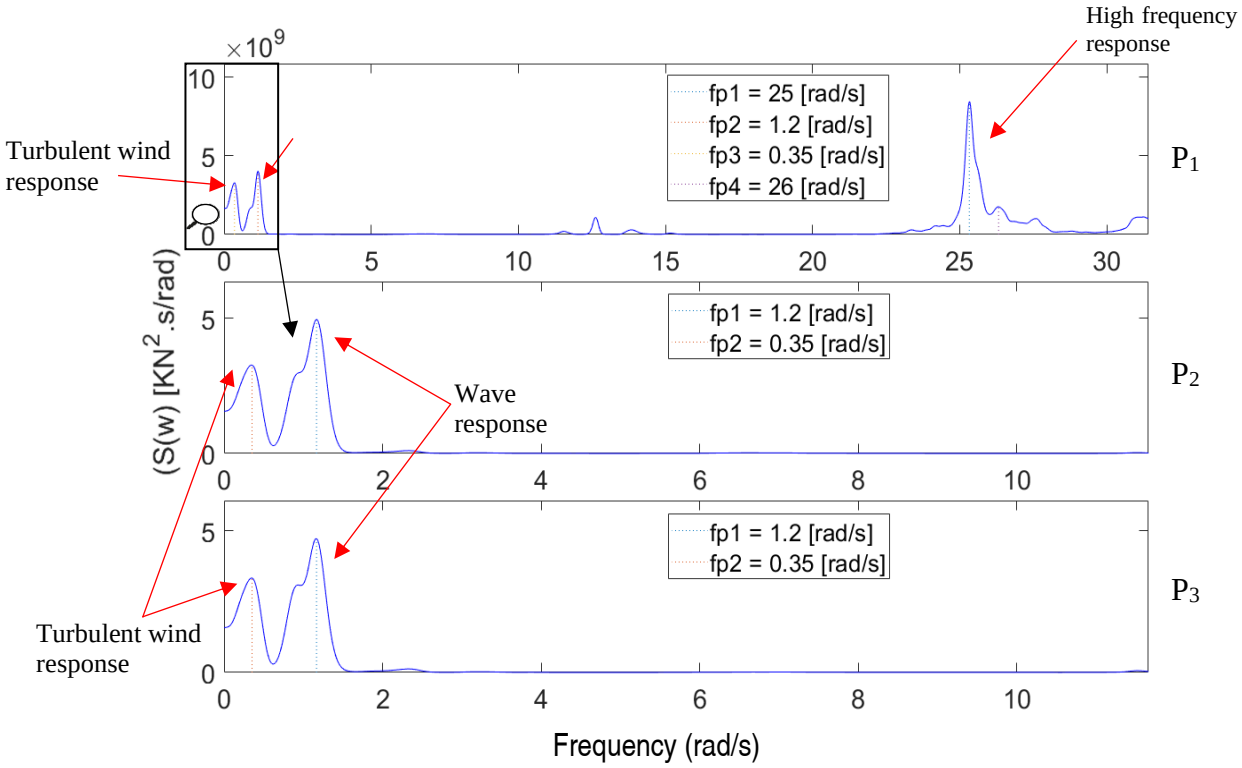

Figure 5-10 Spectra for mooring line tension in LC3

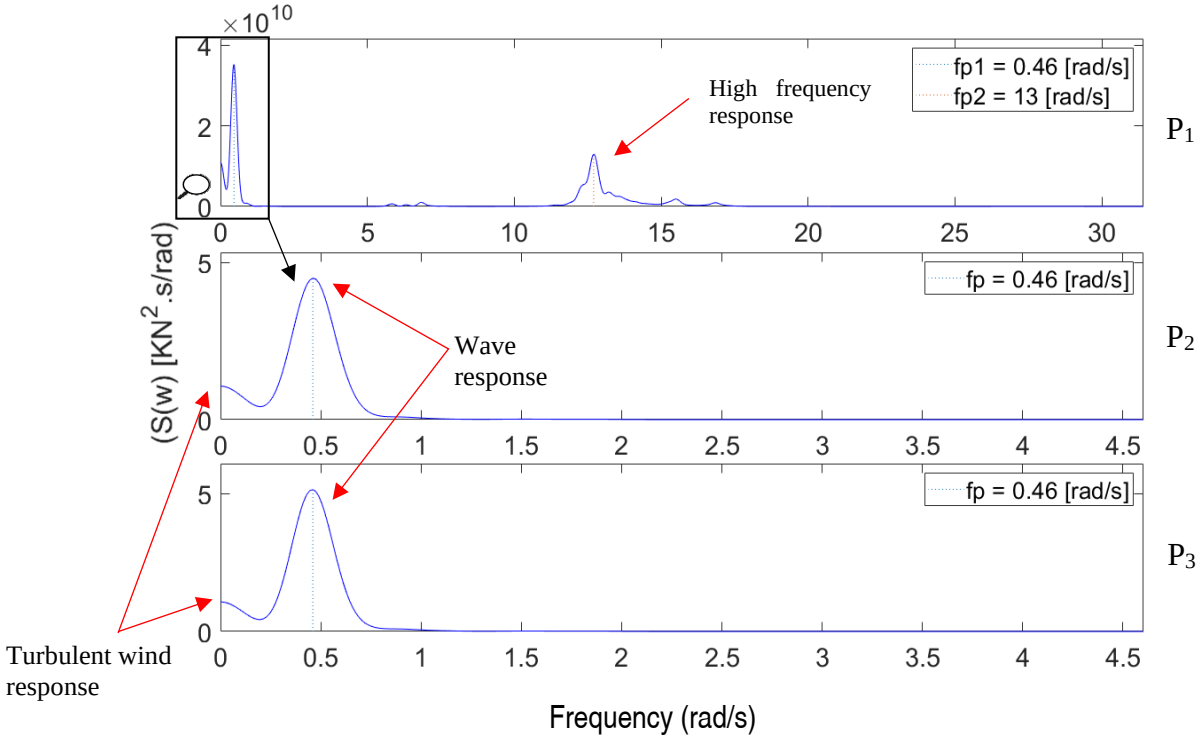

Figure 5-11 Spectra for mooring line tension in LC4

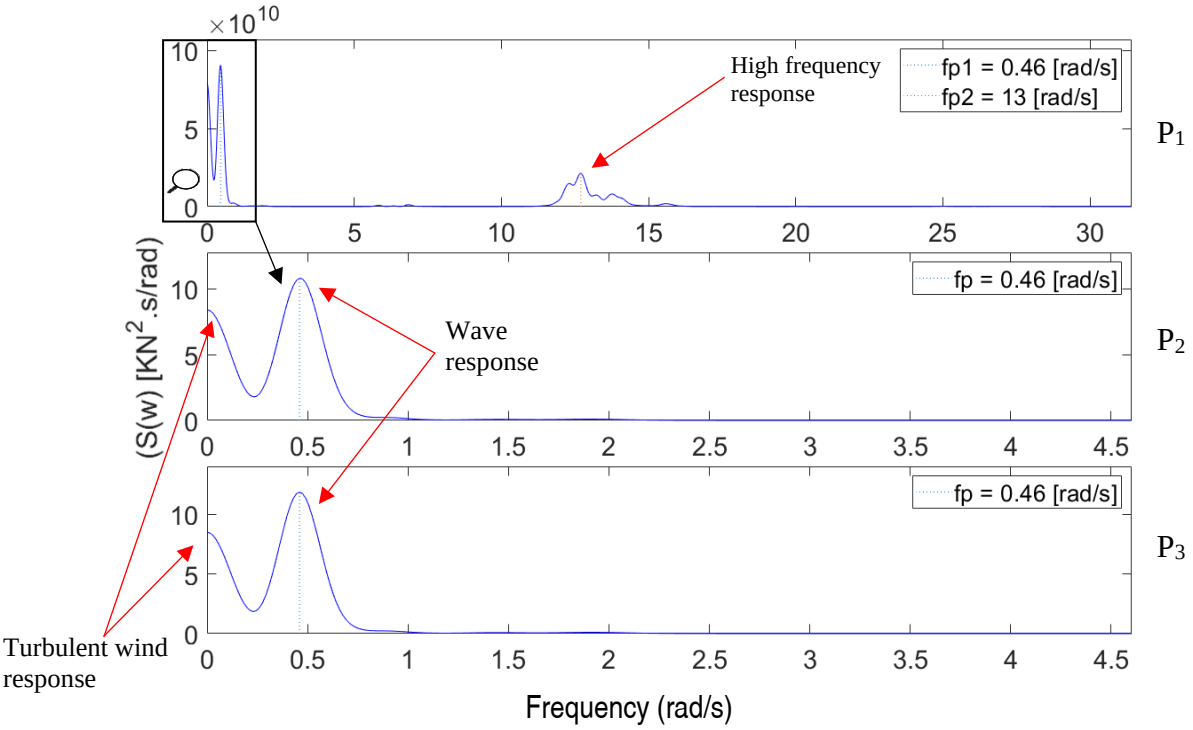

Figure 5-12 Spectra for mooring line tension in LC5

Finally, the utilization factor is presented. The proposed mooring line is divided into two sections, the one with 300kg/m and the one with 500kg/m. Since the fact that the simulations performed are 1-hour simulations the maxima of responses is not captured. The formula for calculating the utilization factor requires to plug in the most probable mooring line maximum tension. Trying to be more conservative than the guidelines from DNVGL 2018b [87], with the available data, the maximum mooring line value obtained is used. The steel grade chosen is R4-RQ4.

$$u = \frac{T_{pret} * \gamma_{pret} + T_{c-env} * \gamma_{env}}{S_C} \tag{34}$$

Following Xu et al [45] methodology, γ_{pret} and γ_{env} are safety factors and are set to 1.3 and 1.75 respectively based on the assumption of level 1 consequence class. T_{c-env} is the characteristic environmental tension, meaning the excess tension that is applied to the mooring line with increasing offset. It is calculated as $T_{MPM} - T_{pret}$, where T_{MPM} is equal to 0.95% of the minimum breaking load of the mooring line. The weak part of the mooring line with 300kg/m, has minimum breaking load equal to 12993 KN and the strong part with 506kg/m, equal to 20156KN. The safety factor obtained is 0.5 and 0.3 for the weak and strong part respectively. This is a rough calculation as the weak part, touching the seabed, is not subjected to the same pretension as the heavy one that hangs on the floater. With this preliminary assessment is obvious that this is a

conservative design and the there is a lot of room for increasing the weight of the floater with installing a larger wind turbine or rearrange the catenary design with lighter material and cut down cost.

6 CONCLUSIONS AND RECOMMENDATIONS FOR FUTURE WORK

The first part of the thesis presents a global analysis and power performance of a combination of a floating wind turbine, flap type and two-point absorber type wave energy converters (STFC) deployed at 200m water depth. The results indicate that the addition of wave energy converters doesn't significantly affect the motion of the structure under operational conditions. Furthermore, the power performance analysis indicates that the addition of wave energy converters increases the power production. In details the main conclusions throughout the thesis are the following.

- The SFC and STFC models' natural periods are measured. A step analysis of the change in natural period by adding each type of WEC is performed. The overall behavior of the floater doesn't change significantly. The addition of flaps increases the periods in all degrees of freedom due to increase in mass. The addition of Torus increases the natural periods in all three degrees of translation and slightly in yaw rotation. The pitch and roll natural periods are reduced by the addition of Torus due to increased hydrostatic stiffness. The effect PTO mechanisms doesn't affect the natural periods.

- Regular wave test is performed for SFC and STFC models. The SFC data show good agreement with the experimental data published by Michailides et al. [82]. The influence of the WECs to the platform RAO is observed. Floater surge and pitch RAO experience a peak close to the flap rotation natural period. Floater heave RAO experiences a peak close to Torus natural period. The absorbed power RAO plot indicates that Torus's efficiency remains high for a wide spectrum of frequencies.

- The motions of STFC are almost identical with the CSC motions under operational conditions. This is an indication that no extra mooring arrangements will be required. The installation of WECs doesn't significantly affect the mean surge offset. A small reduction in pitch motion is observed due to the addition of Torus and the increase of hydrostatic stiffness.

- The mean and annual power production of Torus, flaps and HAWT is evaluated. The installation of WECs has little to no influence at the wind turbine power production. Torus significantly outperforms the flaps. The flaps with the current configuration produce little to negligible power. Torus produces 9% of the total STFC power production and flaps only 14% of Torus produced power. STFC outperforms CSC by 10%.

- The reason that the flaps don't produce energy is that their rotation is out of phase with the first order surge excitation force. The flaps can not be efficient as long as they have passive control meaning constant damping and stiffness.

The second part of the thesis presents the design and assessment of a hybrid mooring arrangement following the methodology and criteria of Xu et al. [45]. The overall behavior of the new design in operational and parked conditions is satisfactory. Based on the given loading conditions the design is a promising concept. In details, the main conclusions are the following:

- A system restoring force test is performed. The results indicate that the new design's system restoring force maintain a relatively linear behavior throughout the offset range of 30% of the water depth.

- The irregular waves test indicates that an important parameter dictating the maximum offset of the floater is the pretension of the mooring line. The CCCB floater experiences smaller offset mean values throughout the whole range of loading conditions compared to the CCB mainly due to the increased pretension.

- The surge offset of the floater is restricted to 14% of the water depth while keeping the maximum tension within acceptable limits. This is almost 50% less than the 30% initial target.

- The main design criteria is that the floater shouldn't experience large offsets so that the power cables don't experience high stresses. The CCCB design excels in this criterion.

- The power spectra analysis is performed in three designated points along the mooring line. A smoother power spectra is observed in points P2 and P3. This is attributed to the damping providing by the Lead buoy. It' s heave motions isolate the two seafloor touching catenaries.

- The utilization factor for the two sections of the mooring line is obtained. With 0.3 and 0.5 for the heavy and lightweight part respectively, the design is withing safe limits. The CCCB arrangement can be used in a variety of applications where heavier floaters are used. For less demanding applications a weight reduction can applied.

Throughout the process of working on the thesis, there are a few points where future work could help obtaining a better understanding of the proposed concepts.

- Torus bearing numerical modeling. The modeling of the bearing system of Torus is a rough design. From the data obtained it's obvious that the coupling of torus and floater in pitch and roll directions is not accurately represented. Torus experiences way higher pitch and roll motions than the floater. This is because the arrangement of the docking cone is some how loose. The proposal that would counteract this problem in a simple way is the use of more than three cones with variable cone and pin elevations. A preliminary modeling has shown that it works, and it also affects the power production.

- Flaps passive control. The flaps in their current configuration are not producing enough power to justify further research. To conclude if the flap type WECs can be productive a new study with active damping and stiffness control should be made in order to bring the flap rotation in phase with the excitation force.

- Regarding the CCCB concept, a full mooring analysis with 3hr simulations and the inclusion of second order wave effects would help evaluate better the proposed concept.

- A lot of things can be done also design wise, such as emerging the fairleads to increase the suspended catenary length, but special attention should be given to the possibility of mooring chain and structure clashing.

- To increase the drag forces of the intermediate water mooring line, plates oriented perpendicular to the surge direction could be added along the mooring length thus increasing the damping and added mass

- For less demanding applications, a cost reduction effort can be made by reducing the size of the chain. A list of possible arrangements with varying properties could be made for various applications.

7 REFERENCES

[1]. Lindsay, Robert B. (1975). Energy: Historical Development of the Concept. Dowden, Hutchinson & Ross.

[2]. Burnet, J. (1892). Early Greek Philosophy. United Kingdom: Adam and Charles Black.

[3]. Britannica, T. Editors of Encyclopedia (2019, November 13). *heterotroph*. *Encyclopedia Britannica*. https://www.britannica.com/science/heterotroph

[4]. Gregory, T.R. Understanding Natural Selection: Essential Concepts and Common Misconceptions. Evo Edu Outreach 2, 156–175 (2009). https://doi.org/10.1007/s12052-009-0128-1

[5]. Eckhardt N. A. (2010). Evolution of domesticated bread wheat. The Plant cell, 22(4), 993. https://doi.org/10.1105/tpc.110.220410

[6]. Aeschylus, James Scully, and C J. Herington. Prometheus Bound. New York: Oxford University Press, 1975. Print.

[7]. Wrangham, R. W. (2009). Catching fire: How cooking made us human. New York: Basic Books.

[8]. Schwab, K. S. (2016, January 16). *The Fourth Industrial Revolution: what it means, how to respond*. World Economic Forum. Retrieved May 20, 2022, from https://www.weforum.org/agenda/2016/01/the-fourth-industrial-revolution-what-it-means-and-how-to-respond/

[9]. Deloitte. (2020). The Fourth Industrial Revolution At the intersection of readiness and responsibility. https://www2.deloitte.com/content/dam/Deloitte/de/Documents/human-capital/Deloitte_Review_26_Fourth_Industrial_Revolution.pdf

[10]. Kershner, M. K. (2021, July 15). Data Isn't The New Oil — Time Is. Forbes. Retrieved May 21, 2022, from https://www.forbes.com/sites/theyec/2021/07/15/data-isnt-the-new-oil--time-is/?sh=70af391535bb

[11]. BP. (2022, January). Statistical Review of World Energy. Bp Statistics. https://www.bp.com/content/dam/bp/business-sites/en/global/corporate/pdfs/energy economics/statistical-review/bp-stats-review-2021-full-report.pdf

[12]. Our world in data. (2022, January 1). Our world in data. Retrieved May 23, 2022, from https://ourworldindata.org/energy-substitution-method

[13]. International renewable energy agency. (2022, January 1). Https://Www.Irena.Org/Wind. Retrieved May 23, 2022, from https://www.irena.org/wind

[14]. Hywind Scotland. (2017). Equinor. https://www.equinor.com/energy/hywind-scotland

[15]. Windfloat Atlantic. (2019). EDP. https://www.edp.com/en/innovation/windfloat

[16]. Kincardine Offshore Floating Wind Farm. (2020, October 9). GRUPO COBRA. https://www.grupocobra.com/en/proyecto/kincardine-offshore-floating-wind-farm/

[17]. BW Ideol signs an agreement with EDF Renewables & Maple Power for the upcoming floating wind tender in the Mediterranean Sea. (2022, May 23). IDEOL. https://bw-ideol.com/en

[18]. Global Wind Atlas. (2022). Energydata Info. https://globalwindatlas.info/

[19]. Fox, A. D., Desholm, M., Kahlert, J., Christensen, T. K., & Krag Petersen, I. B. (2006). Information needs to support environmental impact assessment of the effects of European marine offshore wind farms on birds. Ibis, 148, 129-144.

[20]. Petersen, I. K., & Fox, A. D. (2007). Changes in bird habitat utilization around the Horns Rev 1 offshore wind farm, with particular.

[21]. Myhr, A., Bjerkseter, C., Ågotnes, A., & Nygaard, T. A. (2014). Levelised cost of energy for offshore floating wind turbines in a life cycle perspective. *Renewable energy*, 66, 714-728.

[22]. Stehly, T. S., Beiter, P. B., & Duffy, P. D. (2020, December). *2019 Cost of Wind Energy Review* (National Renewable Energy Laboratory, Ed.; NREL/TP-5000-78471). National Renewable Energy Laboratory. https://www.nrel.gov/docs/fy21osti/78471.pdf

[23]. Tønseth, S. (2021, July 19). *Six factors that will determine the cost of offshore wind power. Norwegian* SciTech News. https://norwegianscitechnews.com/2021/07/six-factors-that-will-determine-the-cost-of-offshore-wind-power/

[24]. Ebbesen, M. E. (2022). *Floating Offshore Wind Commercializing with confidence*. DNV. https://www.dnv.com/focus-areas/floating-offshore-wind/index.html

[25]. Energy is in our Nature. (2022). Clarus offshore. https://clarusoffshorewindfarm.com/

[26]. Kallehave D, Byrne BW, LeBlanc Thilsted C, Mikkelsen KK. 2015Optimization of monopiles for offshore windturbines.Phil.Trans.R.Soc.A373: 20140100.http://dx.doi.org/10.1098/rsta.2014.0100

[27]. Daubney, K. (2013, October 9). *IN DEPTH: Cost imperative drives monopiles to new depths.* Windpower Monthly. https://www.windpowermonthly.com/article/1210058/depth-cost-imperative-drives-monopiles-new-depths

[28]. Fore Wind. (2019, March 28). *Overview | Fore Wind*. Fore Wind | Delivering Your Future Energy. https://forewind.co.uk/dogger-bank/overview.html

[29]. Sif Group. (2022, May 17). *Home*. https://sif-group.com/en/

[30]. Smulders. (2022). Smulders. https://www.smulders.com/en/

[31]. Luan, C., Gao, Z., & Moan, T. (2016, June). Design and analysis of a braceless steel 5-mw semi-submersible wind turbine. In International Conference on Offshore Mechanics and Arctic Engineering (Vol. 49972, p. V006T09A052). American Society of Mechanical Engineers.

[32]. Weber, J., Mouwen, F., Parish, A., & Robertson, D. (2009, September). Wavebob—research & development network and tools in the context of systems engineering. In Proc. Eighth European Wave and Tidal Energy Conference, Uppsala, Sweden (Vol. 8, No. 1, pp. 416-420).

[33]. National Renewable Energy Laboratory. (2015, January). Reference Model 5 (RM5): Oscillating Surge Wave Energy Converter (NREL/TP-5000-62861). NREL. https://www.nrel.gov/docs/fy15osti/62861.pdf

[34]. Li, Q., Mi, J., Li, X., Chen, S., Jiang, B., & Zuo, L. (2021). A self-floating oscillating surge wave energy converter. Energy, 230, 120668.

[35]. Luan, C., Michailides, C., Gao, Z., & Moan, T. (2014, June). Modeling and analysis of a 5 MW semi-submersible wind turbine combined with three flap-type wave energy converters. In International Conference on Offshore Mechanics and Arctic Engineering (Vol. 45547, p. V09BT09A028). American Society of Mechanical Engineers.

[36]. National Renewable Energy Laboratory. (2009, February). Definition of a 5-MW Reference Wind Turbine for Offshore System Development (NREL/TP-500-38060). NREL. https://www.nrel.gov/docs/fy09osti/38060.pdf

[37]. Aderinto, T., & Li, H. (2018). Ocean wave energy converters: Status and challenges. Energies, 11(5), 1250

[38]. FlexiFloat®. (n.d.). Flexifloat – Flexible floating system. https://www.uis.no/nb/skaper-nye-losninger-havvind. Retrieved October 1, 2021, from https://flexifloat.no/

[38]. FlexiFloat®. (n.d.). Flexifloat – Flexible floating system. https://www.uis.no/nb/skaper-nye-losninger-havvind. Retrieved October 1, 2021, from https://flexifloat.no/

[39]. McTiernan, K. L., & Sharman, K. T. (2020). Review of Hybrid Offshore Wind and Wave Energy Systems. In Journal of Physics: Conference Series (Vol. 1452, No. 1, p. 012016). IOP Publishing.

[40]. Danish Energy Agency. (2021, February 4). Danish Energy Agency. Https://En.Kefm.Dk/. https://ens.dk/en

[41]. Muliawan, M. J., Karimirad, M., Moan, T., & Gao, Z. (2012, July). STC (Spar-Torus Combination): a combined spar-type floating wind turbine and large point absorber floating wave energy converter—promising and challenging. In International Conference on Offshore Mechanics and Arctic Engineering (Vol. 44946, pp. 667-676). American Society of Mechanical Engineers.

[42]. Soulard, T., Babarit, A., Borgarino, B., Wyns, M., & Harismendy, M. (2013, June). C-HyP: A combined wind and wave energy platform with balanced contributions. In International Conference on Offshore Mechanics and Arctic Engineering (Vol. 55423, p. V008T09A049). American Society of Mechanical Engineers.

[43]. Aubault, A., Alves, M., Sarmento, A. N., Roddier, D., & Peiffer, A. (2011, January). Modeling of an oscillating water column on the floating foundation WindFloat. In International Conference on Offshore Mechanics and Arctic Engineering (Vol. 44373, pp. 235-246).

[44]. Bachynski, E. E., & Moan, T. (2013, June). Point absorber design for a combined wind and wave energy converter on a tension-leg support structure. In International Conference on Offshore Mechanics and Arctic Engineering (Vol. 55423, p. V008T09A025). American Society of Mechanical Engineers.

[45]. Xu, K., Larsen, K., Shao, Y., Zhang, M., Gao, Z., & Moan, T. (2021). Design and comparative analysis of alternative mooring systems for floating wind turbines in shallow water with emphasis on ultimate limit state design. Ocean Engineering, 219, 108377.

[46]. Finn, L. D. (1976, May). A new deepwater offshore platform-the guyed tower. In Offshore Technology Conference. OnePetro.

[47]. Mavrakos, S. A., Papazoglou, V. J., Triantafyllou, M. S., & Hatjigeorgiou, J. (1996). Deep water mooring dynamics. Marine structures, 9(2), 181-209.

[48]. Fitzgerald, J., & Bergdahl, L. (2008). Including moorings in the assessment of a generic offshore wave energy converter: A frequency domain approach. Marine Structures, 21(1), 23-46.

[49]. Yuan, Z. M., Incecik, A., & Ji, C. (2014). Numerical study on a hybrid mooring system with clump weights and buoys. Ocean engineering, 88, 1-11.

[50]. Vicente, P. C., Falcão, A. F., & Justino, P. J. (2011, April). Slack-chain mooring configuration analysis of a floating wave energy converter. In Proceedings of the 26th International Workshop on Water Waves and Floating Bodies, Athens, Greece (Vol. 17).

[51]. Jonkman, B.J.; Kilcher, L. TurbSim User's Guide: Version 1.06.00; National Renewable Energy Laboratory: Golden, CO, USA, 2012.

[52]. IEC. International standard 61400-1, Wind turbines, Part 1: Design requirements, 2005.

[53]. Hasselmann, K., Barnett, T. P., Bouws, E., Carlson, H., Cartwright, D. E., Enke, K., ... & Walden, H. (1973). Measurements of wind-wave growth and swell decay during the Joint North Sea Wave Project (JONSWAP). *Ergaenzungsheft zur Deutschen Hydrographischen Zeitschrift, Reihe A*.

[54]. Faltinsen, O. (1993). Sea Loads on Ships and Offshore Structures (Cambridge Ocean Technology Series, Series Number 1) (Reprint ed.). Cambridge University Press.

[55]. Charlotte Obhrai. OFF580: Marine Technology-Lecture notes. Dept. of marine technology, UiS,2021

[56]. Daniel Kaasa, Integrated dynamic analysis of a semi-submersible wind turbine considering hull flexibility, Master thesis, NTNU, 2019

[57]. Gudmestad, O., 2015. *Marine technology and operations: Theory & practice*. WIT Press.

[58]. Cheng, Z., Wang, K., Gao, Z., & Moan, T. (2015). Dynamic response analysis of three floating wind turbine concepts with a two-bladed Darrieus rotor.

[59]. Wan, L., Gao, Z., & Moan, T. (2014, June). Model test of the STC concept in survival modes. In International Conference on Offshore Mechanics and Arctic Engineering (Vol. 45530, p. V09AT09A010). American Society of Mechanical Engineers.

[60]. Dick, W. D. (2011, March 22). *WAVE* ENERGY CONVERTER (US 7,909,536 B2). U.S Patent and Trademark Office. https://patentimages. storage.googleapis.com/f0/e7/2d/36b6a9f3ec359c/US7909536.pdf

[61]. Jaya Muliawan, M.; Gao, Z.; Moan, T.; Babarit, A., Analysis of a Two-Body Floating Wave Energy Converter with Particular Focus on the Effects of Power Take-Off and Mooring Systems on Energy Capture. Journal of Offshore Mechanics and Arctic Engineering 2013, 135 (3), 031902-031902-12.

[64]. Li, L., Cheng, Z., Yuan, Z., & Gao, Y. (2018). Short-term extreme response and fatigue damage of an integrated offshore renewable energy system. Renewable Energy, 126, 617-629.

[63]. Li, L., Gao, Y., Yuan, Z., Day, S., & Hu, Z. (2018). Dynamic response and power production of a floating integrated wind, wave, and tidal energy system. Renewable Energy, 116, 412-422.

[64]. Muliawan, M. J., Karimirad, M., & Moan, T. (2013). Dynamic response and power performance of a combined Spar-type floating wind turbine and coaxial floating wave energy converter. Renewable energy, 50, 47-57.

[65]. National Renewable Energy Laboratory. (2015, January). Reference Model 5 (RM5): Oscillating Surge Wave Energy Converter (NREL/TP-5000-62861). NREL. https://www.nrel.gov/docs/fy15osti/62861.pdf

[66]. Kurniawan, A., & Moan, T. (2012). Optimal geometries for wave absorbers oscillating about a fixed axis. IEEE Journal of Oceanic Engineering, 38(1), 117-130.

[67]. AS, D. N. V. G. (2015). *Position Mooring*. DNVGL-OS-E301.

[68]. Manual, A. (2010). The guide to anchoring. Vryhof Anchors.

[69]. Panterplast. (2022). Offshore and subsea Buoyancy systems and cable protection solutions [Brochure].6421-Offshore-and-Subsea_digital-brochure_-english_REV-2021_Spreads.pdf (partnerplast.com)

[70]. Clump Weights. (2022). SAGA SUBSEA. https://www.sagasubsea.com/clump-weights

[71]. SINTEF Ocean. RIFLEX 4.10.1 User Guide; SINTEF Ocean: Trondheim, Norway, 2017.

[72]. SINTEF Ocean. SIMO 4.10.1 User Guide; SINTEF Ocean: Trondheim, Norway, 2017.

[73]. DNV GL – Software. GeniE 7.33 User Guide; DNV GL – Software: Norway, 2016

[74]. DNV Software Report No.: 94-7100 / Revision 12, April 10, 2014

[75]. SINTEF Ocean. HydroD 4.7 User Guide; SINTEF Ocean: Trondheim, Norway, 2017.

[76]. Wen, T.R. (2018) Feasibility study and dynamic analysis of floating vertical axis wind turbines in multi-applications. [Master's thesis, University of Stavanger] Studentoppgaver (TN-IKM/TN-IMBM). http://hdl.hanlde.net/11250/256260

[77]. Cheng, Z., Wen, T. R., Ong, M. C., & Wang, K. (2019). Power performance and dynamic responses of a combined floating vertical axis wind turbine and wave energy converter concept. Energy, 171, 190-204

[78]. Jonkman BJ. TurbSim user's guide: version 1.50. Golden, CO, USA: NREL; 2009. Tech. Rep. NREL/TP-500-46198.

[79]. IEC. International Standard 61400-1, wind turbines, Part 1: design requirements. 2005.

[80]. Johannessen, K.; Meling, T.S.; Haver, S. Joint Distribution for Wind and Waves in the Northern North Sea. In Proceedings of the Eleventh International Offshore and Polar Engineering Conference, Stavanger, Norway, 17–22 June.

[81]. C.F Lee, C. Tryfonidis, M.C Ong (2022) Power Performance and Response Analysis of a Semi-Submersible Wind Turbine with Combined Flap Type and TORUS Wave Energy Converters. OMAE2022-79483

[82]. Michailides, C., Gao, Z., & Moan, T. (2016). Experimental study of the functionality of a semisubmersible wind turbine combined with flap-type Wave Energy Converters. Renewable Energy, 93, 675-690.

[83]. Cheng, Z., Wen, T. R., Ong, M. C., & Wang, K. (2019). Power performance and dynamic responses of a combined floating vertical axis wind turbine and wave energy converter concept. *Energy, 171, 190-204.*

[84]. Wan, L., Greco, M., Lugni, C., Gao, Z., & Moan, T. (2017). A combined wind and wave energy-converter concept in survival mode: Numerical and experimental study in

regular waves with a focus on water entry and exit. *Applied Ocean Research, 63*, 200-216

[85]. Michailides, C., Gao, Z., & Moan, T. (2016). Experimental and numerical study of the response of the offshore combined wind/wave energy concept SFC in extreme environmental conditions. *Marine Structures, 50*, 35-54.

[86]. Campanile, A., Piscopo, V., & Scamardella, A. (2018). Mooring design and selection for floating offshore wind turbines on intermediate and deep-water depths. *Ocean Engineering, 148, 349-360.*

[87]. Dnv, G. L. (2018). DNV GL-ST-0119 Floating wind turbine structures. DNV GL.